ETH

Eidgenössische Technische Hochschule Zürich
Swiss Federal Institute of Technology Zurich

Department of Physics

Quantum Device Lab

Zurich, Switzerland

Master Thesis

Towards continuous wave Rydberg excitation for $2\,^3\mathrm{S}_1$ Helium

Author: Dominik Friese

Date: 13th March, 2015

Tobias Thiele

Thesis Advisor

Prof. Dr. A. Wallraff

Principal Investigator

ABSTRACT

In this thesis, a setup for two-photon Rydberg excitation of metastable $2\,^3\mathrm{S}_1$ helium atoms is described. We first focus on the cw laser stabilization to an atomic resonance using a Pound-Drever-Hall scheme in combination with Doppler free saturation spectroscopy, describe a detection stage via pulsed field ionization and the extraction towards an MCP. Then we describe the actual Rydberg excitation.

For compatibility, most of the electronic and vacuum components built and used are standard hardware and can be reused in future projects.

As of now, the experience gained by problems we solved can be utilized to improve existing experiments or enhance the design of prospective experiments.

---

[1]Contact: dfriese@phys.ethz.ch

Table of Contents

List of Figures

CHAPTER 1

Introduction

1.1 Historical survey

> "Wenn mir Einstein ein Radiotelegramm schickt, er habe nun die Teilchennatur des Lichtes endgültig bewiesen, so kommt das Telegramm nur an, weil das Licht eine Welle ist."

> "If Einstein were to send me a telegram announcing irrefragable evidence of light-quanta the telegram could reach me only in virtue of the waves that were here."

> (Niels Bohr, Nobel prize speech, 1922 [1])

Quantum mechanics has undergone a long and difficult journey from its beginning to where it is today. Even the smartest minds of their generation had a hard time with the concepts and ideas that quantum mechanics introduced.

Yet, the influence of quantum mechanics is recognized only very flimsy in daily life but plays a major role when it comes to dealing with atoms and subatomic particles.

One crucial difference between classical and quantum mechanical systems is the phenomenon of superposition. A quantum mechanical system can be in a mixture of different states and takes its final state not until it was measured. The outcome is known only in a probabilistic sense.

In mathematical terms this can be expressed by writing a quantum mechanical state $|\Psi\rangle$ as

$$|\Psi\rangle = \alpha |0\rangle + \beta |1\rangle \tag{1.1}$$

with $|0\rangle$ and $|1\rangle$ being two possible states and $\alpha, \beta \in \mathbb{C}$. The modulus of the two coefficients $|\alpha|^2$ and $|\beta|^2$ can be interpreted as an expression for the probabilities to find the system in state $|0\rangle$ or $|1\rangle$ respectively and sum up to unity.

People struggled with the idea that there are physical processes that are not deterministic. There is a famous quotation from Einstein which expresses his discontent regarding this topic:

> "Die Quantenmechanik ist sehr achtunggebietend. Aber eine innere Stimme sagt mir, daß das noch nicht der wahre Jakob ist. Die Theorie liefert viel, aber dem Geheimnis des Alten bringt sie uns kaum näher. Jedenfalls bin ich überzeugt, daß *der* nicht würfelt."

> "Quantum mechanics is very impressive. But an inner voice tells me that it is not yet the 'true Jacob'. The theory says a lot, but does not bring us closer to the secret of the Old One. I am at all events convinced that *He* is not playing at dice."
>
> (Albert Einstein, Letter to Max Born, 1926 [2] [3])

As we can see, Einstein was not totally convinced of quantum mechanics even though he was one of the co-founder of quantum mechanics.

Nevertheless, the predictions that quantum mechanics makes are extremely accurate and have not been proven wrong so far.

An important concept is entanglement. The measurement outcome of two systems can be strongly correlated in a way that a measurement on one of those two determines instantaneously the state of the other one. Entanglement is a non-local property and can reach over tens of kilometers [4]. Entanglement was probably the corollary which experienced most resistance. Many scientists believed that there had to be hidden variables that explain all results of quantum theory while fulfilling the premiss of local realism. This assumption could be proven wrong by evincing that quantum mechanics contradicts Bell's inequality, where Bell's inequality is a must for a classical, local and realistic physical theory.

Nonetheless, information transfer faster than the speed of light is not possible, being compatible with causality and special relativity.

Today, entanglement is used for new applications like quantum cryptography, quantum computing and quantum teleportation [5–8].

1.2   Quantum computing

With quantum computing one speaks about the idea of performing quantum mechanical operations on quantum bits (qubits). For a practical quantum computer the following requirements must be fulfilled [9]:

1. A scalable physical system with well characterized qubits
2. The ability to initialize the state of the qubits to a simple fiducial state, such as $|000\ldots\rangle$
3. Ccoherence times much longer than the gate operation time
4. A "universal" set of quantum gates
5. A qubit-specific measurement capability

In principle, any two-level quantum system can be used as a qubit. Up to this date various systems have been investigated and proven to work. The first implementation of a quantum algorithm was done in a nuclear magnetic resonance system [10]. Notable other examples are Rydberg atoms [11], single-photon Bell-states [12], electron spin in semiconductor materials [13],

nuclear spins by nuclear spin resonance [14] [15], superconducting flux [16] [17], charge [18] [19] or phase qubits [20], and quantum dots [21].

All of the systems mentioned above have their advantages and disadvantages.

Two aspects must be considered when designing a quantum computing setup. The first challenge is to find a way to have both fast manipulation and long coherence time. On the one hand one wants to operate the qubits in a well defined and fast way, on the other hand the qubits shall be protected against decoherence at least as long as the computation and readout is going on.

The second problem is scalability. In general, a system is called scalable if its performance improves after adding new hardware proportional to the added hardware without reaching a limit. In case of quantum computers, the hardware are single and multi qubit gates and the qubits themselves. For a scalable quantum computer, an arbitrary number of qubits and gates must be addressable including error correction and read-out.

Scalability is probably the most difficult task in today's quantum computing research.

The number of gates and qubits depends on the algorithm used and the problem to be solved. For instance, the Shor-algorithm factorizing an integer, needs at least $\log(n)$ qubits to factorize the number n [22]. To illustrate the strength of the Shor-algorithm we may compare a common prime number based encryption method to state-of-the-art quantum computing systems.

RSA is a encryption method that is based on large prime numbers. It is recommended to use 2048 bit long key, i.e. a 600-digit number. To factorize this number we would need $\log\left(2^{2048}\right) \approx 1420$ entangled qubits. For comparison a 232-digit number (768 bit) was factorized by use of eighty computer processors in parallel within a time span of two years [23].

However, the world record for the most number of entangled qubits is 14 and the biggest number factorized with the Shor-algorithm is 21 with 10 entangled qubits used and 56'153 with a minimization algorithm and four qubits [24–26].

Hence, we are several milestones away from a quantum computer that can break contemporary prime number based encryption schemes or an universal computer that can be used for different algorithms.

Nevertheless, or maybe especially for that reason, the research for scalable and reliable quantum computers is going on actively.

1.3   Hybrid Quantum Systems

Hybrid atom-solid state quantum systems are promising candidates for quantum computers. The idea is to combine e.g. single atoms with solid state qubits to generate a system that allows for long coherence times with a maximum of control.

Single atoms can be thoroughly decoupled from the environment with theoretical coherence times exceeding several seconds. The downside, however, is that qubit manipulation can not be done fast in free space via RF or static external fields.

To enhance the single atoms approach one can combine it with circuit QED systems, for example, superconducting coplanar waveguide microwave resonators [27]. In contrast to the single atoms,

they can be strongly coupled to microwave photons and hence be modified fast. Though, the embedding into solid-state structures leads to lower coherence times.

Combining the best of both worlds, these newly formed Hybrid Quantum Systems are both robust and simultaneously fast to modify, forming a promising prospective for future quantum computing research.

1.4 The Rydberg experiment

In this experiment, a beam of metastable $2\,^1S_0$ helium atoms is excited to np Rydberg states with quantum number n between 30 and 50 via a single-photon excitation driven by a pulsed Nd:YAG pumped dye laser. Single Rydberg atoms are suitable to be coupled to microwave photons in a chip based transmission line because of their large dipole moment and their transition frequencies in the GHz regime. The dipole moment scales like n^2 which can result in values up to 10'000 Debye [28].

Additionally, by making use of their long radiative lifetime, they may serve as "quantum memory" in a quantum computer in the future. The lifetime scales like $n^3 - n^5$ depending on the l state and can have values ranging from microseconds to seconds [29].

The complete setup of the main Rydberg experiment can be seen in [30] as well as an excerpt of the setup in Fig. 1.1.
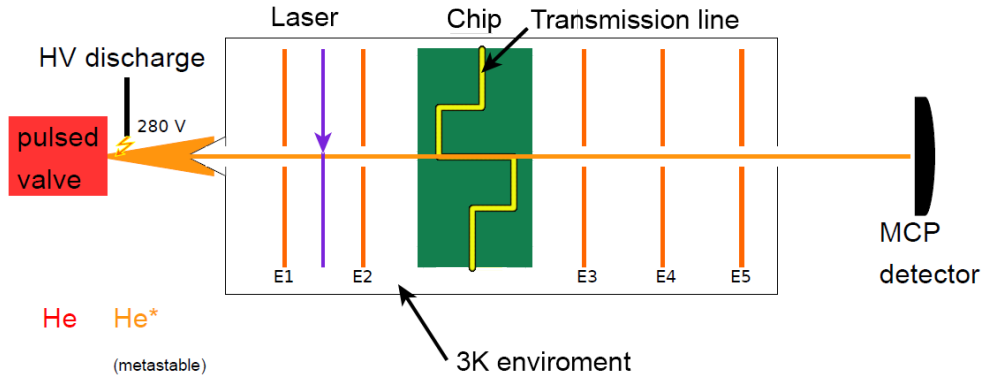
Fig. 1.1: Excerpt of the Rydberg experiment setup. Important for this thesis are the parts from the left up to E2.

The experiment consists of several stages. After being excited into a metastable state by a HV discharge the atoms are spatially filtered and brought into a Rydberg state by a UV laser with wavelength $\lambda = 312\,\text{nm}$.

Subsequently, the Rydberg atoms move across a chip held at a temperature of $3\,\text{K}$ containing a transmission line resonator at a distance of a few hundred micrometers. So far, coherent population transfer using microwave radiation is used to detect the electric fields above the chip [30].

As of now, the atoms used in the main experiment are in the $^1S_0$ singlet state. For higher lifetimes and less sensitivity to stray fields we want to switch to $^3S_1$ triplet states for which a new laser

system must be set up. For better beam control and higher repetition rates a new helium source is being designed and set up.

CHAPTER 2

Preliminary Deliberations

2.1 Level structure of Helium

The atomic levels of helium can be split into two parts: $^1S_0$ singlet and $^3S_1$ triplet states. In the singlet states, the excited electron has a spin antiparallel to the ground state electron, hence a total spin S=0. We call the helium 'parahelium'. In the triplet states, the excited and ground state electron have parallel spin and thus S=1. The helium is called 'orthohelium' in these states. From a quantum mechanical point of view the spin wave function must either be fully symmetric or fully antisymmetric under exchange of two particles. For the singlet state with antisymmetric electron spin wave function this requirement allows one possible spin wave function (thus the name singlet):

$$|\Psi_{\text{singlet}}\rangle = \frac{1}{\sqrt{2}} \left(|\uparrow\downarrow\rangle - |\downarrow\uparrow\rangle \right) \tag{2.1}$$

Likewise, the triplet state has three possible spin wave functions which are symmetric:

$$|\Psi_{\text{triplet},0}\rangle = \frac{1}{\sqrt{2}} \left(|\uparrow\downarrow\rangle + |\downarrow\uparrow\rangle \right) \tag{2.2}$$

$$|\Psi_{\text{triplet},+1}\rangle = |\uparrow\uparrow\rangle \tag{2.3}$$

$$|\Psi_{\text{triplet},-1}\rangle = |\downarrow\downarrow\rangle \tag{2.4}$$

The index in the triplet wave functions corresponds to the m_s value being the the projection of the total spin onto the quantizaton axis. It can take values from $-|S|$ to $+|S|$ in integer steps. A visualization of the Helium energy level structure can be found in Fig. 2.1. The important transitions for our experiments are denoted explicitly.
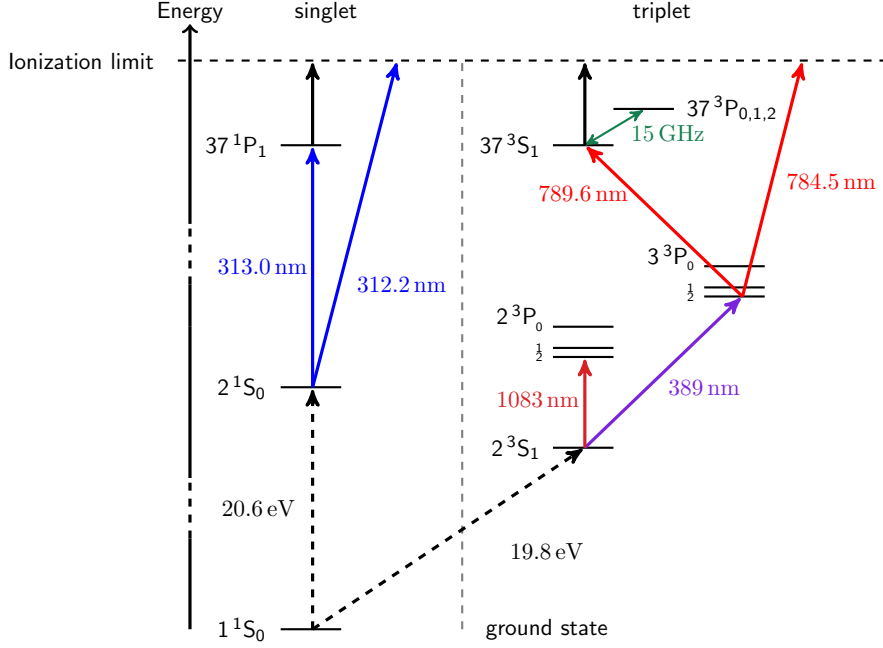
Fig. 2.1: Energy level scheme of Helium. The energy levels are noted by the Russell–Saunders term symbol $^{2S+1}L_J$ with $J = L + S$. Black dashed lines are covered by non-radiative processes, green solid lines by microwave radiation and coloured lines by optical frequencies. Black solid lines can be covered by both optical and non-optical processes.

The transition from the ground state $1\,^1S_0$ to the first excited states $2\,^1S_0$ and $2\,^3S_1$ are usually covered by discharge processes where the atoms are placed in a strong or oscillating electromagnetic field to become ionized. Afterwards, a fraction of about 10^{-8} recombines into the desired state.

Both $2\,^1S_0$ and $2\,^3S_1$ have long lifetimes of $19.7\,\mathrm{ms}$ respectively $7870\,\mathrm{s}$ [31] [32]. The long lifetime results from selection rules which are described in detail in the next Section 2.2. An optical transition must conserve momentum and both $2\,^1S_0$ and $2\,^3S_1$ have angular momentum $l = 0$ just as the ground state $1\,^1S_0$. Therefore, a transition is only possible through emission of two far-detuned photons which is unlikely to happen. In addition, for $2\,^3S_1$ the spin must be flipped extending the lifetime even more.

Transitions between levels above $n = 2$ are usually driven by laser radiation. The production of singlet Rydberg states is directly possible from the metastable $2\,^1S_0$ state. However, for the triplet Rydberg states a two-photon excitation via the intermediate $3\,^3P_{0,1,2}$ states is necessary to avoid ionization of the singlet state. The cycling transition $2\,^3S_1 \longleftrightarrow 2\,^3P_{0,1,2}$ at $1083\,\mathrm{nm}$ can be used to e.g. cool metastable helium atoms with an optical molasses.

Typical lifetimes of the relevant intermediate states $2\,^3P_{0,1,2}$ and $3\,^3P_{0,1,2}$ are $98\,\mathrm{ns}$ and $105\,\mathrm{ns}$ respectively [33]. The corresponding linewidths are $64.1\,\mathrm{MHz}$ respectively $59.8\,\mathrm{MHz}$.

2.2 Selection rules and allowed transitions

Not every transition is naturally allowed. An electric dipole transition accessible by lasers has to fulfill certain selection rules.

The most important selection rules for single electron Hydrogen-like atoms are given in Table 2.1.

Quantum number	Rule	Notes
Principal n	Δn arbitrary	dipole strength decreases with Δn^{-2}
Total angular momentum J	$\Delta J = 0, \pm 1$	except $0 \nrightarrow 0$
Orbital angular momentum l	$\Delta l = \pm 1$	$L < n$
Magnetic m_J	$\Delta m_J = 0, \pm 1$	$0 \nrightarrow 0$ if $\Delta J = 0$, $m_J = -|J| \ldots + |J|$
Spin s	$\Delta s = 0, \pm 1$	$\Delta s \neq 0$ if $\Delta J = 0$

Table 2.1: Electric dipole selection rules.

For our purpose, the orbital angular momentum and the magnetic quantum number are of interest. The orbital angular momentum rule has both advantages and disadvantages. On the one hand, for Rydberg excitation we are restricted to a state sequence with s $\rightarrow$ p $\rightarrow$ s for the angular momentum. On the other hand, it ensures that the metastable state exhibits a long lifetime because e.g. $2\,^3S_1 \rightarrow 1\,^1S_0$ is dipole forbidden and would violate the conservation of angular momentum.

The change in the magnetic quantum number plays a role when choosing the polarization of the incoming light. For a light vector $\vec{k}$ perpendicular to the atoms' quantization axis p-polarized light leads to $\Delta m = 0$ whereas s-polarized light induces a $\Delta m = \pm 1$ transition.

2.3 Characteristica of Rydberg atoms

2.3.1 Transition wavelengths

The transition wavelength between $3\,^3P_2$ and $n\,^3S_1$ can be calculated by assuming Hydrogen like energy levels with corrected principal quantum number n by an l-dependent term called 'Quantum defect' δ_l. The quantum defect is the additional phase that an electron picks up when it interacts with the ion-core potential of non-hydrogen atoms instead of the perfect $1/r$ Coulomb potential as depicted in Fig. 2.2. The effect is big for trajectories of the electron that traverse the core, i.e. states with low l. With $n^\star = n - \delta_l$ one can still use $E_{n^\star} = -\frac{Rhc}{n^{\star 2}} = -\frac{Rhc}{(n-\delta_l)^2}$ to obtain the energy levels. To first order, the transition wavelengths still scale like $1/n^2$. For instance, the calculated transition wavelengths for triplet Rydberg states starting from $3\,^3P_2$ can be seen in Fig. 2.3. The corresponding numbers can be found in Appendix A.
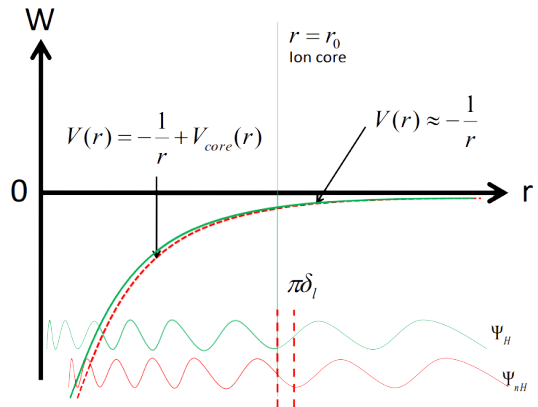
Fig. 2.2: Visualization of the quantum defect. Ψ_H is the hydrogenic wave function, Ψ_{nH} the non-hydrogenic one with modified core potential. The phase shift between Ψ_H and Ψ_{nH} is $\pi\delta_l$. For $r > r_0$ the core potential vanishes. [34]
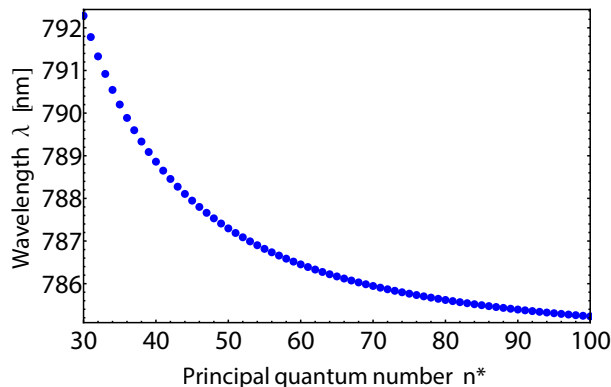
Fig. 2.3: Calculated Rydberg transition wavelengths for $3\,^3P_2 \rightarrow n^{\star\,3}S_1$.

2.3.2 Lifetime

The lifetime of both singlet and triplet states scaling as n^3 has been calculated by Theodosiou et. al. [35]. To motivate the shift from singlet to triplet states both lifetimes are given here. The np states given in Fig. 2.4 & 2.5 can be populated via microwave excitation from ns to np.
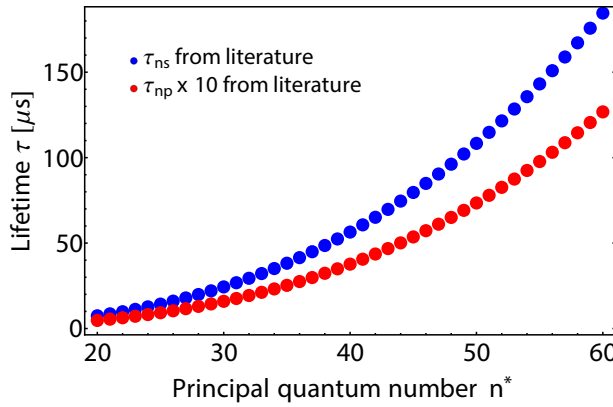
Fig. 2.4: Lifetime of the singlet states.   Fig. 2.5: Lifetime of the triplet states.

We see that the lifetime of the ns state is similar for both singlet and triplet states. However, the lifetime of the np state increases drastically. We achieve a factor 20 longer lifetimes for the $n\,{}^3\mathrm{P}_{0,1,2}$ states.

The improvement in lifetime can be explained if one considers the decay mechanisms. A decay will most likely happen between states with largest energy difference. For the singlet states $n\,{}^1\mathrm{P}_1$ can decay to the ground state $1\,{}^1\mathrm{S}_0$ easily. However, $n\,{}^1\mathrm{S}_0$ can not decay to the ground state without violating conservation of momentum. It must decay to $2\,{}^1\mathrm{P}_1$ where the energy difference is not as large and thus the lifetime higher.

For the triplet states a decay to the ground state is impossible for both $n\,{}^1\mathrm{S}_0$ and $n\,{}^1\mathrm{P}_{0,1,2}$ because of the different spin configuration. Therefore, $n\,{}^1\mathrm{P}_{0,1,2}$ decay to $2\,{}^1\mathrm{S}_0$ and $n\,{}^1\mathrm{S}_0$ to $2\,{}^1\mathrm{P}_{0,1,2}$. The lifetimes can be estimated by considering the overlap of the wavefunctions. For $n\,{}^1\mathrm{S}_0 \rightarrow 2\,{}^1\mathrm{P}_{0,1,2}$ the initial state has large, spherical symmetric wave function and the final state a dumbbell shaped wavefunction of small radius with zero modulus at the center. Vice versa for $n\,{}^1\mathrm{P}_{0,1,2} \rightarrow 2\,{}^1\mathrm{S}_0$. Therefore, the overlap of $n\,{}^1\mathrm{S}_0$ and $2\,{}^1\mathrm{P}_{0,1,2}$ is bigger than for $n\,{}^1\mathrm{P}_{0,1,2}$ and $2\,{}^1\mathrm{S}_0$ leading to a shorter lifetime of $n\,{}^1\mathrm{S}_0$. F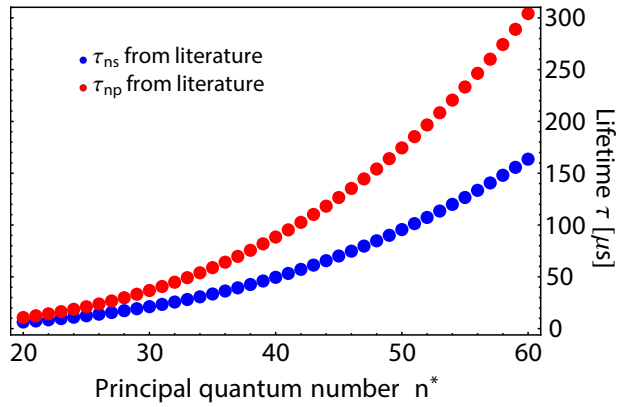or an exact explanation one must calculate the transition matrix elements and one utilizes Fermi's golden rule to calculate the Einstein coefficient.

2.3.3 Polarizability

Atoms located in an electric field experience a splitting of the energy levels because of the Stark effect. The strength of the quadratic Stark effect for small electric fields is characterized by the polarizability α.

The quadratic Stark effect results from second order perturbation theory and takes the form $\Delta E^{(2)} = \frac{1}{2}\alpha F^2$, F being the applied electric field. The polarizability α can be calculated via numerical simulations and scales with n^7 becoming relevant when working with Rydberg states. The polarizabiliy for the transition ns to np for specific $n^\star$ for both singlet and triplet states can be seen in Fig. 2.6 & 2.7.

Both curves are fitted with a $B \cdot n^7$ ansatz. The calculation yields $B_{\mathrm{singlet}} = (+50.535 \pm 0.34) \cdot 10^{-9}\,\mathrm{MHz\,cm^2/V^2}$ and $B_{\mathrm{triplet}} = (-3.7624 \pm 0.42) \cdot 10^{-9}\,\mathrm{MHz\,cm^2/V^2}$. Hence, we are one magnitude less sensitive to external DC electrical fields when switching to triplet states. Because

of p being energetically below the Stark manifold, α is negative and the transition frequency is lowered for higher fields as can be seen in the next section.
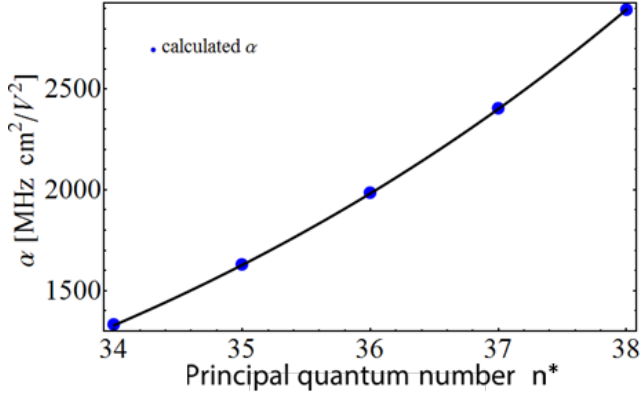
Fig. 2.6: Polarizability of the singlet states.
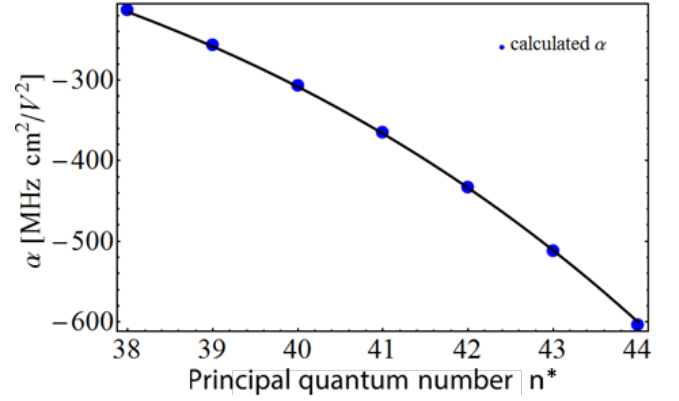
Fig. 2.7: Polarizability of the triplet states.

2.3.4 Stark manifolds

Upon applying an electric field to atoms the energy levels get shifted similar to what we have seen before. In addition to the quadratic Stark effect there is also a linear Stark effect that comes into play for higher effective field strengths F. States with energy levels close to each other begin to mix and new eigenstates must be introduced to describe the situation. The new eigenstates can be calculated via perturbation theory with a perturbing Hamiltonian $H^1 = eFz$ as a superposition of the primal eigenstates $|\Psi^0\rangle$. [36] The perturbative calculation yields

$$|\Psi^1_{nlm}\rangle = |\Psi^0_{nlm}\rangle + \sum_{(n'l'm')\neq(nlm)} \frac{\langle \Psi^0_{n'l'm'}|\, eFz\, |\Psi^0_{nlm}\rangle}{E_{nlm} - E_{n'l'm'}}. \qquad (2.5)$$

We see that the stronger the dipole coupling between two states the more they mix and one can not distinguish the free field eigenstates anymore.

A visualization of an exemplary Stark manifold can be calculated by exact diagonalization of single particle Hamiltonian and is shown in Fig. 2.8 & 2.9 [37].
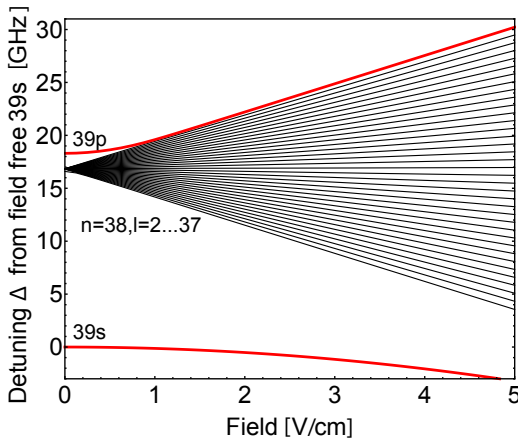
Fig. 2.8: Stark manifold of the $n = 38$ singlet state for $m_j = 0$.
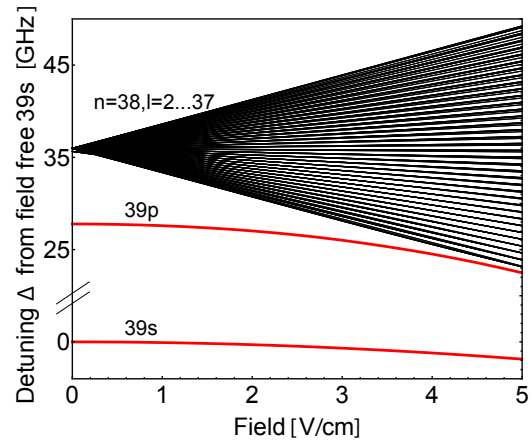
Fig. 2.9: Stark manifold of the $n = 38$ triplet state for $m_j = 0$.

The red line starting at $\Delta = 0\,\mathrm{GHz}$ represents the field free 39s state. Measured from this level one can see the 39p state separated from the $n = 38$ Stark manifold at about $17\,\mathrm{GHz}$ for the singlet respectively $27\,\mathrm{GHz}$ for the triplet. The 39s and 39p state are shifted down te become energetically located close to the Stark manifold of $n = 38$. All states with $n = 38$ and $l > 2$ are nearly degenerate for zero field and begin to mix already for small fields F. 38s and 38p are shifted down to the $n = 37$ manifold. The additional states in the manifold of Fig. 2.9 compared to Fig. 2.8 come from states with $J = L \pm 1$.

In case of the singlet states the Stark manifold is energetically located between the s and the p state. This leads to a larger splitting in transition frequency for increasing F. However, for the triplet states the Stark manifold is above both the s and p state. Therefore, a static field decreases the energy difference between the two states.

2.3.5   Ionization field

The ionization field of the singlet and triplet states show no discrepancy. However, there is a difference between s and p states. The p states need a slightly lower field for being ionized due to their already higher energy. We can estimate the ionizing electrical field with $F_{\mathrm{ionization}} = \frac{1}{16\,n^{\star 4}} F_A$ derived in [38]. $F_A = 5.142 \cdot 10^{11}\,\mathrm{V/m}$ is the atomic field strength. The ionization field strength and the difference between s and p states can be seen in Fig. 2.10.
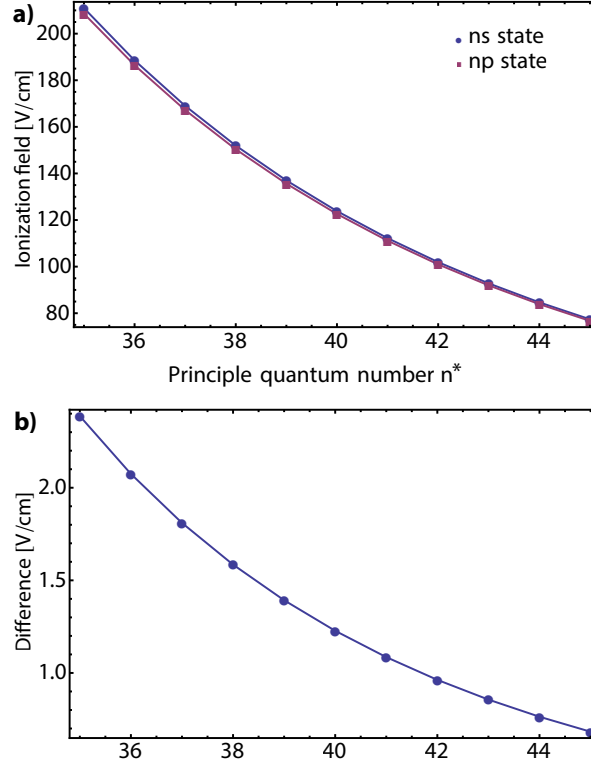
Fig. 2.10: **a)** The ionization field strength for $n^{\star} = 35 - 45$ for both s and p states. The field strength scales with $n^{\star\,-4}$. **b)** Difference in ionization field strength between s and p state. The difference scales with $n^{\star\,-5}$.

For increasing n the difference in ionization field strength declines rapidly and it becomes harder to separate the two states by their ionization field strength.

CHAPTER 3

Experimental Realization

3.1 Overview of the setup

The Rydberg atom source for the Hybrid Rydberg experiment is based on the existing helium source with some modifications. The helium source is described in [39–41] and will be outlined briefly in this thesis.

Fig. 3.1 gives an overview of the helium source in its current state.
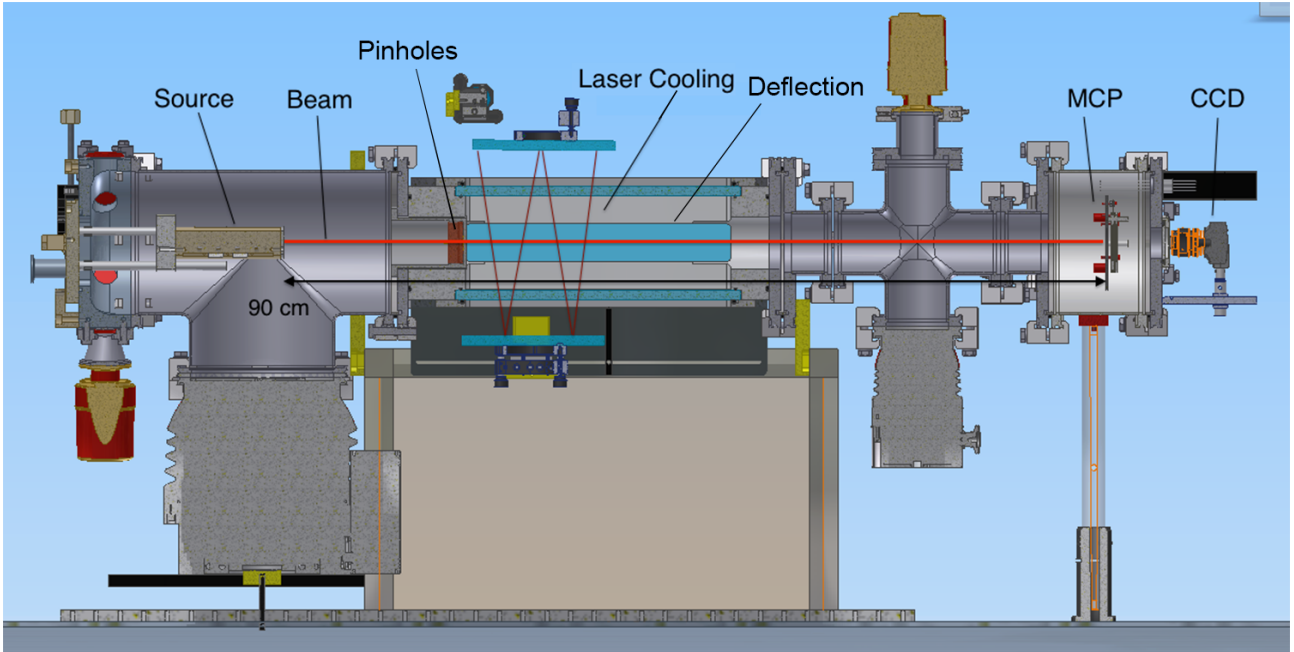
Fig. 3.1: Overview of the old helium Source. The parts are explained below. Image adapted from [39].

Helium atoms are injected into the vacuum chamber on the far left side. They are excited into the metastable $2\,^3S_1$ state by a discharge process in the "Source" area. A voltage of $200\,\mathrm{V}$ is applied to this zone while electrons are constantly inserted via a filament that is supplied by a current of $\sim 6\,\mathrm{A}$. This ionizes atoms and a fraction of $\simeq 10^{-5}$ of them recombine into the metastable $2\,^3S_1$ state. All particles – metastables, ground state atoms and ions – are transversally cooled with two pinholes. The pinholes act as a preliminary cooling step to enhance the beam shape.

Hereafter, the metastable $2\,^3S_1$ beam is optically cooled by a laser cooling process with a $1083\,\mathrm{nm}$ fiber laser and ends up as a collimated beam with transversal temperature close to the Doppler cooling limit [40].

Subsequently, the collimated beam of metastable atoms is separated from the rest by deflecting it in the horizontal direction. The mechanism is similar to the cooling, however, laser radiation shines from one side only [41]. Ideally, the metastable atoms are spatially separated from the rest and can be addressed solely in future setups.

So far, the atoms then hit an imaging microchannel plate assembly, usually called MCP, whose spatial signal can be detected either via a CCD camera or the trace of this signal on an oscilloscope. The plan to realize Rydberg excitation is readily described. After leaving the deflection region the atoms enter an area where they are excited into high n Rydberg states by a two-photon process. First, a pulsed near UV laser at $\lambda \simeq 389\,\mathrm{nm}$ brings them in one of the $3\,^3\mathrm{P}_{0,1,2}$ states followed by a tunable red laser with a tuning range of $\lambda \simeq 784 - 804\,\mathrm{nm}$. In principle, it can generate states from $20\,^3\mathrm{S}_1$ up to the ionization limit. After being excited to the desired state the atoms are ionized by voltage pulsed electrodes and the resulting ions or electrons are accelerated towards the MCP.

The pulsing of the UV laser and electrodes is necessary to separate the Rydberg excitation from the ionization. Furthermore, we want to restrict the ionization time window to a region where most of the passing atoms are in the metastable state.

The necessary modifications of the old version of the setup are humble. The main alterations have taken place at the vacuum cross in front the MCP. A magnified image section can be seen in Fig. 3.2.

The vacuum cross highlighted in orange is replaced by a double vacuum cross with additional 'arms' and openings in direction of the paper plane. On both of these openings AR coated 2" circular windows are installed. The position of the windows are highlighted in dark blue. The AR coating is designed such that the reflection is lowest for light in the range of 389 nm and $780 - 800\,\mathrm{nm}$, the wavelengths of

Fig. 3.2: Excerpt of the relevant parts. The modifications are explained in the text besides.

the lasers for the Rydberg excitation. The windows are described in Section 3.2.5.

Furthermore, four electrodes are inserted for ionization and extraction of the Rydberg atoms. Aligned along the direction of the lasers, i. e. from window to window, they are attached to the closure of the vacuum chamber (small circles in Fig. 3.2). A detailed description of the electrodes can be found in Section 3.4.1 along with a CAD model of the mounted electrodes in the double cross in Fig. 3.34.

Finally, the green part, formerly a pressure sensor, is replaced by an additional MCP. In contrast to the present MCP, the new one is solely time tracing and cannot provide images. However, the position perpendicular to the direction of flight of the atoms is an advantage because it cannot be hit by metastable atoms. This way, we can ensure to detect solely electrons that have been affected by the electrodes.

3.2 Optical setup

3.2.1 Laser setup and controls

TA SHG PRO

As mentioned before, the triplet Rydberg excitation is a two photon process. The first transition, $2\,^3S_1 \to 3\,^3P_{0,1,2}$, is carried out by a near UV laser of 389 nm. We use a Toptica TA SHG PRO. It consists of a DL PRO (788 nm diode laser) with an additional amplifier (TA PRO) and a second-harmonic generation (SHG) unit to create a frequency doubled beam. A sketch of the internal parts can be seen in Fig. 3.3.

The DL pro is equipped with a diode emitting light at a wavelength of $\lambda = 788$ nm.

After passing a 60 dB optical isolator to protect the diode from reflection the light enters a tapered amplifier and is amplified to a power of about 900 mW followed by a second optical isolator. Afterwards, the beam profile is shaped to match the mode of the resonant doubling cavity. The cavity contains one movable and three fixed mirrors as well as the doubling crystal. The movable mirror is mounted on a piezo-eletric element that regulates the cavity length to stabilize the frequency to a certain mode. The piezo is controlled by a PID feedback loop.

Fig. 3.3: Sketch of TA SHG PRO's internal layout. [42]

After leaving the cavity, the doubled light leaves the laser box through some additional beam shaping optics with a power of about 250 mW.

The center frequency of the laser diode can be shifted and swept which will be useful to find atomic resonances. This will be used for frequency stabilization of the TA SHG PRO to a specific atomic transition which is explained in Section 3.3.3.

Fig. 3.4: Overview of the TA SHG PRO laser setup.

Fig. 3.4 gives an overview of the UV laser setup. After exiting the casing the beam passes a $\lambda/2$ plate which is used to adjust the polarization. Subsequently, a polarizing beam splitter divides the beam into two parts. The ratio in power between the two paths can be tuned using the $\lambda/2$ plate. Our polarizing beam splitters are designed to reflect the s-polarized light and transmit the p-polarized light. The reflected light goes via two mirrors directly into a fiber coupler and is lead to a spectroscopy setup. The transmitted part passes an acousto-optic modulator (AOM) which is used to artificially pulse the laser. For an inactive AOM the light goes straight through, hits an iris and no light enters the fiber. Switching it on results in about 70% of the light being diffracted into the first order which is then coupled into a fiber.

Usually, one uses about 15 mW for the spectroscopy part and the rest for the actual excitation.

TA PRO

The transition to the Rydberg states, $3\,^3\mathrm{P}_{0,1,2} \to n\,^3\mathrm{S}_1$, is carried out by a TA PRO.

The laser is similar to the TA SHG PRO, however, it lacks the second harmonic generation unit. Fig. 3.3 is also valid for this laser with beam shaping optics and exit right after the second optical isolator. The power output of the laser is as high as possible to get a large population in the Rydberg states. We measure a maximum output power of about 2.90 W for a wavelength of 785 nm.

The light is coupled into a fiber with a Toptica FiberDock directly mounted to the case of the laser.

A probe beam can be lead off through a shutter before the tapered amplifier. This light is used to measure the wavelength via a fibercoupled HighFinesse WS/6-200 wavemeter. The wavelength information is used to determine the exact excitation wavelength.

Fig. 3.5: Overview of the TA PRO laser setup.

In order to be able to address as many Rydberg states as possible, the laser is tunable over the range of 780 nm to 805 nm. The wavelength adjustment is done via a combination of a motor and a piezo-electric element. The motor is capa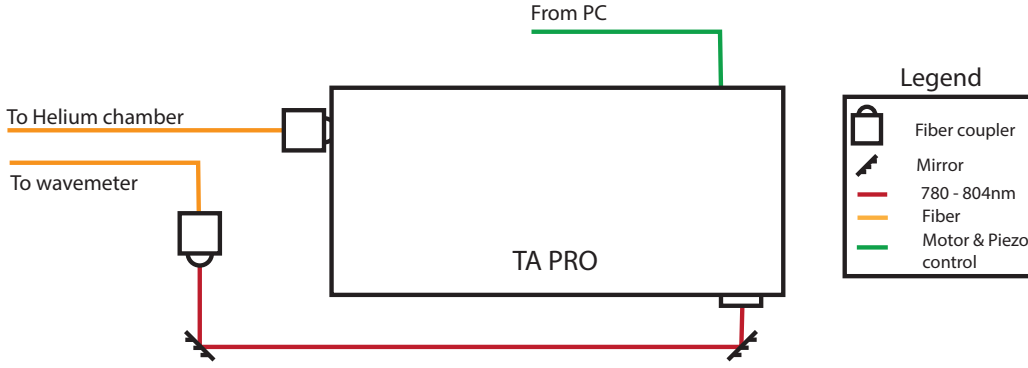ble of tuning the laser's wavelength coarsely to the vicinity of a transition. For fine adjustment the piezo-electric element is used. It can tune the wavelength up to about ± 0.5 nm around the motor's set spot.

Both the motor and the piezo are controlled via a LabView program. The control program with basic functions is supplied by Toptica and modified by Mathias. A screenshot and explanation of the program can be found in Appendix C.

It is capable of sweeping over multiple resonances as well as going above the ionization limit. Furthermore, it reads out the measurement oscilloscope and visualize the data. Most of the measurements are carried out remotely with this program while the experiment is running.

3.2.2 Overview of Fibers

Depending on the requirements we use different fibers in our experiment. In general, optical fibers are waveguides that consists of a core, cladding, buffer and a jacket. A sketch of a single-mode fiber with typical sizes can be seen in Fig. 3.6. Light entering the core is kept inside via total internal reflection. To maintain the total internal reflection a maximum incident angle must be deceeded. The maximum incident angle θ_{max} is often expressed in terms of the numerical aperture (NA) that depends on the refractive indices of the core and the cladding as $\text{NA} = \frac{1}{n_{\text{air}}} \sqrt{n_{\text{core}}^2 - n_{\text{cladding}}^2} = \sin \theta_{\text{max}}$. Typical values are NA$= 0.05 - 0.2$ and $\theta_{\text{max}} = 3 - 12°$. To enter the fiber with light the beam must be focused by a strong lens to a diameter on the order of the core diameter.
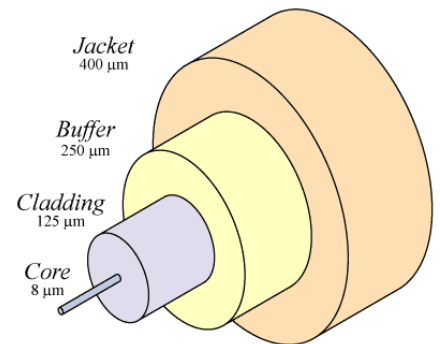

Fig. 3.6: Sketch of a fiber. Typical diameters are given in the sketch [43].

The buffer and jacket protect the cladding and core against damage. The relevant types of fibers are given subsequently.

Single mode (SM) fibers

Single mode fibers support only one spatial mode. For any input shape, the beam profile is split up into its different Laguerre- or Hermite-Gaussian modes (similar to a Fourier transformation; the actual decomposition depends on the geometry of the fiber) and the shape is projected onto one mode. A single mode fiber can be used to purify a beam profile at the expense of coupling efficiency.

Polarization maintaining (PM) fibers

Regular, non-polarization maintaining fibers – even if they are perfectly circular symmetric – experience birefringence because of bending and pulling or temperature gradients that break the symmetry. As a result, birefringence leads to uncontrolled polarization changes. Polarization maintaining fibers, however, have strong a built-in birefringence. For the incoming beam's polarization aligned along one of the birefringent axes, the polarization is maintained regardless of length, temperature and curvature of the fiber. Disturbances in polarization can propagate slowly if the two polarization axes are strongly decoupled from each other i. e. that the propagation constants distinguish strongly due to the birefringence.

High power (HP) fibers

High power, "longlife" fibers are designed to withstand high powers for a long period of time. In contrast to regular fibers, they can tolerate several Watts of incident power exceeding 1000 h. Typically, they are composed of pure fused silica to increase the damage threshold and to minimize Brillouin scattering. Brillouin scattering is an nonlinear effect that mainly happens in backwards direction and decreases the transmission efficiency of the fiber. Above a certain threshold, optical power can stimulate acoustic phonons at which light scatters. Fused silica however has a low nonlinearity and does not experience Brillouin scattering for powers below several Watts.

3.2.3 Fibers in experimental use

The best way to couple light into a fiber is by use of two mirrors and an adjustable lens. Two mirrors provide all necessary degrees of freedom – position and angle for both horizontal and vertical direction – whereas the lens can be adjusted to match the NA and core diameter of the fiber.

Practically, one uses an additional weak fiber laser that is plugged into the fiber coupler from the back before the actual fiber is connected. With two beams travelling in opposite direction, the weak coupling beam and the actual beam to be coupled in, one can overlap their spots at two separate points along the beam path to find an initial mirror configuration from which the coupling efficiency can be improved. Hereafter, the weak coupling beam can be detached and the

actual fiber be connected with and its output being measured on a photodiode.

To maximize coupling efficiency we use the technique of 'beam walking'. 'Walking the beam' is a process to adjust two mirrors in such a way that a specific angle and position in space is reached. In a first step we concentrate on one of the spatial directions and rotate the mirror closer to the coupler slightly. Second, the mirror further away is turned and a new output maximum on the photodiode is looked for. If the new maximum is higher than before turning the first mirror we continue to rotate the first mirror in the same direction until we reach a preliminary maximum. Subsequent, we switch to the other spatial direction and repeat the steps mentioned. The two directions alternate until we reach a global maximum. For further improvement the focus of the lens is tuned to reach a higher maximum and the beam walking is repeated again until the required efficiency is obtained.

The fibers used for the TA SHG PRO seen in Fig. 3.4 are both single mode and polarization maintaining. In addition, the fiber going into the helium chamber for Rydberg excitation is a high power fiber that has a specified degradation $<5\%$ over $1000\,\mathrm{h}$ at $120\,\mathrm{mW}$ input power. We choose a high power fiber to minimize Brillouin scattering as mentioned before. For both fibers we obtain a coupling efficiency of $55-60\%$.

The TA PRO as seen in Fig. 3.5 uses a SM/PM/HP fiber for the Rydberg excitation. The fiber is designed to withstand powers of more than $1\,\mathrm{W}$. The fiber connected to the wavemeter is a simple multi mode fiber. It has a core diameter of about $62\,\mu\mathrm{m}$ and a NA of 0.275 to support various modes. We use it with low powers of about $0.5\,\mathrm{mW}$ to avoid damage to the wavemeter. The achieved coupling efficiency for the HP fiber is of 70% and about 55% for the multi mode fiber.

3.2.4 Acousto-optic modulator

As mentioned in Section 3.2.1 we use an acousto-optic modulator to pulse the beam for the $2\,^3\mathrm{S}_1 \rightarrow 3\,^3\mathrm{P}_{0,1,2}$ transition.

An AOM works by injecting acoustic waves into an acousto active material. The traveling acoustic waves locally change the refractive index of the crystal and give rise to diffraction at the crystal planes. For a specific incident angle – the Bragg angle θ_{Bragg} – the diffraction works best and one gets a first order diffracted beam. The diffracted beam's frequency is shifted with respect to the original frequency either up or down depending on the relative orientation of the light's and the acoustic waves' k-vectors. The magnitude of the shift is equal to the frequency of the sound waves which follows from conservation of both energy and momentum. A sketch of an AOM can be found in Fig. 3.7.
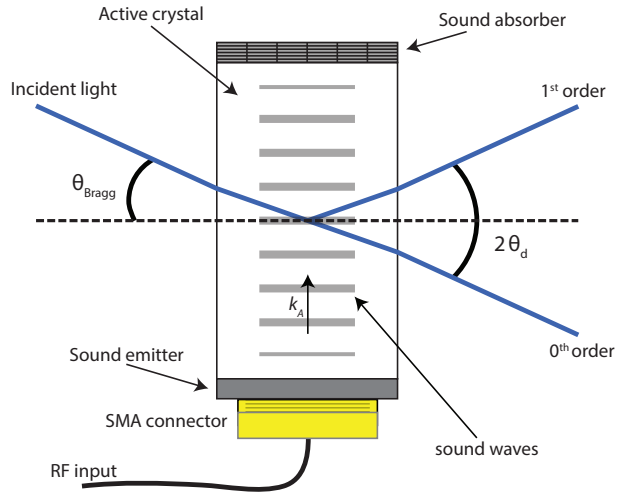
Fig. 3.7: Sketch of an AOM. The first order diffracted beam would have a decreased frequency.

For our AOMs we have an acoustic frequency of $f_A = 400\,\mathrm{MHz}$ and angles $\theta_{\mathrm{Bragg}} = 19\,\mathrm{mrad}$ and $2\,\theta_{\mathrm{d}} = 20\,\mathrm{mrad}$. The AOMs are either made of Fused Silica or Tellurium Dioxide for UV applications.

To accurately adjust the point in time where the UV laser shines on the atoms the rise time of the AOM and the delay between trigger and actual laser light entering the setup must be known. For this purpose a fast photodiode is placed in the diffracted beam after the AOM.

Determination of delay and rise time

The RF driver is switched on by a $3\,\mathrm{V}$ trigger signal with a pulse length much longer than the relevant time scales (about $20\,\mu\mathrm{s}$) and a rise time of $2\,\mathrm{ns}$ to reach $2\,\mathrm{V}$. The RF driver is already activated at $2\,\mathrm{V}$ but to ensure proper switching we use a higher trigger end level.

Fig. 3.8: Measurement of AOM delay time.

The delay between trigger and signal is about 800 ns (Fig. 3.8). This needs to be considered when designing the trigger sequence.

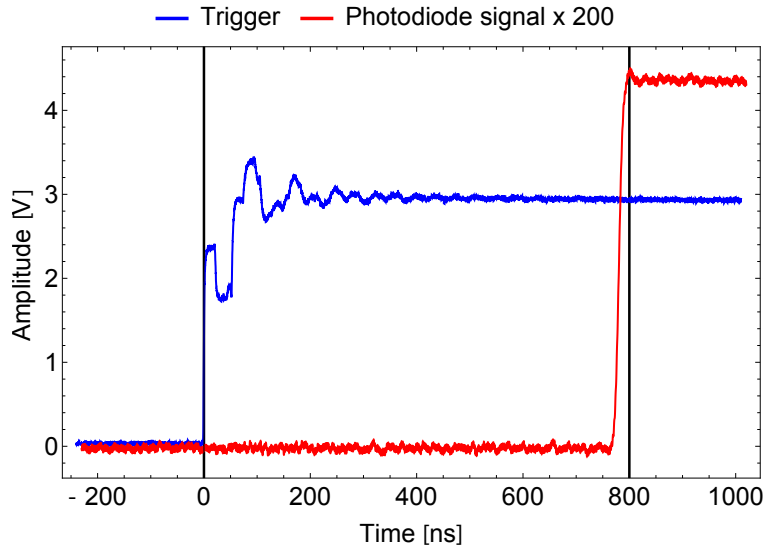We think that the delay is because of the AOM's driver which must ramp up its voltage to start driving the AOM crystal. Beyond a certain voltage the AOM suddenly begins to start modulating the light.

The rise time between 10 % and 90 % signal is about 15 ns as seen in Fig 3.9. The specified rise time is 5.5 ns. However, the photodiode has a specified bandwidth of 50 MHz which results under ideal circumstances in a minimum detection time of about 7 ns (for exact impedance matching and no parasitic capacitances).
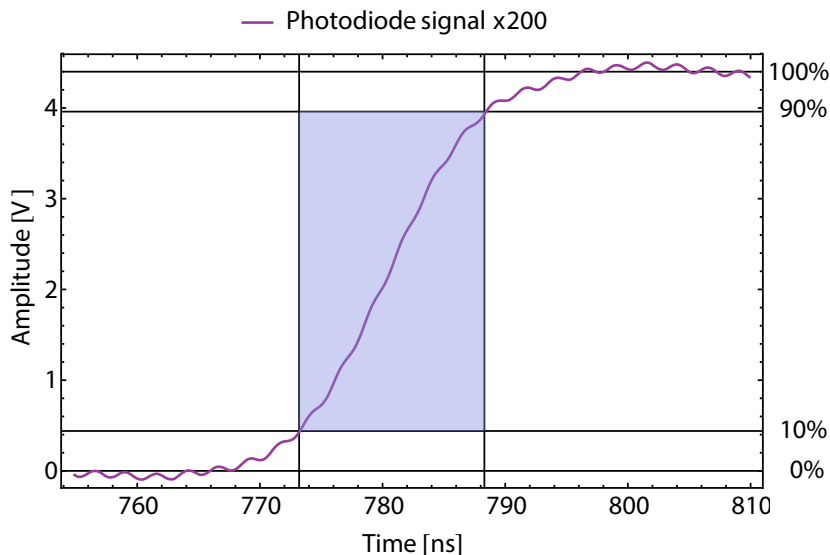
Fig. 3.9: Magnification of the rising edge from Fig. 3.8. Within the blue shaded area the signal rises from 10 % to 90 %. The left and right time markers are located at 773.2 ns and 788.3 ns.

However, we experience that the AOM's diffraction efficiency continually decreases from 70 % down to 20 % without changing the path that the laser takes through the crystal. A possible reason may be local heating up of the crystal (because of a bad crystal or insufficient coating).

22

The heated crystal has a slightly different refractive index which alters the properties of the AOM. Upon bad diffraction efficiency, the beam path can be slightly altered to regain the maximum efficiency of 70 %. In the current experiment the AOM has been exchanged by the manufacturer. The new AOM made of Tellurium Dioxide has a lower diffraction efficiency of 50 % yet being stable in the UV range.

The compensation AOM before the spectroscopy cell is used in a constant mode with a diffraction efficiency of $40 - 50$ %. It experiences no short-term changes in efficiency and it is enough to check it once a week.

3.2.5   AR coated windows

The pulsed 389 nm and the constant 790 nm laser for Rydberg excitation cross the chamber via two 2" anti-reflection (AR) windows which are mounted on the double cross as indicated in Fig. 3.10. The windows are held in place by the vacuum within the chamber.
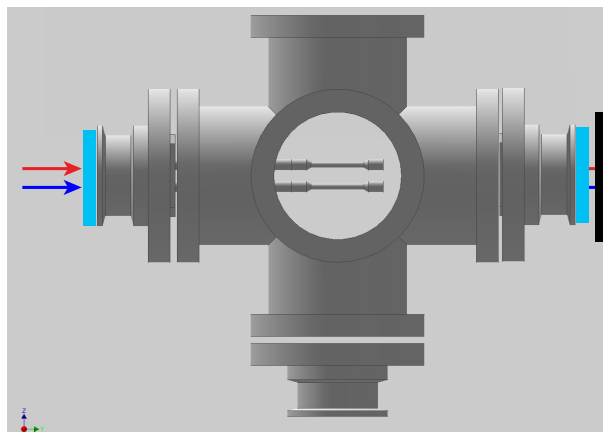
Fig. 3.10: Double cross with AR windows mounted. The laser beams, indicated by the red and blue arrow, move colinear through the setup and are blocked at the end. For better alignment the block can be removed temporarily.

It is crucial that the windows reflect as little light as possible to minimize power losses. Therefore, custom made windows are ordered whose reflection spectrum can be found in Fig. 3.11.
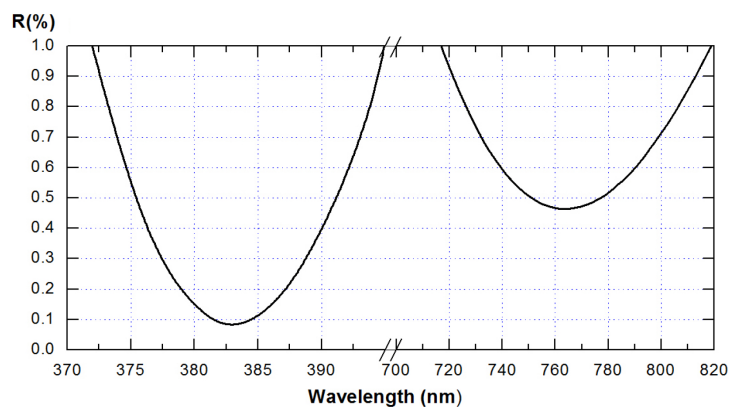
Fig. 3.11: Reflection spectrum of the AR coated windows [44].

Even with the AR coating and perfect 0° incident angle, the windows reflect $5-7\,\mathrm{mW}$ of the incident light at $790\,\mathrm{nm}$. Hence, precise alignment of the beams with respect to the window surface is important to minimize stray light and maximize power. The laser beams are blocked after the second window. For alignment the beam block can be removed and both laser can be overlapped at a far distance.

A photograph of one of the mounted windows can be seen in Appendix E.

3.2.6 Beam combination and alignment

For Rydberg excitation the two laser beams must be overlapped precisely. This is achieved by a dichroic mirror and two fully movable and rotatable output coupling stages. These stages include a lens system and a $\lambda/2$ plate to adjust the polarization. A photograph of the stage can be seen in Fig. 3.12.

The golden screws marked with red at the middle of the stage are used for translation along the two horizontal axes. The screws marked with blue at the bottom are used for rotation and tilting. The screw marked in light green adjusts the distance between the two lenses. The small golden screws at the top and the top side are used for fine adjustment of the lenses and the output coupler.

The first lens with focal length $f = 6.24\,\mathrm{mm}$ is used to compensate the large divergence angle of the beam leaving the fiber and collimates the beam. By varying the distance between the first and the second lense with $f = 40\,\mathrm{mm}$ one can translate the

Fig. 3.12: Photograph of the coupling stage. The effect of the colored screws is explained besides.

position of the focus of laser beam. Furthermore, the beam can be collimated if the focus is set to infinity. The size of the collimated beam can be adjusted by changing the distance between fiber and first lens, the shorter the distance the smaller the collimated beam.
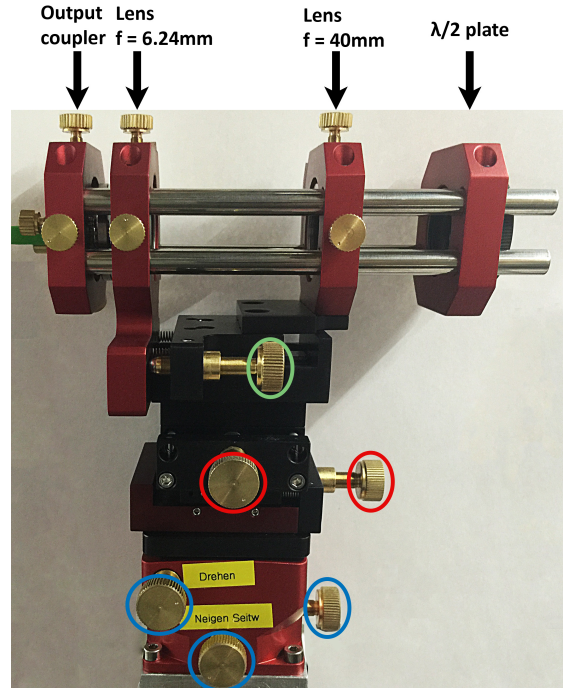
To combine the two beams with different wavelength we use a dichroic mirror. It is designed to be transparent for a specific wavelength range while being reflective for a different wavelength range at the same time. The red laser is transmitted through the backside of the mirror on axis with the experiment whereas the blue laser is brought in from a 90° angle and reflected at the frontside. After the mirror the two beams move collinear. The setup we use is sketched in Fig. 3.13.

The mirrors we use are custom made and have coatings on both sides. The green side has a reflectivity $>99.5\%$ for 400 nm and a transmissivity $>95\%$ for 800 nm. The red side has an AR coating with $< 0.5\%$ reflection for 800 nm. All values hold for an incident angle of 45° [45].

Fig. 3.13: Output coupling stages for excitation. Beams are combined with a dichroic mirror. The output coupling stages are one combined piece.

To overlap the two beam exactly we sent the red laser through the vacuum cross with the beam block seen in Fig. 3.10 removed by adjusting the screws of the coupling stage at first. Aferwards, the blue laser is also sent through by turning the screws of the dichroic mirror mount. In principle, turning the mirror does not change the path of the red laser. To maximize the overlap we 'walk' the blue laser and compare the two beams at two distant spots. The first position is right at the entrance window, the second one at a distant wall after the vacuum cross. For perfect overlap and collinear paths within the vacuum chamber, the beams must be overlapped at those two points.

3.2.7 Measurement of the beam profile

To ensure that the coupling stages collimate and focus the beams we measure one of the beam profiles. It is possible to measure the beam profile of the UV laser before entering the fiber to the helium chamber seen in Fig. 3.4 and after leaving the output coupling stage seen in Fig. 3.13 at different distances. The measurement data for the beam after passing the AOM but before entering the fiber can be seen in Fig. 3.14 and 3.15. Measurement data after the output coupling stage can be found in Fig. 3.16 and 3.17.

Before the fiber, a two dimensional beam profile is measured and two slices of it are taken along the horizontal and vertical directions. They are indicated with the white lines seen in Fig. 3.14. The FWHM for both directions is calculated with a Gaussian fit and is given by $w_{\mathrm{HM}} = 2\sqrt{2\log 2}\,\sigma$, σ being the standard deviation extracted from the fits. We find $w_{\mathrm{HM,\ horizontal}} = 887.3 \pm 0.65\,\mu\mathrm{m}$ and $w_{\mathrm{HM,\ vertical}} = 1237.0 \pm 1.45\,\mu\mathrm{m}$.
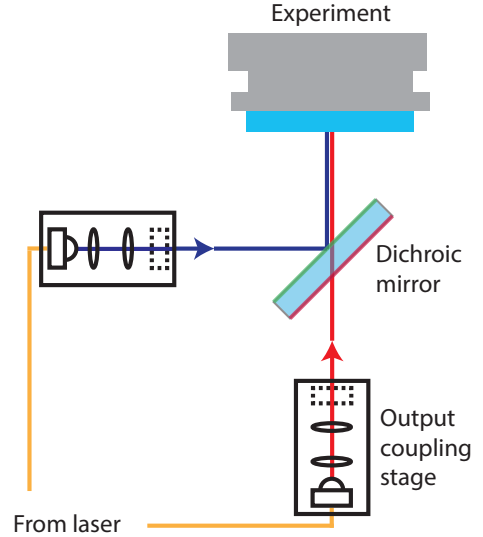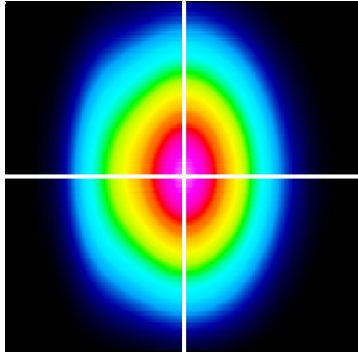
Fig. 3.14: Beam profiler measurement after the AOM and before entering the fiber. The image shows a 2D profile of the beam.
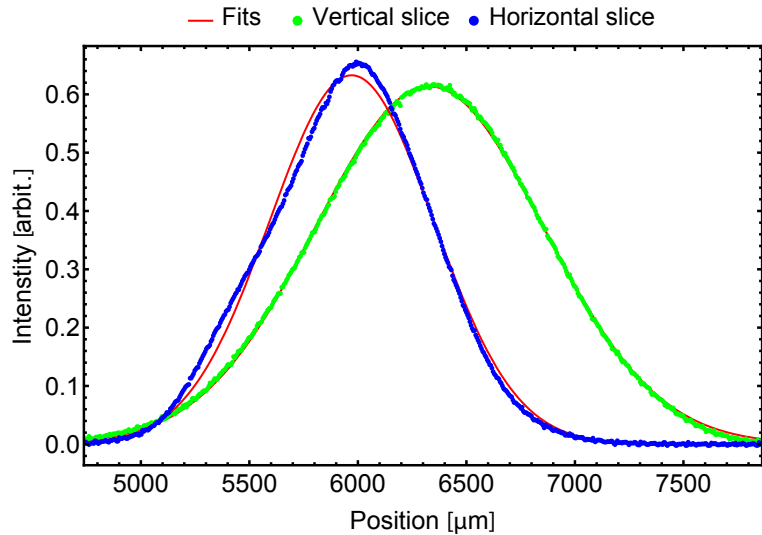
Fig. 3.15: Plots of the slices through the 2D beam profile in front of the fiber from Fig. 3.14. Each data set (green and blue) is fitted with a Gaussian (red).

The beam shape is slightly elliptic which is expected for diode lasers. Beam shaping optics before the exit of the laser case are used to compensate the ellipticity and make the beam more circular. Yet, this is not achievable completely as seen in the different FWHMs of the two transversal directions. In principle, the beam shape should be cleansed when coupling the light into the fiber as explained in Section 3.2.2.

After the fiber and output coupling stage the beam is mode matched with the fiber and either collimated or focused down.

A collimated beam profile can be seen in Fig. 3.16.

Fig. 3.16: Beam profiler measurement after exiting the fiber and the output coupling state. The image shows a 2D profile of the beam.
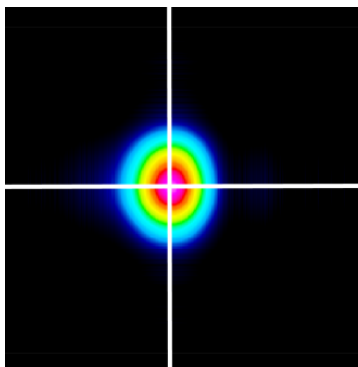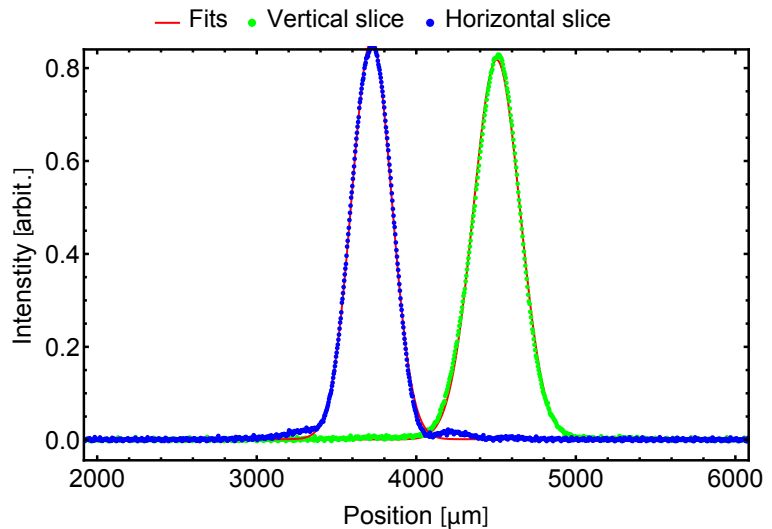

Fig. 3.17: Plots of the slices through the 2D beam profile after the output coupling stage from Fig. 3.16. Each data set (green and blue) is fitted with a Gaussian (red).

From the fit of the two curves we can extract the FWHM as before. For the given example we find $w_{\text{HM, horizontal}} = 295.2 \pm 0.37\,\mu\text{m}$ and $w_{\text{HM, vertical}} = 344.4 \pm 0.31\,\mu\text{m}$. We notice that the profile of the beam resembles a more circular shape than before which can be ascribed to the single mode fiber's fundamental Gaussian mode. The deviations can be imputed to e. g. the lenses of the output coupling state that are not passed perfectly concentrically.

Besides collimation, the lenses can be arranged to focus the beam. The FWHMs for slices along the horizontal direction at varying distance to the focus is shown in Fig. 3.18.
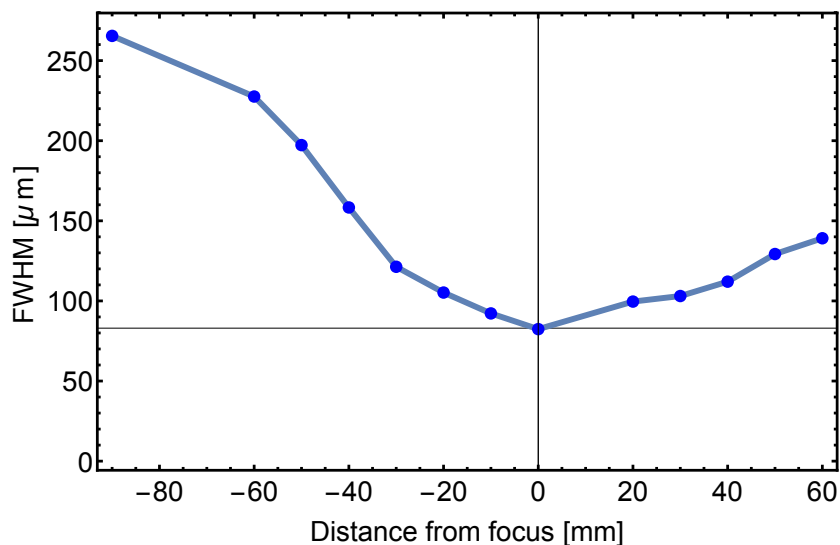
Fig. 3.18: FWHMs for varying distance to the focus.

We achieve a minimum FWHM of $83\,\mu\text{m}$ at the focus. For the behaviour of the FHWMs off focus we observe a slightly asymmetric shape. In principle, one would expect a shape similar to Fig. 3.19. The origin can be inferred to aberrations of the lenses.
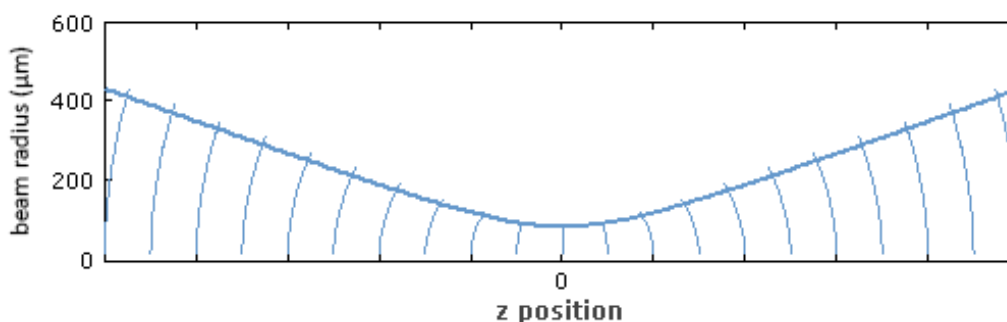
Fig. 3.19: Expected behaviour of the FWHMs

27

3.2.8 Intensity

With the measurements at hand, the achievable intensities and populations for Rydberg excitation can be estimated.

The population of atoms in the excited state can be calculated in the limit of large intensity to be

$$N_2(I) = \frac{1}{2}\left(1 - \frac{1}{1 + \frac{I}{I_{\text{sat}}}}\right)$$

with saturation intensity I_{sat} for a two-level system given by

$$I_{sat} = \frac{h\nu}{\sigma(\nu)\cdot\tau_s}$$

where $\sigma(\nu) = A_{21}\frac{\lambda^2}{8\pi n^2}\, g(\nu)$ is the cross section and $g(\nu)$ the line shape of the transition.

For a power P of $30\,\text{mW}$ exiting the fiber, a collimated beam has an intensity I of about $1330\,\frac{\text{mW}}{\text{cm}^2} \approx 380\, I_{\text{sat}}$. For the focused beam we achieve $I \approx 17.4\,\frac{\text{W}}{\text{cm}^2} \approx 4930\, I_{\text{sat}}$.

With $N_2^{\text{coll.}} \approx N_2^{\text{foc.}}$ we conclude that a collimated beam is sufficient to saturate the transition.

3.3 Frequency stabilization

By default, the TA SGH PRO is coarsely set to a wavelength in the vicinity of $\lambda = 389\,\text{nm}$. With a laser linewidth of about $200\,\text{kHz}$ and a linewidth for each of the three $2\,{}^3\text{S}_1 \rightarrow 3\,{}^3\text{P}_{0,1,2}$ transitions of $w = \frac{1}{2\pi\tau} = \frac{A}{2\pi} = \frac{10\,\text{MHz}}{2\,\pi} \approx 1.6\,\text{MHz}$ we must adjust the laser frequency precisely to match one of the transition. The procedure of frequency stabilization is described in the following sections.

3.3.1 Pound-Drever-Hall locking

The Pound-Drever-Hall (PDH) locking method is a method for obtaining an error signal from a resonance. Eventually, the error signal is fed into a PID controller which controls the laser's frequency.

A proper and useful error signal is supposed to satisfy several properties. It should be antisymmetric around the resonance frequency and have a zero-crossing at the resonance frequency which is used as the set point to lock the laser. This can be achieved by modulating the laser before entering the spectroscopy cell and subsequent demodulation.

A generic setup can be seen in Fig. 3.20.
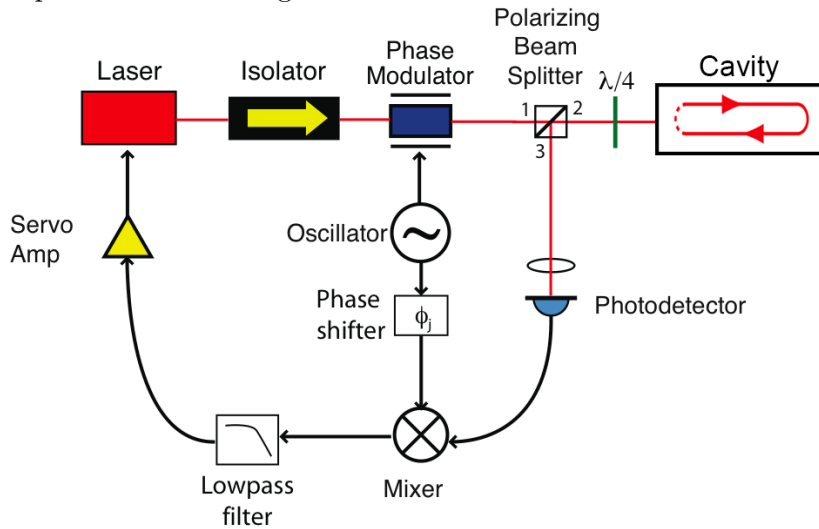
Fig. 3.20: A standard PDH scheme. Figure adapted from [46].

The light emitted by the laser at frequency f_0 passes an optical isolator and enters a phase modulator. After passing the phase modulator, the light's incident electric field $E = E_0\,e^{i2\pi f_0 t} = E_0\,e^{i\omega t}$ changes to $E = E_0\,e^{i(\omega t + \beta \sin(\omega_m t))}$ where $\omega_m = 2\pi f_m$ is the modulation rate and β the modulation depth of the phase modulator.

A first order Taylor expansion gives $E \approx E_0\,e^{i\omega t}\left[1 + J_1(\beta)e^{i\omega_m t} - J_1(\beta)e^{-i\omega_m t}\right]$ which can be seen as a superposition of three different frequencies: ω, $\omega + \omega_m$ and $\omega - \omega_m$. The center frequency ω is the carrier, the other two constitute the first pair of sidebands.

In spectroscopy, E is sent into a cavity or an atomic cell and picks up the characteristics in its amplitude and phase which is then detected on a photodetector. A calculated spectroscopy signal can be seen in Fig. 3.21 where the frequency of the light is being swept.
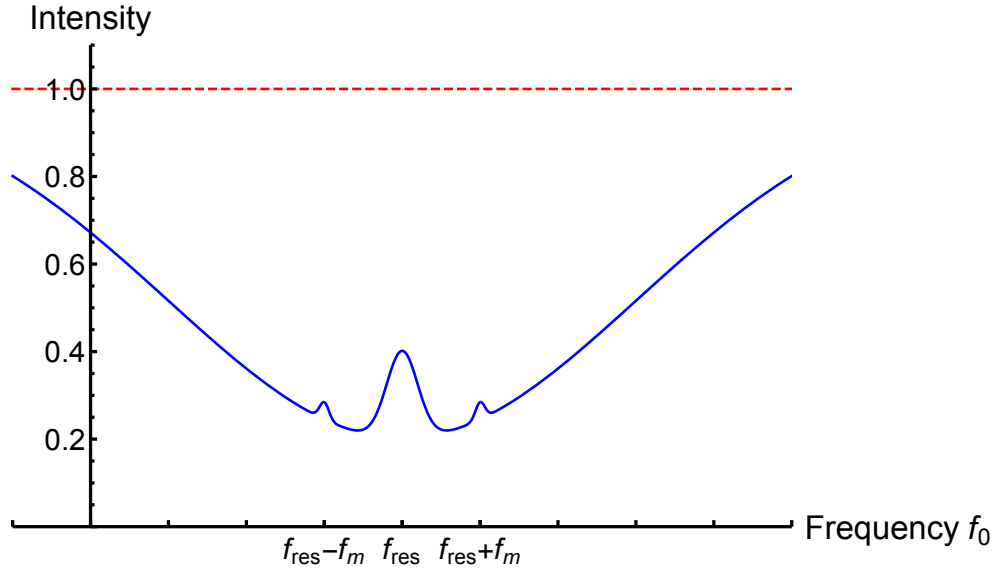
Fig. 3.21: Calculated spectroscopy signal. The red line shows the intensity of the light before the cavity, the blue line shows the intensity after passing the cavity.

The RF spectroscopy signal is then demodulated using a mixer with a phase shifted LO signal. With a correctly adjusted phase the sidebands interfere with the carrier and in combination with a lowpass filter produce an error signal as in Fig. 3.22. The zero-crossing of the error signal is exactly at the resonance frequency.

By choosing a set point at e.g. the zero-crossing of the error signal, a PID controller is in principle now capable of regulating the laser's frequency very accurately with respect to the transition frequency.
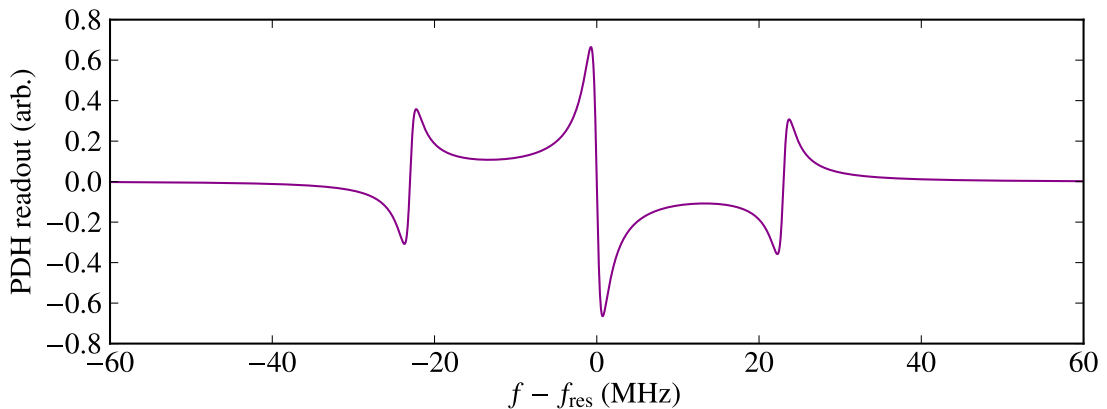
Fig. 3.22: Example of an error function from a Fabry-Perot cavity. The modulation frequency is $f_m = \omega_m/2\pi = 23\,\mathrm{MHz}$, the length of the cavity $L = 1.0\,\mathrm{m}$ and the finesse $\sim 6.3 \cdot 10^3$.

Often, the linewidth of the laser or of the cell is larger or similar to the modulation frequency. In this case the sidebands are hardly visible in the intensity profile detected on the photo detector.

However, the error signal is still of good qualitiy and can be used to obtain suitable control data because we pick out the specific modulation frequency via the mixer and ignore everything else, e. g. the background DC signal.

### 3.3.2 Dopplerfree saturation spectroscopy

One procedure to obtain the resonance signal of an atomic transition that the PDH technique needs is the Dopplerfree saturation spectroscopy (DFSS). The major advantage of DFSS is the lacking demand of cooling the atoms to a regime where Doppler broadening of the measured transition frequencies because of the temperature of the atoms is no longer relevant. The idea is similar to a classical pump probe method with two beams traveling in opposite directions. Ideally, the pump beam is several magnitudes more intense than the probe beam to ensure a strong contrast.

A spectroscopy cell filled with the atoms is placed in the pathway of both pump and probe beam and the intensity spectrum of the probe beam is measured. The beam path of both beams must be overlapped. Depending on the relative velocity with respect to one of the beams, different sets of atoms absorb the light, i. e. a red-detuned pump beam is absorbed by atoms moving towards it with a velocity corresponding to the detuning $\delta = \vec{k} \cdot \vec{v}$ and vice versa for a blue-detuned beam. The same holds for the probe beam yet for atoms moving in opposite direction.

Being resonant with one velocity class of atoms, the pump beam's transmission for the relevant frequency is reduced and the population of the atoms in the upper state is increased. The dips in the ground state population spectrum in Fig. 3.23 *b)* result from excitation of atoms with compatible velocity. Large dips are created by the pump beam, the smaller dips by the probe beam. Since the two beams counterpropagate, each one addresses atoms with the same velocity but different directions i. e. $v_{\mathrm{pump}} = -v_{\mathrm{probe}}$.
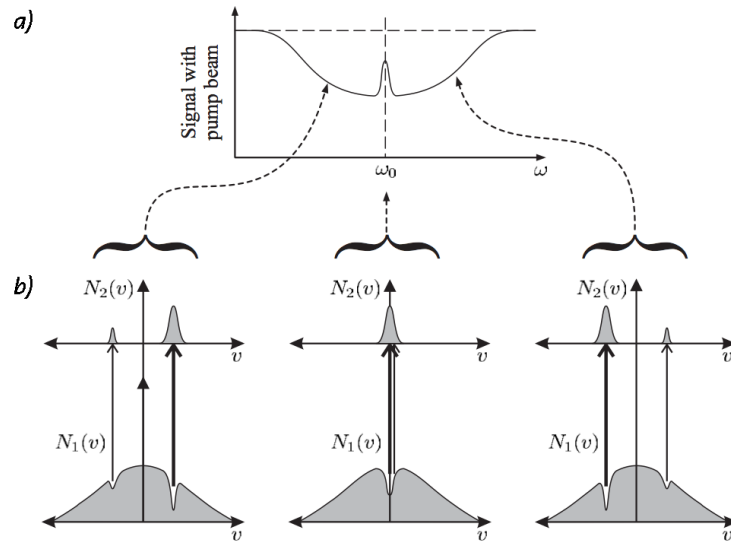
Fig. 3.23: Transmission line and population for the saturated absorption spectroscopy. a) The absorption spectrum of the pump beam with the visible decrease at resonance ω_0. b) The population of the ground state N_1 and the excited state N_2 for various detunings. Note that the ground state population can never reach zero because population inversion is not possible in a two-level system regardless of beam intensity. Image adapted from [47] p. 158.

For Dopplerfree frequency stabilization, one wants to obtain an absorption spectrum similar to Fig. 3.23 *a)* where a single peak is visible within a broad absorption dip. The absorption dips of pump and probe beam are overlapping and both beams address the same velocity class of atoms – the ones with $v = 0$. The pump beam excites most of the atoms to the upper level and the probe beam can pass unimpeded.

The width of the peak is determined by the natural linewidth of the transition and the linewidth of the laser.

Spectroscopy cell

For locking the TA SHG PRO we need a spectroscopy signal. The signal is obtained by use of a DFSS setup as explained in Section 3.3.3. The spectroscopy cell we use is described in the following.

The spectroscopy cell is filled with helium atoms in the metastable $2\,^3S_1$ state and can be seen while glowing in Fig. 3.24.
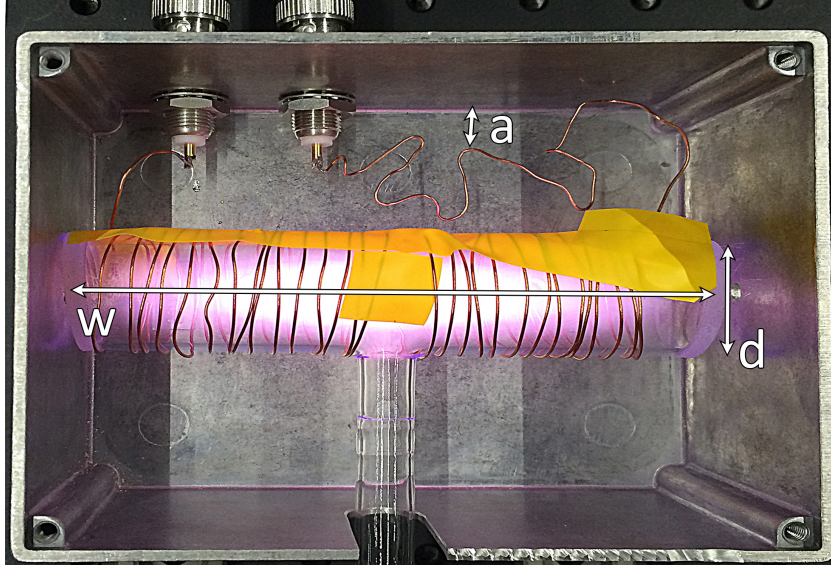

Fig. 3.24: The spectroscopy cell while glowing. The coiled wire creates a strong and rapidly varying field inside the cell. The cell has dimensions w = 8.5 cm, d = 2.5 cm and a ≈ 1 cm.

As for the color of the glowing, it strongly depends on the helium pressure within the cell and the consequent helium-nitrogen ratio. Ideally, the cell is glowing blueish whereas a reddish/pink tone is a sign for a too high nitrogen concentration [39]. The ideal pressure in terms of a strong error signal is about $1.1 - 1.3 \cdot 10^{-1}$ mbar with a background pressure of $\ll 10^{-2}$ mbar. An estimated fraction of about 10^{-8} of the total helium atoms in the cell are excited to the metastable state. The metastable state is created by a cold discharge induced by a rapidly oscillating magnetic field. In the cold RF induced discharge electrons and ion-cores are separated by the oscillating magnetic field creating an inductively coupled plasma. The magnetic field induces circular currents within the plasma that supply the plasma with energy and can be calculated with the third Maxwell equation $\vec{\nabla} \times \vec{E} = -\frac{\partial \vec{B}}{\partial t}$. To start the discharge process the resonance frequency of the plasma of about $25 - 30$ MHz and the frequency of the oscillating circuit must be equal, i. e. they must be impedance matched. We achieve this by changing the capacitance and inductance of the current carrying wire. Leading the wire close to the metal case in S-shaped curves increases the capacitance of the circuit and likewise decreases the resonance frequency $f = \frac{1}{2\pi\sqrt{LC}}$. The coil has a fixed number of $L = 29$ windings and is fixed with adhesive tape. With the geometry given in Fig. 3.24 the effective capacitance can be calculated. We find $C \approx 4 - 5$ pF and $L \approx 4.18\,\mu$H for $f = 27$ MHz.

3.3.3 Locking the TA SHG PRO

For accurately stabilizing the TA SHG PRO's frequency with respect to the desired transition we use a Pound-Drever-Hall locking scheme as explained in Section 3.3.1. The optical setup can be seen in Fig. 3.25.
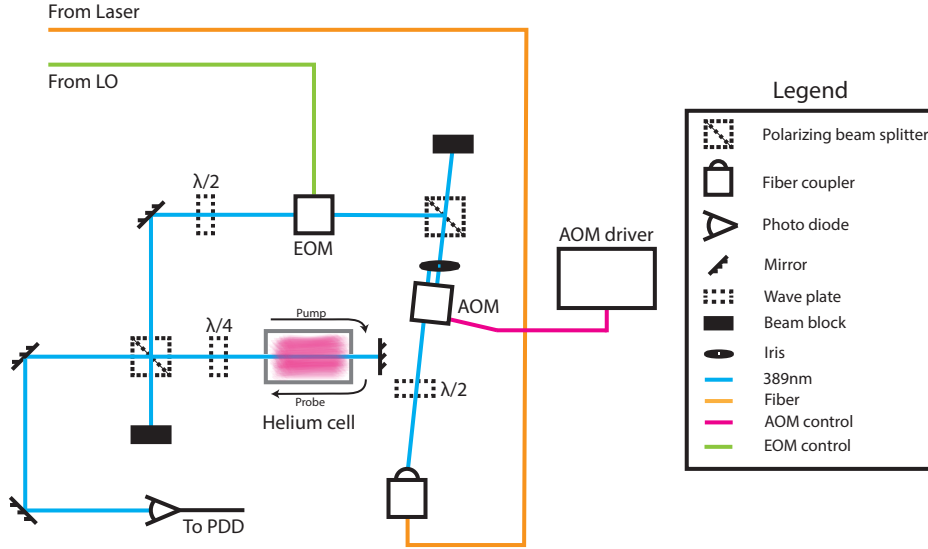

Fig. 3.25: Overview of the spectroscopy setup.

The laser beam of $\lambda \simeq 389\,\mathrm{nm}$ enters the setup through the orange fiber. To compensate the $400\,\mathrm{MHz}$ shift in the light's frequency from the AOM used to pulse the laser (as seen in Fig. 3.4) we use a second AOM before the spectroscopy cell. The light passing this second AOM also gets a frequency shift of $400\,\mathrm{MHz}$ and we will lock the laser to this shifted frequency. In the end, the light entering the helium chamber for Rydberg excitation has effectively the correct frequency because the two AOMs annul each other.

Afterwards, the beam is modulated by an electro-optic modulator (EOM) of $20\,\mathrm{MHz}$. An EOM is an easy way to phase modulate the light. It can be either be used in free space or fiber coupled. For our given wavelength of $\lambda \simeq 389\,\mathrm{nm}$ a free space EOM has to be used because there are no fiber coupled ones in the near UV. An EOM works best for a distinct polarization which is marked at the casing. In our case, the EOM is installed such that the polarization must be vertical, thus we place it behind a polarizing beam splitter that reflects the p-polarization which is in this case equivalent to a vertical polarization. The EOM is described more accurately in Section 3.3.4.

To maximize accuracy of the locking setup, it is important that pump and probe beam have the same frequency. In our case this is realized by re-using the same beam and reflecting it back at the end of the spectroscopy cell instead of splitting it into two parts. In contrast to a classical pump probe approach, the same beam acts both as pump and probe beam reducing the contrast of the λ-dip in the spectroscopy signal. After passing the spectroscopy cell, the absorption signal is detected with a photo diode at the end of the path. To ensure that the beam does not travel back its original path ones uses a $\lambda/4$ plate before the helium cell in a double-pass configuration

to convert p- to s-polarized light and transmit it through the polarizing beam splitter.

The spectroscopy cell is driven by the electronics described in Section 3.3.2 and a fraction of $\sim 10^{-8}$ of the total helium atoms in the spectroscopy cell is excited to the metastable $2\,^3\mathrm{S}_1$ state. For detection, it is important that the photo diode is fast enough to resolve the sidebands. The minimum bandwidth for our case is therefore $20\,\mathrm{MHz}$. To ensure that the photo diode works with the specified bandwidth it must be connected with a $50\,\Omega$ termination and a $50\,\Omega$ BNC cable. Otherwise the bandwidth is decreased and can be calculated with $f_{\mathrm{bw}} = \frac{1}{2\pi R C_J}$ where R is the termination impedance and $C_J \simeq 40 - 80\,\mathrm{pF}$ the junction capacitance.

For a non-terminated photo diode the impedance is given by the oscilloscope which usually is $1\,\mathrm{M}\Omega$ giving a bandwidth of about $2 - 4\,\mathrm{kHz}$. A termination with $50\,\Omega$ increases the bandwidth to about $40 - 80\,\mathrm{MHz}$. The downside of the termination is that the output voltage is decreased and one must amplify the signal before sending it into an oscilloscope.

The photo diode we use (PDA8A by Thorlabs) has termination and amplification already included and comes with a bandwidth of $50\,\mathrm{MHz}$. However, the quantum efficiency respectively responsivity in the near UV range, especially at $\lambda = 389\,\mathrm{nm}$ is low compared to e.g. light of yellow or red color as seen in Fig. 3.26.
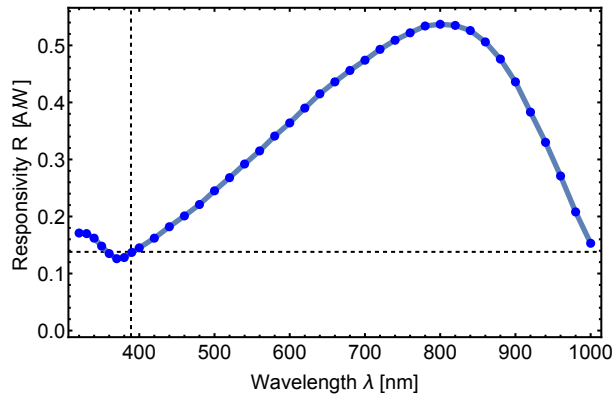

Fig. 3.26: Responsivity curve of the PDA8A. $\lambda = 389\,\mathrm{nm}$ is marked with the dashed lines. Raw data from [48].

Results

The error signal and the transmission profile for the $2\,^3\mathrm{S}_1 \to 3\,^3\mathrm{P}_{1,2}$ transitions that we measure can be seen in Fig. 3.27.

Along the x-axis the frequency of the laser is varied. One spectroscopy peak occurs for each of the transition frequencies (final state $3\,^3\mathrm{P}_1$ and $3\,^3\mathrm{P}_2$) as well as a peak for the crossover.

The crossover resonance arises because the two excited levels are close enough in energy that their Doppler-broadened profiles overlap. Some metastable atoms have a velocity $\vec{v}$ such that $2\,|\vec{k}\cdot\vec{v}| = |f_{3\,^3\mathrm{P}_1} - f_{3\,^3\mathrm{P}_2}|$ and now exhibit a Doppler shift such that the pump beam is absorbed by e.g. the $3\,^3\mathrm{P}_1$ transition. For the probe beam traveling backwards those atoms seem to have a matching velocity component for the $3\,^3\mathrm{P}_2$ frequency to be in resonance with. Since most atoms are already in the upper level the probe beam can pass undisturbed and we see an intensity peak in the absorption spectrum at $f_{\mathrm{crossover}} = f_{3\,^3\mathrm{P}_2} + \frac{|f_{3\,^3\mathrm{P}_1} - f_{3\,^3\mathrm{P}_2}|}{2}$.

The error signal for each transition can be found together with the transmission profile in Fig. 3.27.

However, it is different than the one we see in Fig. 3.22.

To obtain the same shape as in Fig. 3.22 one has to focus on one of the flanks and zoom into it. The distance between the carrier and the sidebands of $20\,\mathrm{MHz}$ is on the same scale as the width of the broadened resonance which is about $30-40\,\mathrm{MHz}$. Therefore, the sidebands are not as distinct as in Fig. 3.22 and one can spot them slightly next to the peak as small dips.
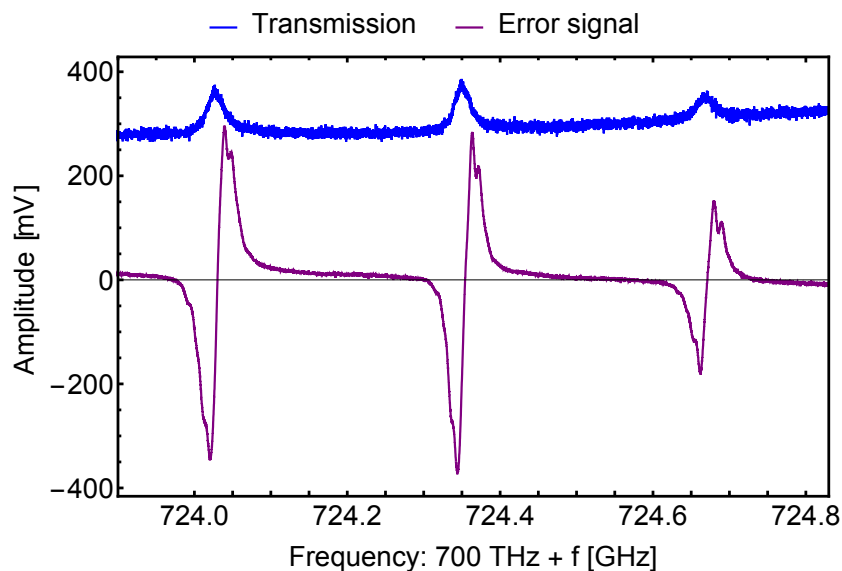

Fig. 3.27: Measurement data for error signal and transmission for J=1 and J=2. The crossover peak is located right between.

The left resonance corresponds to the final state with J=2 at a frequency of $f = 770.7240\,\mathrm{THz}$ whereas the right one results in the state with J=1 at $f = 770.7247\,\mathrm{THz}$. The middle peak arises from the crossover as explained before.

The resonance for J=0 is about $9\,\mathrm{GHz}$ apart from the other two at $f = 770.7328\,\mathrm{THz}$. The curves for the J=0 transition can be found in Fig. 3.28.
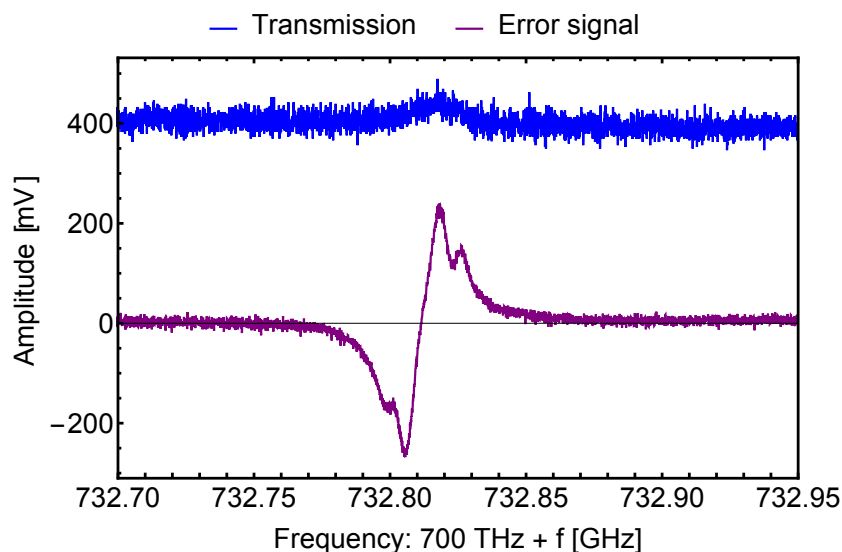

Fig. 3.28: Measurement data for error signal and transmission for J=0.

One can notice that the intensity peak is barely visible because we do not optimize the power of the laser and the pressure in the spectroscopy cell to optimize the signal. However, the error signal is still strong and distinct.

For the actual stabilization the frequency with the strongest error signal is chosen. This is the one with $f = 770.7240\,\text{THz}$ and thus the J=2 final state. The scan range is gradually decreased until one single zero crossing is visible. Then the PID is set to lock the frequency to the point of the zero crossing.

Up to now we can keep the frequency locked for about 2 h. After that time the center wavelength has drifted out of the scan range and the PID cannot detect the zero crossing any more if it needs to relock. Wavelength drifts can occur because of small temperature or current changes.

3.3.4 Electro-optic modulator

As mentioned before, to obtain an error signal and lock the laser we need a phase modulator. In our case we use an EOM that has a modulation frequency which can be tuned between 18.6 and 27.0 MHz with a linewidth of 370 kHz. The frequency is chosen to be 20 MHz because the PDH lock of the doubling cavity to generate the $\lambda \simeq 389\,\text{nm}$ radiation also runs at 20 MHz. By using the same frequency, we are able to drive both modulators using the same source.

Every free space EOM has a distinct axis of polarization that must be matched. For our EOM, the polarization is marked with a line along the casing. We install the EOM in a way that the polarization of the light is vertical.

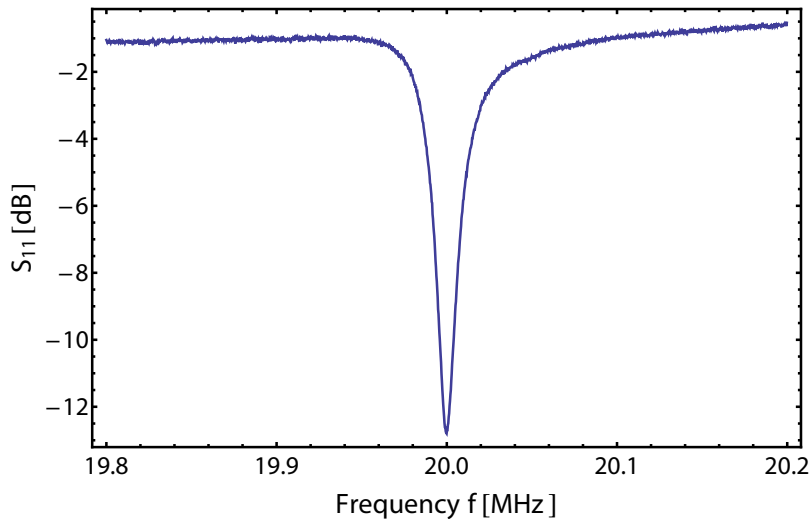The linewidth and resonance frequency of the EOM are measured with a Vector Network Analyzer.

Fig. 3.29: Power absorption by the EOM with resonance at 20 MHz.

To ensure that the EOM works as supposed, we send the light from the laser through a Mach-Zehnder interferometer and place the EOM in one of the arms. The interfering light intensity at one of the fringes is measured with a photodiode. The photodiode is connected to a Spectrum Analyzer that does a Fourier transformation of the intensity signal.

The theoretical explanation of the modulation mechanics seen in Section 3.3.1 can be generalized. If one takes the complete Fourier series into account the we get

$$E = E_0 \, e^{i\omega t + i\beta \sin(\omega_m t)} = E_0 \, e^{i\omega t} \left(J_0(\beta) + \sum_{k=1}^{\infty} J_k(\beta) e^{ik\omega_m t} + \sum_{k=1}^{\infty} (-1)^k J_k(\beta) e^{-ik\omega_m t} \right) \quad (3.1)$$

with J_k being the k-th Bessel function of 1st kind.

Equation 3.1 simplifies to $E \approx E_0 \, e^{i\omega t} \left[1 + J_1(\beta) e^{i\omega_m t} - J_1(\beta) e^{-i\omega_m t} \right]$ in the limit of small β as seen in Section 3.3.1.

Therefore, the amplitude of the k-th sideband should be proportional to $J_k(\beta)$ if we vary the modulation depth β. Fig. 3.30 shows measured data and the corresponding fit. The 1st and 2nd sideband refer to the signal at $f = 20\,\mathrm{MHz}$ and $f = 40\,\mathrm{MHz}$ at the Spectrum Analyzer.
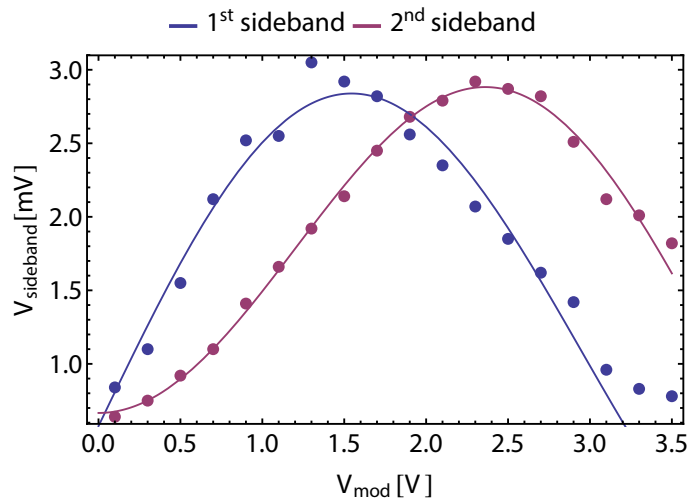

Fig. 3.30: Amplitude of the sidebands. The voltage at the abscissa is linearly proportional to the modulation depth and the voltage at the ordinate is a measure for the amplitude of the corresponding sideband. The solid lines are fits to the k=1 and k=2 Bessel function of 1st kind.

The first sideband has its maximum for a driving voltage of about 1.4 V for an impedance $Z = 50\,\Omega$. Ideally, we want to reach the maximum of the first sideband. Furthermore, we conclude from the measurement that the EOM should not be overdriven to keep the second sideband low. When using the LO of the laser to drive the EOM one must be careful because the LO has a maximum output of 2 V which is split between both modulators. A 1:1 split would result in too little voltage for both of them. To ensure sufficient driving voltages of at least 1.3 V a 2:1 splitter is used. 2/3 of the 2 V enter the internal oscillator. The remaining 1/3 is amplified by 4 dB prior to entering the EOM with a 10 dB amplifier followed by two 3 dB attenuators.

3.3.5 Discharge electronics

The current that drives the oscillating field within the solenoid is supplied by an electronic setup that consists of three main parts as seen in Fig. 3.31.
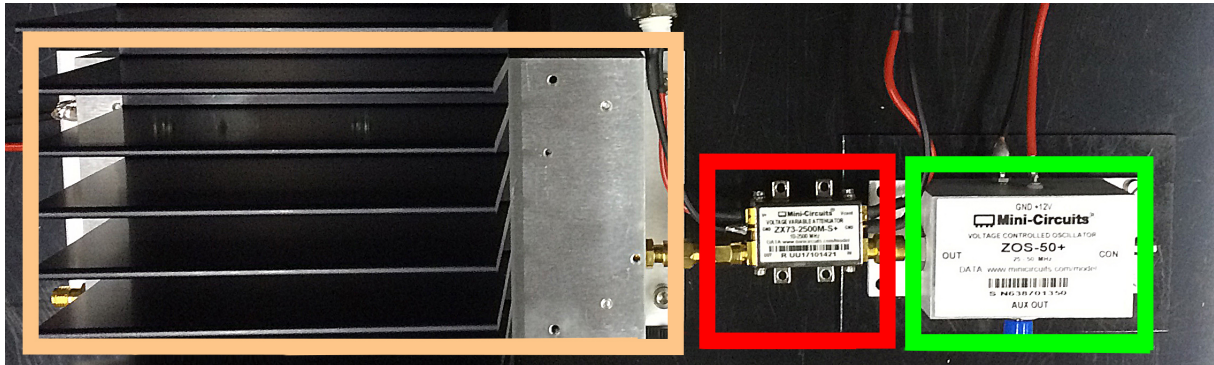

Fig. 3.31: The discharge electronics in the original configuration. Indicated with ▬ is the Voltage Controlled Oscillator (VCO), ▬ the Voltage Controlled Attenuator (VCA) and ▬ the 40 dB amplifier. The black ripped metal part is a passive cooler. The signal exists the setup towards the left.

The oscillation is created by a Voltage Controlled Oscillator (ZOS-50+ by Mini Circuits) which can be tuned between 25 and 50 MHz with an output power of 9 dBm.

The sinusoidal output voltage of the VCO enters a Voltage Controlled Attenuator (ZX73-2500M-S+ by Mini Circuits) which can be tuned between -2 and -80 dB.

Finally, the attenuated signal enters a 40 dB amplifier (ZHL-5W-1 by Mini Circuits) before arriving at the coiled wire around the discharge cell.

In the present configuration the VCA has been replaced by a constant 3 dB attenuator because the VCA suffers from strong back coupling from the amplifier and reacts unstable and unpredictable. With a constant attenuation we achieve a better behaved performance of the circuit. In total, we result in about $40-44$ dBm power through the coils.

Important to note is that the coiled wire and the feed lines act as an antenna and therefore induce noise in surrounding electronic devices depending on their distance to the coil. For a frequency of 27 MHz the electromagnetic radiation has a wavelength of 11 m which is the same magnitude as the size of the lab. Thus, it is possible to have intensity maxima of the resulting standing wave at points about 5 m away from the coil. Hence, we try to set the frequency such that the noise in the surrounding electronic devices is as low as possible.

For future improvements of the experiment the grounding of all components should be examined carefully and improved.

3.4 Electronic setup

3.4.1 Design of the ionization and extraction electrodes

For the distinction between the ns and np state for the same n we use their difference in ionizing electric field. Furthermore, we want to detect the resulting electrones respectively ions on an MCP. Transverse to the beam direction a time-tracing MCP is installed whereas along the beam axis an imaging MCP is located. Hence, ionization and extraction electrodes which are supplied by the switchable voltage source described in Section 3.4.2, are designed to be able to ionize atoms in two perpendicular directions and lead them to the specific MCP. To be able to change between two distinct direction when ionizing a total number of four electrodes is used. The ionization is carried out via pulsed field ionization.

As calculated in Section 2.3.5, the atoms in ns and np states need a certain electric field for being ionized. For dimensioning the electrodes and the required voltages we carry out a simulation beforehand. The dimensions are limited by the size of the double cross and the size of the windows for laser injection as well as by the maximum applicable voltage of 500 V. Furthermore, there should be enough space for the collimated beam of metastables to progress through without colliding with the electrodes.

The results of the simulation which fulfills these requirements best for $n \geq 30$ can be seen in Figures 3.32 and 3.33.
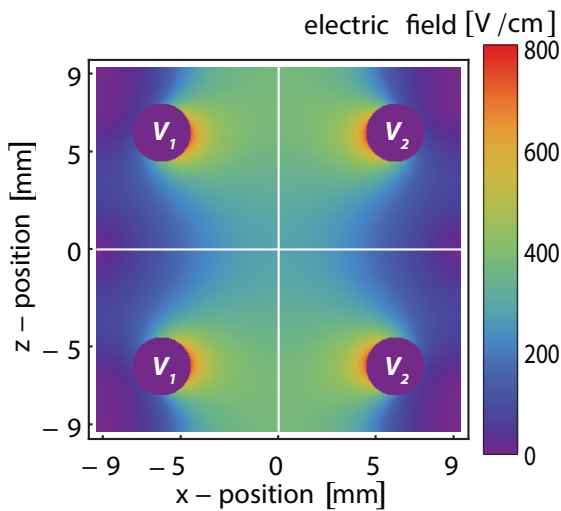

Fig. 3.32: Simulation of the electric field created by the ionization electrodes. The two left electrodes are held at $V_1 = 400\,\text{V}$, the two right ones at $V_2 = 0\,\text{V}$. The electrodes are visible in dark purple and have a diameter of 3 mm with a center distance of 12 mm. The white lines represent slices along symmetry lines visible in Fig. 3.33.
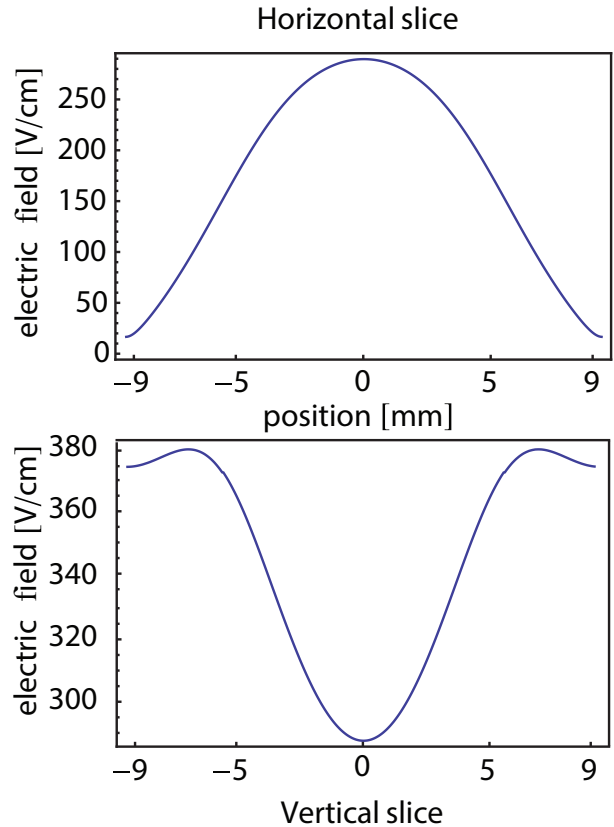

Fig. 3.33: Horizontal and vertical slices through the 2D simulation in Fig. 3.32.

With the simulation at hand, we design the electrodes to have a cylindrical shape with a diameter of $3\,\mathrm{mm}$ arranged at the edges of a square with its centers separated by $12\,\mathrm{mm}$. The diameter of the electrodes increases at the beginning and the end to make them for having a small focusing effect towards the center of the cross. Electrons and ions created during ionization are extracted along the x-direction in the given example configuration. The electric field along x-direction in a range of $\pm 3\,\mathrm{mm}$ around the center is constant with a maximum deviation of $10\,\%$ which is sufficient to ionize Rydberg atoms. The vertical position of the electrode stack can be varied to match the exact beam position.

The lasers travel along the y-direction perpendicular to the helium beam direction.

The electrodes' CAD drawing can be seen in Fig. 3.34 as well as a part of the double cross. The finished and mounted electrodes are shown in Fig. 3.35 as well as in Appendix E.
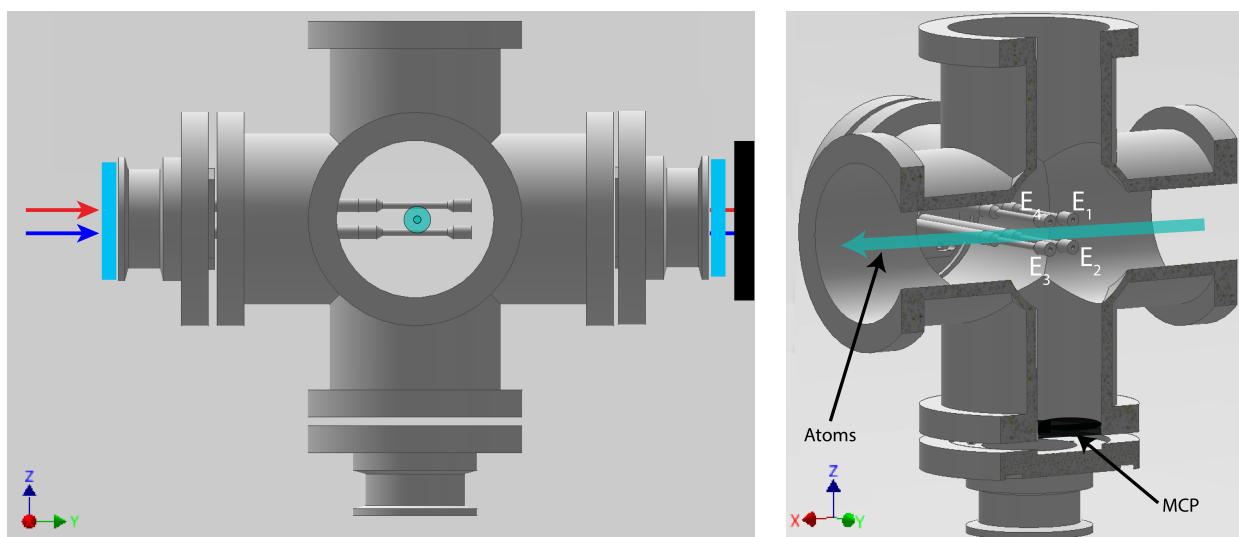

Fig. 3.34: CAD drawing of the extraction electrodes. The atoms (indicated green) move in positive x-direction. The MCP holder can be seen at the bottom (black). Electrodes are labeled E_1 to E_4 in a clockwise direction. The lasers pass along the y-direction.
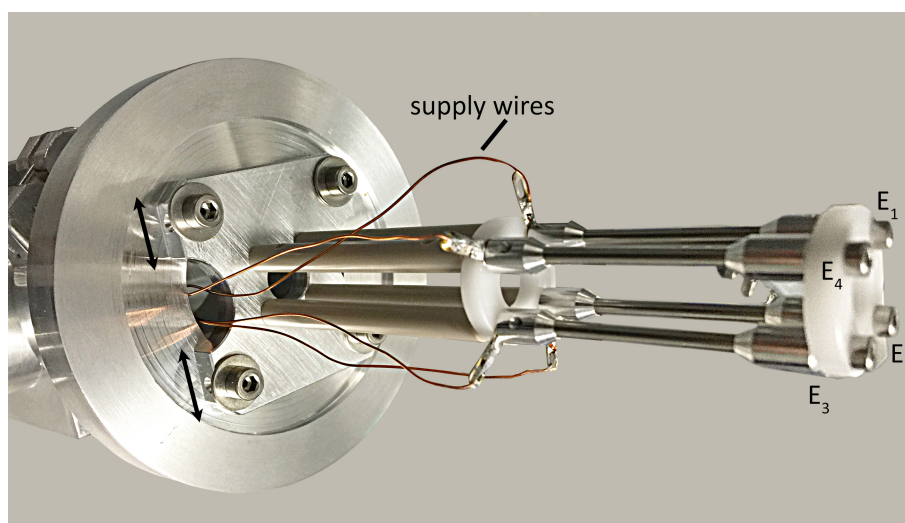

Fig. 3.35: Mounted electrode stack. The supply wires are fed through the vacuum flange.

3.4.2 Design of a switchable voltage source

To achieve an temporal separation of ns and np states a triggered three-level voltage pulser is designed that supplies the electrodes described in Section 3.4.1.

The separation can be realized by the exemplary procedure described in the following for $n = 42$ and outlined in Fig. 3.37. As seen before, the 42s state has a ionizing electric field of $100.9\,\mathrm{V/cm}$ whereas the 42p state needs a field strength of $101.9\,\mathrm{V/cm}$.
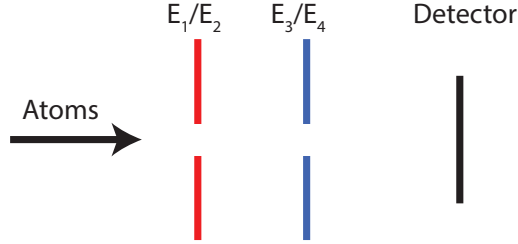

Fig. 3.36: Schematic two-dimensional sketch of the ionization electrodes.

For both triggers being switched off electrodes E_1 and E_2 are held at ground and a constant voltage of $5\,\mathrm{V}$ is applied to electrodes E_3 and E_4, see Fig. 3.36 & 3.37. Upon switching on trigger 1, E_1 and E_2 are set to -96 V which makes a total potential difference of -101 V and as a result an ionization of the 42s state leaving the atoms in 42p ideally untouched. Afterwards, the voltage applied to E_3 and E_4 is switched to $7\,\mathrm{V}$ by a second trigger making a total potential difference of -103 V and thus ionizing the remaining atoms in 42p state.

The exact values for the different voltages need to be found in the real experiment because they strongly depend on the position and direction of the metastable atoms upon entering the electrode stack.
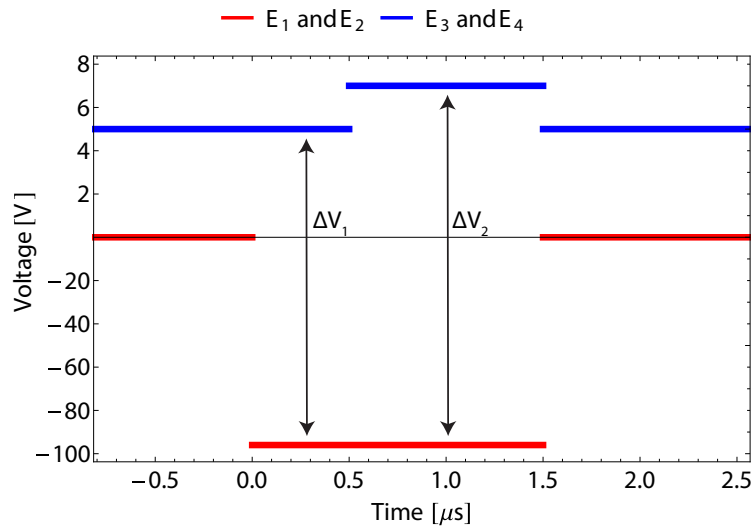

Fig. 3.37: Extraction voltage sequence. $\Delta V_1 = -101\,\mathrm{V}$, $\Delta V_2 = -103\,\mathrm{V}$

The population of both states can be determined by measuring the time trace of the MCP signal and comparing it to the instants of time where the voltage pulses are applied. We want to detect the Rydberg electrons because they are two magnitudes faster than the ion cores ($v_{e^-} \approx 10^7\,\mathrm{m/s}$ and $v_{\mathrm{ion}} \approx 10^5\,\mathrm{m/s}$) and arrive almost instantaneously ($\Delta t_{\mathrm{flight}} < 100\,\mathrm{ns}$) at the MCP. The signal of the ions would be disturbed by the frontmost metastable atoms of the $\sim 300\,\mu\mathrm{s}$ pulse that arrive in the same time interval as the ions produced at the center of the pulse.

The circuit diagram and the PCB design as well as pictures of both boards can be found in Appendix B. The spare copper planes visible in the photos have been sawn off to decrease the coupling capacitances to ground making the circuits more predictable.

Measurement of rise and fall times

For proper ionization a rise time of roughly 100 ns is needed. The pulses itself have a pulse lengths of $200 - 500$ ns. Furthermore, the overshooting after switching the voltages must be as low as possible to ensure a proper distinction between two different states.

High Voltage Switch

The high voltage switch is connected to a supply voltage of $+15$ V and to GND. At the high voltage input a potential of 350 V is applied. Upon sending a trigger pulse into the switch high voltage is applied to the output port.

For testing, a trigger pulse of $100\,\mu$s length and amplitude of 2 V is applied to the trigger input.

The output takes about 300 ns to stabilize to the predefined value of 350 V (Fig. 3.38 a) The overshooting is significant with a maximum measured output voltage of about 600 V as a result of impedance mismatch at the oscilloscope input. The impedance must be matched at the experiment directly for a clean excitation. However, a state distinction would be possible with this switch if we use the peak of the overshooting to ionize the corresponding atoms and fine tune it with the low voltage switch to address the relevant Rydberg atoms only (either ns or np).

Moreover, the switch can provide the defined voltage of 350 V only for a limited amount of time (Fig. 3.38 b). After about $38\,\mu$s the output voltage begins to decrease because of the power storing capacitors depleting and the output voltage begins to decay. However, we want to keep pulse lengths short (about $0.2 - 0.5\,\mu$s) and do not encounter problems caused by the finite pulse length.
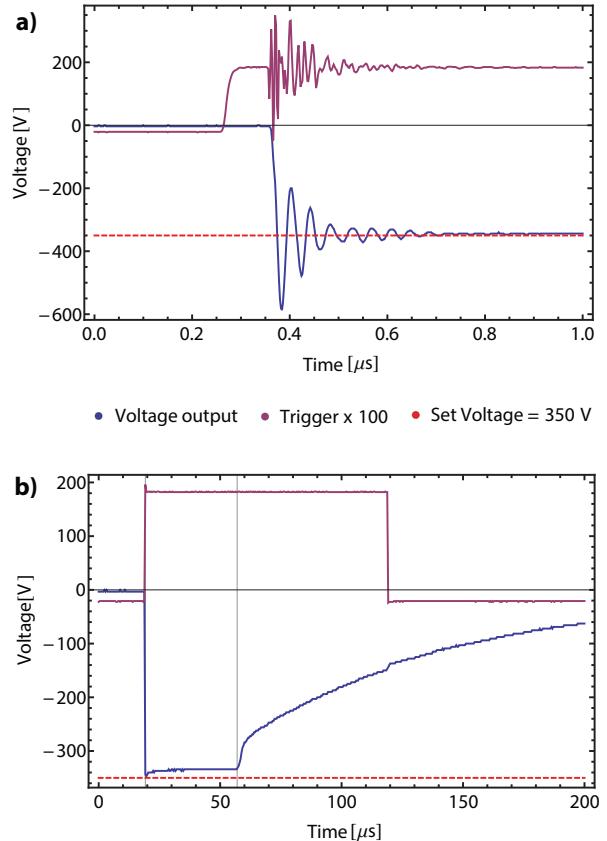

Fig. 3.38: a) Measurement of the switch's rise time. The output is set to be 350 V. One can see the overshooting after the trigger pulse arrives at the switch. b) Measurement of the total pulse with $100\,\mu$s length. The exponential decay of the output voltage is visible.

Likewise, the output voltage does not drop to zero instantaneously because the discharging process of the capacitors follows an exponential decay type behaviour, a result of the RC circuit at the output. Furthermore, we observe strong back coupling from the switch to the trigger because of the coupling through ground.

Low Voltage Switch

The low voltage switch is designed differently than the high voltage switch. Here, two different input voltages can be applied between which can be switched. Furthermore, it requires both +15 V and -15 V as supply voltage besides the usual GND. Circuit explanations can be found in Appendix B.

The switch has a rise and fall time of about 30 ns (Fig. 3.39 a) & b). Moreover, the overshoot is on the order of 1 V. The stabilization process takes 80 ns, a factor of 4 shorter than the HV switch because of the smaller capacitances.

For the low voltage applications, the capacitors have enough capacitance to stabilize the output voltages for more than 100 μs.
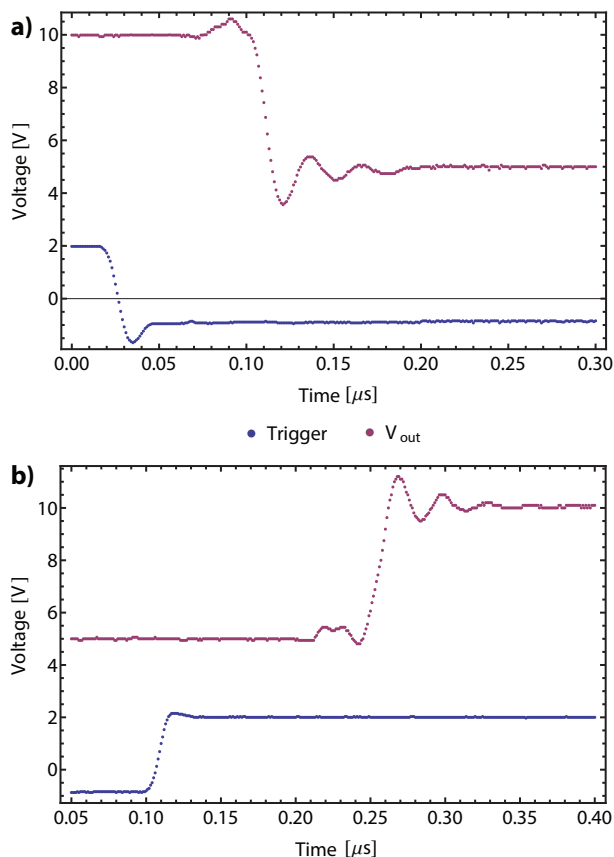

Fig. 3.39: Measurement of the switch's rise and fall time for switching between 5 V and 10 V. The trigger (blue) has a length of 100 μs.

3.4.3 MCP voltage supply and conditioning

The time tracing MCP needs a high voltage supply similar to the imaging MCP already present in the old setup. The circuit diagram and a photograph of the finished voltage supply and the mounted MCP with electrical connections are shown and explained in Appendix D.

A Chevron-type MCP has three inputs and one output [49]. As seen in Fig. 3.40 we must apply a voltage to the Front and Back plate as well as to the Phosphor screen or Metal anode in case of a non-imaging MCP respectively.
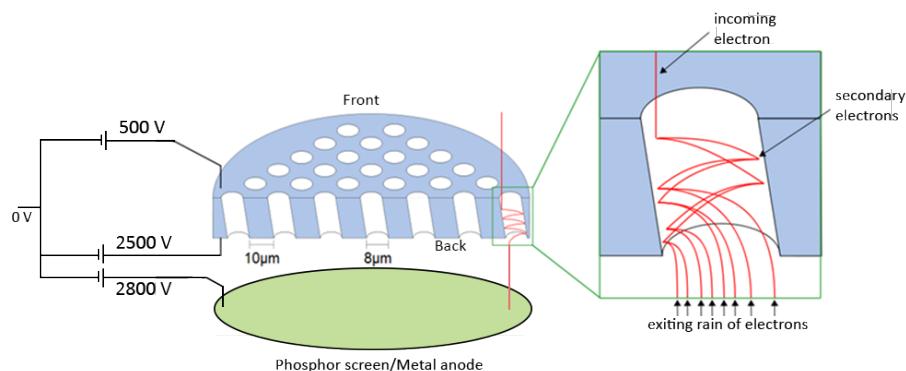

Fig. 3.40: Schematic of an MCP. The front plate is held at $500\,\text{V}$, the back plate at $2500\,\text{V}$ and the metal anode at $2800\,\text{V}$.

To achieve an amplifying effect with the metal anode it must be held at a voltage that is $200-300\,\text{V}$ higher than the voltage at the back plate.

In our case, the voltages at front and back plate are inextricably linked with each other because of a voltage divider. The voltage applied to 'Back in' is divided with a 1:5 ratio between front and back. To achieve the necessary voltages, we apply $2500\,\text{V}$ to the back plate, resulting in $500\,\text{V}$ an the front plate whereas the metal anode is held at $2800\,\text{V}$.

The signal output is realized at the back electrode. If a primary electron hits one of the channels, it is multiplied by secondary electron generation and a current flows from the front to the back plate. The current produces a voltage drop at the back plate which is capacitively coupled to the output port.

Before taking the MCP into operation an Initial Start-up and Electrical Test Procedure must be carried out. The procedure ensures that residual water within the micro channels is removed that can lead to electrical shorts damaging the device. During the procedure the voltages applied to the three inputs are increased on the basis of a given schematic. Depending on the type of particles one want to detect (either positively or negatively charged) the procedure varies slightly. Both procedures can be found on the homepage of the manufacturer [50] and take about $3-6$h each.

3.4.4 Construction of a fast MCP amplifier

For MCP readout a fast amplifier is needed. Single Rydberg electrons produce a peak of $5-10\,\mathrm{ns}$ width and about $1-5\,\mathrm{mV}$ amplitude on the MCP. Thus, the amplifier must have a bandwidth of at least $200\,\mathrm{MHz}$ and a gain of $15\,\mathrm{dB}$ to resolve the signal with respect to the noise. For simplicity we use a preprinted assembly kit designed by Hansjürg Schmutz. The finished board can be seen in Fig. 3.41. The circuit is shown and explained in Appendix F.
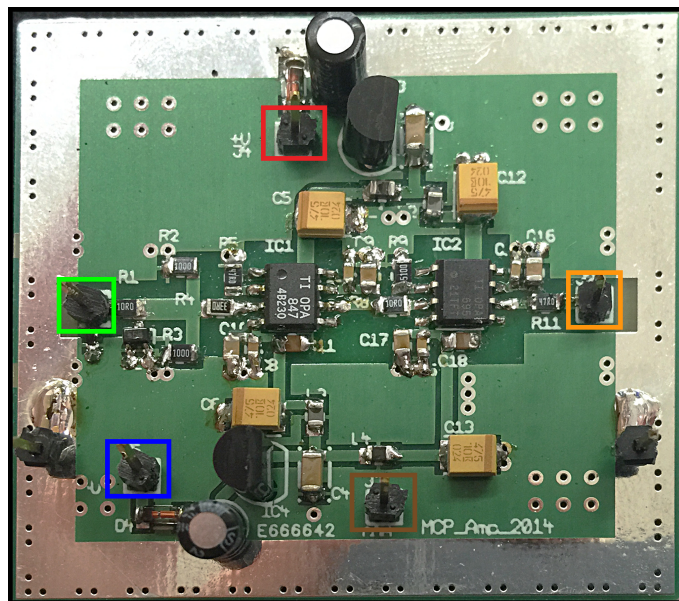

Fig. 3.41: Fast amplifier for MCP readout. Color code: ▬ Input, ▬ Output, ▬ +15 V, ▬ −15 V and ▬ GND.

The amplifier was tested up to $500\,\mathrm{MHz}$ and has a gain of at least $20\,\mathrm{dB}$ up to $310\,\mathrm{MHz}$.

The measured DC amplification for various input voltages can be seen in Fig. 3.42 whereas the gain over a broad bandwidth is plotted in Fig. 3.43.

A linear fit of the data gives $V_{\mathrm{out}} = (6.29 + 13.9 \cdot V_{\mathrm{in}})\,\mathrm{mV}$. The amplification is linear up to $140\,\mathrm{mV}$ input and then saturates to an output voltage of $2100\,\mathrm{mV}$. An amplification factor of 13.9 in voltage translates into $11.5\,\mathrm{dB}$ voltage gain respectively about $23\,\mathrm{dB}$ power gain .

The saturation voltage of $2100\,\mathrm{mV}$ is not reached by a typical MCP signal that usually is about about $50-300\,\mathrm{mV}$ after amplification. In the experiment, because of high impedance, nearby electronics couple capacitively into the output signal. In the worst case this is of similar magnitude as the signal. Further shielding and proper grounding of the setup can improve this.
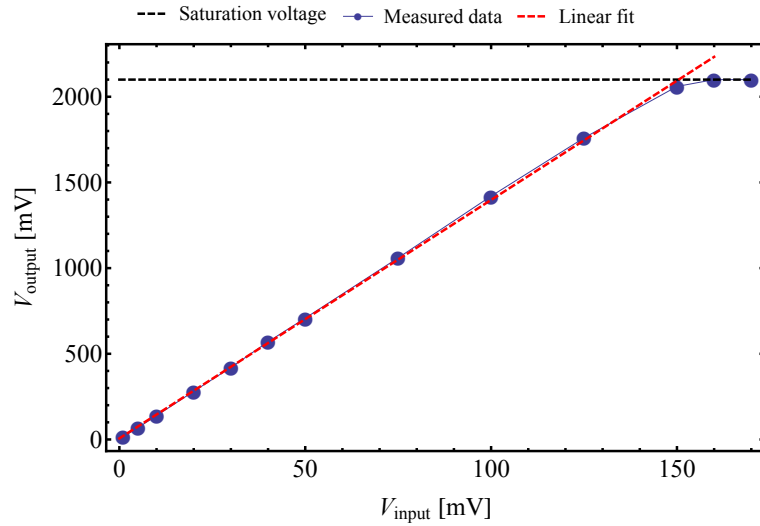
Fig. 3.42: DC amplification of the fast amplifier. At DC input it has a power gain of 23 dB.
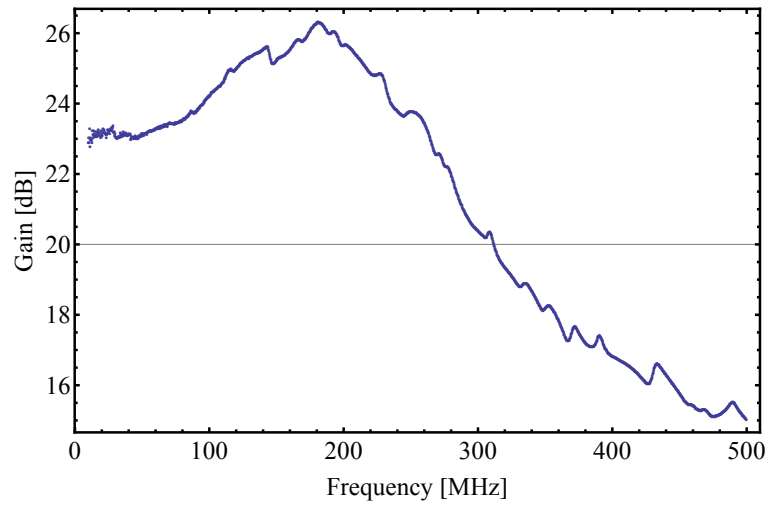

Fig. 3.43: Gain bandwidth of the fast amplifier for an input power of $-40\,\mathrm{dBm}$.

CHAPTER 4

Quest for Rydberg atoms

4.1 Procedure

With all components working the quest for Rydberg atoms can be attempted. In a first step, the distinction between ns and np states is not considered as there should be only a little amount of atoms in the np states. The trigger scheme for mestable helium production, Rydberg excitation, subsequent extraction and detection is sketched in Fig. 4.1.
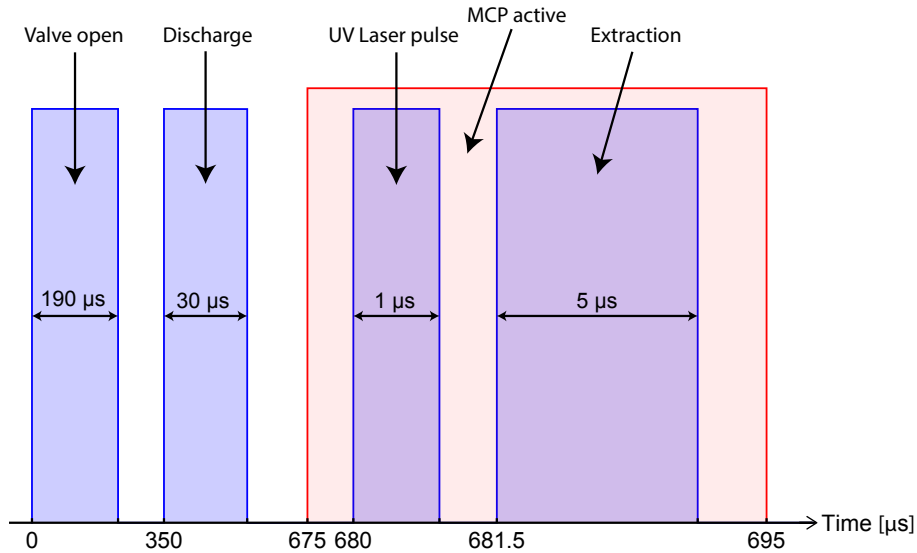

Fig. 4.1: The trigger scheme for Rydberg excitation. The 0 is measured from the trigger that opens the valve.

A trigger pulse is sent to the valve at time $t = 0$ with a length of $190\,\mu$s. During this time a helium pulse expands into the source chamber. Because the actual time of the opening cannot be measured directly, we find it by optimizing the amount of metastable helium atoms produced by the discharge. The maximum amount of metastable helium atoms is achieved for a delay of the AC discharge pulse by $350\,\mu$s at a voltage of $200\,$V. The length of the discharge pulse is as small as possible with maximum signal which is about $30\,\mu$s.

The metastable atoms travel at about $1.7 - 2.0\,\frac{\text{mm}}{\mu\text{s}}$ such that the peak reaches the the Rydberg excitation region about $300\,\mu$s after the end of the discharge pulse. The UV laser is switched on at $t = 680\,\mu$s for $1\,\mu$s whereas the red laser is continuously lasing. An extraction voltage of $900 - 1200\,$V is applied $500\,$ns after the end of the UV laser pulse for $5\,\mu$s and the MCP is active during excitation and detection to measure metastable atoms, Rydberg ions and Rydberg

electrons continuously to determine the instance of time where Rydberg ions or electrons are supposed to arrive. The time interval is set between $t = 675\,\mu$s and $t = 695\,\mu$s. In principle, the Rydberg electrons (ions) should arrive $20 - 40\,$ns $(1 - 3\,\mu$s) after beginning of the extraction pulse.

4.2 MCP traces

4.2.1 Metastable helium atoms

For comparison the measurement data of metastable helium atoms with an unpulsed MCP is shown in Fig. 4.2.
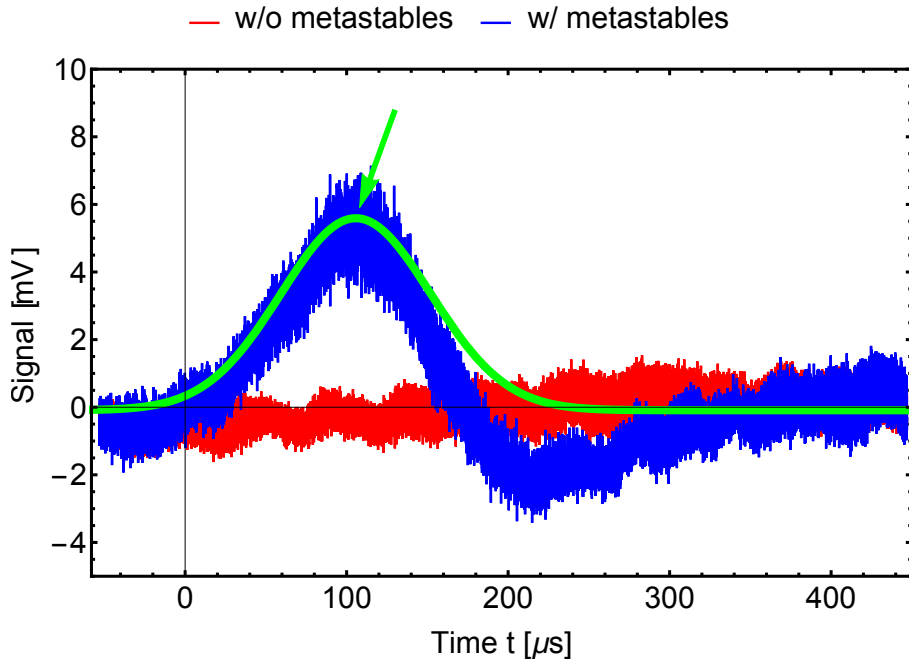

Fig. 4.2: MCP trace with (blue) and without (red) metastable helium atoms. The trace has been averaged 100 times.

The red trace is the data without metastable helium atoms present. The noise level is about $\pm 1\,$mV. With metastable atoms we measure a broadened peak of $V_{\mathrm{pp}} \approx 6\,$mV height and a width of about $110\,\mu$s determined from the fit. Both traces are measured with an unpulsed MCP.

The zero point in time is again set to the beginning of the extraction pulse and it takes the metastable atoms about $110\,\mu$s to reach the MCP which coincides with what we assumed. The distance between the extraction electrodes and the MCP is about $200\,$mm which translates into $100 - 120\,\mu$s time of flight with a velocity of $1.7 - 2.0\,\frac{\mathrm{mm}}{\mu s}$. In the trigger scheme from Fig. 4.1 the UV laser is set to excite atoms within a $1\,\mu$s window at the maximum of the atom pulse indicated with the green arrow. Hence, we can roughly estimate that Rydberg atoms should arrive at the MCP between $t = 0\,\mu$s and $t = 100\,\mu$s.

4.2.2 Overview

To find the regions of interest we take a measurement of the total trace of the MCP in a pulsed mode. A visualization of the data can be seen in Fig. 4.3 with its zero point set to the beginning of the extraction.
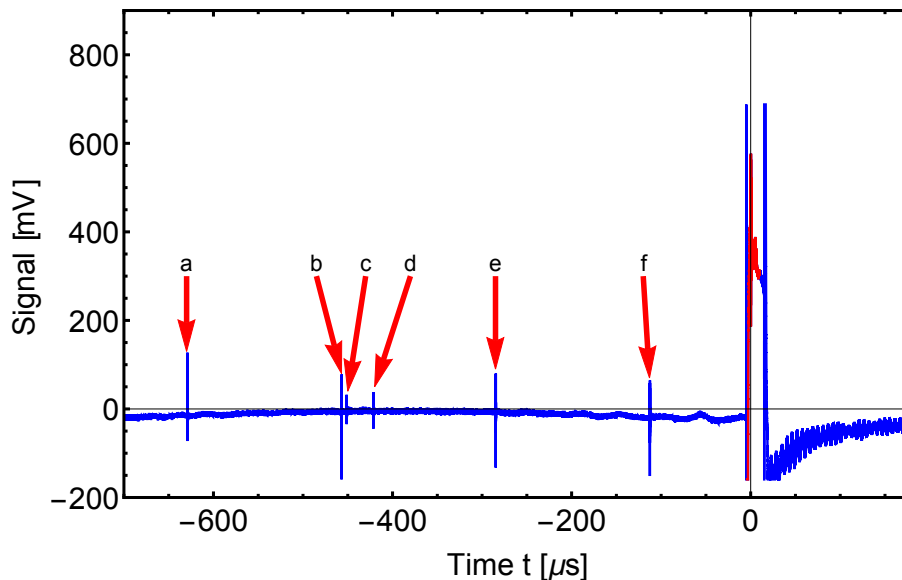

Fig. 4.3: Total trace of the MCP. The region where Rydberg atoms are expected is indicated in red.

The peaks that are marked with a−f are due to trigger coupling through the ground. During the switching a high current is flowing due to the fast change in voltage and new charges cannot be provided by the ground fast enough. This leads to an effective potential difference that is measured by the MCP. The triggers as explained in Section 4.1 and Fig. 4.1 are highlighted in Fig. 4.3. Point a, b, e, f arise from periodic recharging of the extraction switch. Point c and d outline the beginning and end of the discharge that produces the metastable atoms.

Rydberg electrons can be measured in the region right after the extraction trigger (Fig. 4.4).
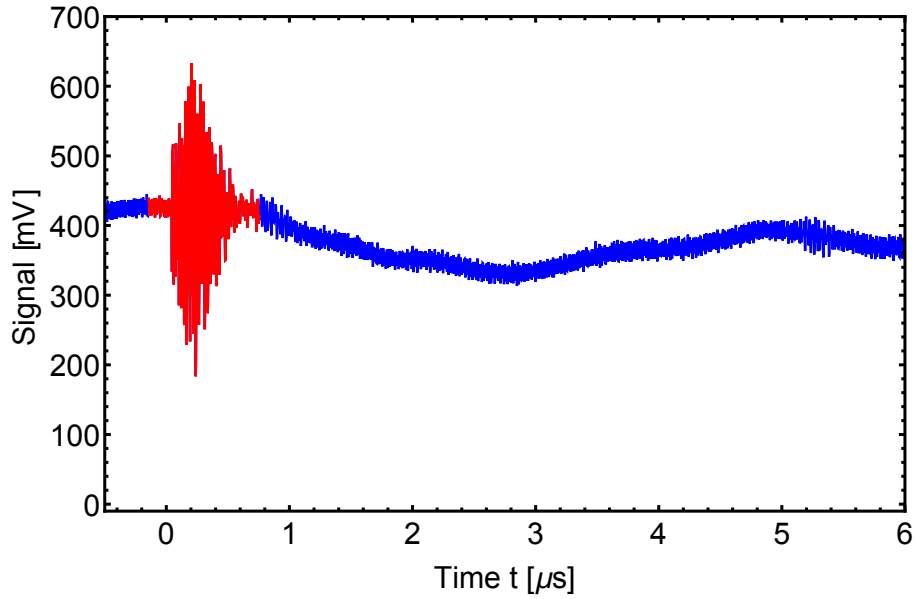
Fig. 4.4: Magnified cut of the total MCP trace for the region where Rydberg ions and electrons are expected. The region where Rydberg electrons are expected is indicated in red. The ions are expected about $1.5\,\mu$s later.

For detection of both Rydberg ions or electrons, the trace with couplings present is averaged about 200 times and then stored locally on the oscilloscope. Next, the stored data is subtracted from the ongoing measurement. In principle, the trace is now flat because the coupling is nearly constant in time and distinct spikes appear when Rydberg ions or electrons hit the MCP. The spikes have a height of about $50-200\,$mV and a width of about $50\,$ns.

4.2.3 Rydberg MCP traces

A first trace of the MCP with Rydberg ions present has been taken (Fig. 4.5) using an ionization voltage of 1200 V. To record the trace we subtract the background measured in Fig. 4.4.
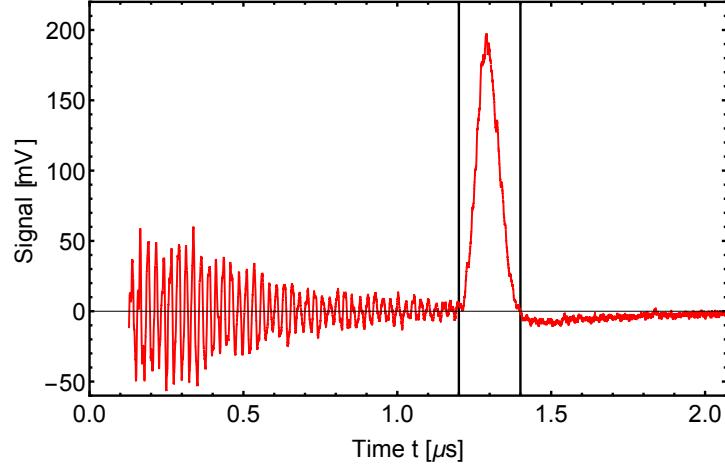

Fig. 4.5: MCP trace with Rydberg atoms. The signal is integrated between the two black marks for further processing.

The signal is used to find the temporal region where Rydberg ions arrive at the MCP. To quantify the signal we integrate between two instants in time indicated in the figure with the black marks. The total integration time is about $150 - 200$ ns depending on the width of the signal. The integrated signal is used in the following measurements as a measure for the number of Rydberg atoms.

For the measurement in Fig. 4.6 the wavelength is set to the 33d transition and the ionization voltage is varied. Four different voltages are compared.
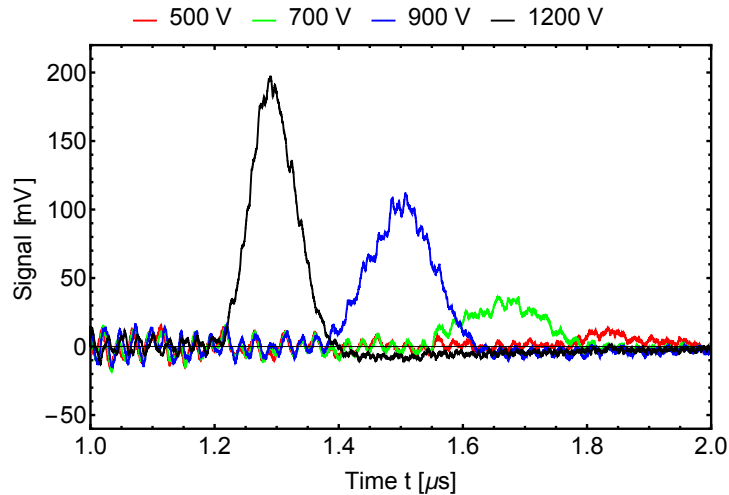

Fig. 4.6: MCP trace for the 33d state and different ionization voltages.

As expected, the ions take a longer time to reach the MCP for smaller voltages due to their lower velocity. Furthermore, the signal broadens due to the slower ionization until it dies out below 500 V. The velocities can be calculated with knowledge of the time needed to reach the MCP and the distance between extraction electrodes and MCP. From the velocity an effective accelerating

potential difference can be calculated with $q \cdot U = \frac{1}{2}mv^2$. Additionally, the area below the peak can be calculated by integrating a corresponding Gaussian fit.

Voltage applied	Time measured	Velocity	Effective potential	Area below peak
500 V	1.85 μs	122.7 $\frac{mm}{\mu s}$	312.7 V	1.02 a.u.
700 V	1.66 μs	136.7 $\frac{mm}{\mu s}$	388.1 V	4.66 a.u.
900 V	1.50 μs	151.3 $\frac{mm}{\mu s}$	475.5 V	12.66 a.u.
1200 V	1.29 μs	176.0 $\frac{mm}{\mu s}$	643.4 V	16.42 a.u.

Table 4.1: Comparison of applied and effective potential. The distance between electrodes and MCP used to calculate the velocity is 227.0 mm.

The data shows that the effective potential difference is about half of the actual applied voltage. This behaviour can be explained by considering the position of ionization to be the center of the electrodes. During the flight through the first half of the electrodes, the neutral Rydberg atoms are not accelerated by the field. After being ionized, the created ion cores are accelerated with the remaining potential difference of about half the initial difference.

Furthermore, the area below the Rydberg peak is calculated. In principle, it should be constant as it is a measure for the total number of Rydberg atoms. However, we see that the area and hence the number of Rydberg atoms declines. We think that the decline is a result of partial ionization for smaller fields resulting from a mix of diabatic and adiabatic ionization processes.

4.3 Rydberg atoms

A first measurement of the 34s state is taken with Rydberg ions without an external electric field being applied (Fig. 4.7). For each data point a section of the MCP trace is integrated as explained before. The maximum of the individual data points is then normalized to unity and they are plotted versus the difference to the field free transition frequency. A Gaussian fit allows to extract the transition frequency and the linewidth.
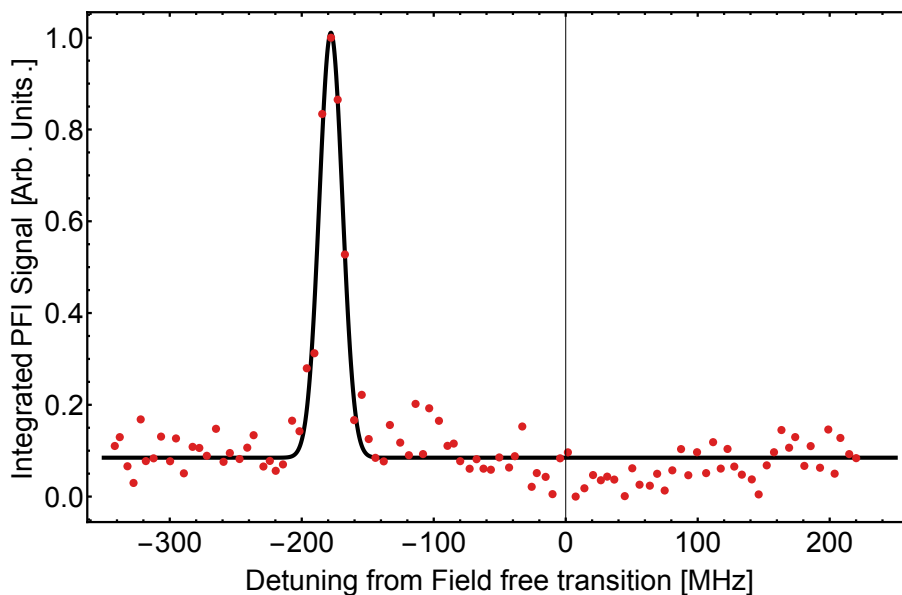

Fig. 4.7: Integrated pulsed field ionization signal of the 34s state. The Gaussian fit yields a transition frequency of 382118.482 GHz and an FWHM of 20.596 MHz.

The systematic deviation from the field free transition frequency due to absolute inaccuracy of the wavemeter of 200 MHz. However, the relative accuracy is 10^{-6} which makes the data points consistent compared to each other. The line is broadened from the expected natural linewidth of $1 - 5$ MHz to 20.596 MHz due to power broadening that for $I = 300 \, I_{\text{sat}}$ gives a factor of about 17.

In a second measurement, an external field is applied to one pair of electrodes to measure the quadratic Stark effect. With unknown stray fields F_0 and systematic errors in the frequency measurement Δ_{offset} the quadratic Stark shift takes the form

$$\Delta_0(F) = \frac{\alpha}{2}(F - F_0)^2 + \Delta_{\text{offset}}. \tag{4.1}$$

The corresponding transition frequency is extracted from numerical fits and plotted versus the applied field in Fig. 4.8.
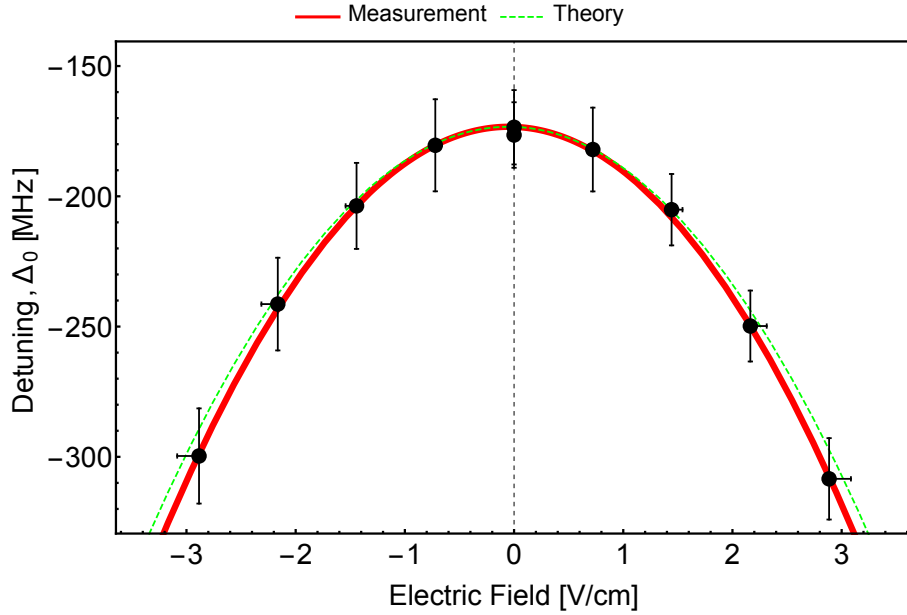

Fig. 4.8: Measurement of the quadratic Stark shift (black dots) in comparison to the theoretical curve (green dashed line). The red curve is fitted to equation 4.1.

The data in Fig. 4.8 shows the expected quadratic behaviour. A fit to equation 4.1 gives $\alpha = -31.2\,\text{MHz}\,(\text{V/cm})^{-2}$, $\Delta_{\text{offset}} = -173.3\,\text{MHz}$ and $F_0 = -0.048\,\text{V/cm}$. Theoretical calculations give $\alpha_{\text{theo}} = -28.8\,\text{MHz}\,(\text{V/cm})^{-2}$. The error bars in the electric field result from the inaccurate conversion between applied voltages and resulting electric fields. Because of the shape of the electric field, the error is only towards larger values. The error in measured frequency is given by the widths of the fits to the single spectra.

CHAPTER 5

Conclusion and Outlook

5.1 Conclusion

During my Master thesis the theoretical aspects of Rydberg atoms are analyzed and investigated experimentally. In the course of the last four months, the existing prototype of the new helium source has been modified and the main components for triplet Rydberg excitation have been taken into operation. The setup is brought to a stage where it is possible to create and measure Rydberg atoms.

For Rydberg excitation two new laser systems are set up. In the case of the UV laser the frequency is locked to the $2\,^3S_1 \rightarrow 3\,^3P_2$ transition. This is achieved by use of the Pound-Drever-Hall technique in combination with Dopplerfree saturation spectroscopy. The electronic components needed for the stabilization are gauged and well understood. Moreover, the frequency of the red laser is controllable via a LabView application to a precision of 10^{-6} nm or 2 MHz respectively by a motor in combination with a piezo-electric element.

Furthermore, optical access to the region of Rydberg excitation is established with both lasers aligned collinearly through the setup. The red laser is used in cw operation with a power of 1.7 W, whereas the UV laser is operated in a pulsed mode. The power used to drive the $2\,^3S_1 \rightarrow 3\,^3P_2$ transition is about $5 - 30$ mW depending on the explicit measurement. For detection, Rydberg atoms can be ionized by pulsed field ionization and guided to one of two MCPs by the electric field created by the electrodes. The pulsed field ionization is realized with a three-stage switch consisting of two independent circuits that supplies custom designed electrodes and is in principle capable of distinguishing between ns and np states.

The MCP signal measured with an oscilloscope can directly be loaded into the LabView control and read-out application. For further investigation, the traces can be integrated and the data exported to be analyzed with e. g. Mathematica.

Recapitulating, the goal of Rydberg excitation including read-out and data analysis of metastable $2\,^3S_1$ helium has been achieved.

5.2 Outlook

In this thesis the foundations for creation of triplet helium Rydberg atoms has been laid. For better comprehension of the new Rydberg source various aspects can be improved and investigated. A brief outlook of the tasks for the near future is given subsequently.

First, the Rydberg signal must be improved and stabilized by e.g. enhancing the overlap of the two lasers, adjusting the timings of the various pulses and the detuning of the lasers. In addition, an optimum laser power has to be found to make a compromise between signal strength and power broadening of the signal linewidth.

Second, measurements of complete Stark manifolds and Rydberg spectra can be taken and analyzed to verify the theoretical considerations. Furthermore, the capability of wide-range tuning the red laser can be quantified.

Third, parts of the designed and constructed electronic components like the amplifiers couple into high impedance RF and voltage sources. The coupling happens most likely through the ground and hence the components demanding high currents must be shielded and grounded more thorough. Concepts for better shielding and grounding can be developed together with Hansjürg.

Fourth, a new valve capable of opening and injection helium at a repetition rate of 1 kHz is supposed to be installed, tested and characterized. With the higher repetition rate and the increased gas flux the new valve puts additional stress on the cooling. Currently, the cooling is done via water circulation. In the future, one must switch to a liquid nitrogen cooling.

Finally, the new Helium source must be combined with the existing Rydberg experiment and tested in the new configuration. The design of a mounting arrangement and the assemblage is carried out within the work of Jonas Künzli. The connection of the two experiments is crucial for the future progress of the Hybrid Quantum systems project. With an increased repetition rate of 1 kHz and a transversally cooled helium beam the precision of the measurements at the Rydberg experiment can be increased drastically.

Acknowledgments

First of all, I would like to thank the whole Qudev Team for the support and the good atmosphere within the group. My special thanks goes to Prof. Andreas Wallraff. I am obliged that I was able to work within his group at this interesting experiment.

Furthermore, I thank Tobias Thiele for being a great advisor. His knowledge and experience about physics in general and especially optics amazed me many a time. I appreciate his ability to work for tens of hours straight while staying fully motivated.

Moreover, very thanks to Mathias Stammeier. I enjoyed the time I spend in the lab together with him, soldering cables and boards and looking out for Rydberg atoms.

In addition, I want to thank Johannes Deiglmayr for his support while I struggled during the beginning of my thesis. Special thanks to Hansjürg, Seppi, Jonas and Janis for their technical assistance and Francesca Bay and Gabriela Strahm for their administrative support.

I thank Bianca Friese for helping me with editing and improving the photographs.

And last but not least, I want to thank my girlfriend for supporting me mentally and physically and letting me spend much time in the lab. Even though I was more in the lab than at home she still stuck with me.

Bibliography

[1] D. R. Murdoch. *Niels Bohr's Philosophy of Physics*. Cambridge University Press, 1987. Cambridge Books Online.

[2] Max Born. *Physik im Wandel meiner Zeit*, volume 4. Auflage. Vieweg & Sohn, 1966.

[3] Jagdish Mehra and Helmut Rechenberg. *The Historical Development of Quantum Theory: The Completion of Quantum Mechanics*. Springer, 2000.

[4] Xiao-Song Ma, Thomas Herbst, Thomas Scheidl, Daqing Wang, Sebastian Kropatschek, William Naylor, Bernhard Wittmann, Alexandra Mech, Johannes Kofler, Elena Anisimova, Vadim Makarov, Thomas Jennewein, Rupert Ursin, and Anton Zeilinger. Quantum teleportation over 143 kilometres using active feed-forward. *Nature*, 489(7415):269–273, September 2012.

[5] F. S. Luiz and Gustavo Rigolin. Teleportation-based continuous variable quantum cryptography. August 2014.

[6] Dina Genkina, Giulio Chiribella, and Lucien Hardy. Optimal probabilistic simulation of quantum channels from the future to the past. *Phys. Rev. A*, 85,:022330, December 2011.

[7] A. Chiuri, C. Greganti, M. Paternostro, G. Vallone, and P. Mataloni. Experimental quantum networking protocols via four-qubit hyperentangled dicke states. *Phys. Rev. Lett.*, 109,:173604, December 2011.

[8] Muhammad Nadeem. Quantum non-locality, causality and mistrustful cryptography. July 2014.

[9] David DiVincenzo. The physical implementation of quantum computation. 2007.

[10] J. A. Jones and M. Mosca. Implementation of a quantum algorithm to solve deutsch's problem on a nuclear magnetic resonance quantum computer. *J.Chem.Phys.*, 109:1648–1653, 1998.

[11] M. Ebert, M. Kwon, T. G. Walker, and M. Saffman. Coherence and rydberg blockade of atomic ensemble qubits. January 2015.

[12] Yoon-Ho Kim. Single-photon two-qubit "entangled" states: preparation and measurement. *Phys. Rev. A*, 67,:040301(2003), 2003.

[13] Arne Laucht, Rachpon Kalra, Juha T. Muhonen, Juan P. Dehollain, Fahd A. Mohiyaddin, Fay Hudson, Jeffrey C. McCallum, David N. Jamieson, Andrew S. Dzurak, and Andrea

Morello. High-fidelity adiabatic inversion of a ^{31}P electron spin qubit in natural silicon. December 2013.

[14] Gui Lu Long and Li Xiao. Experimental realization of a fetching algorithm in a 7 qubit nmr quantum computer. *J. Chem.Phys.*, 119,:8473–8481, 2003.

[15] Jingfu Zhang, Wenzhang Liu, Zhiwei Deng, Zhiheng Lu, and Gui Lu Long. Modularization of multi-qubit controlled phase gate and its nmr implementation. *J. Opt. B: Quantum Semiclass. Opt.*, 7,:22, 2005.

[16] J. Q. You, Xuedong Hu, S. Ashhab, and Franco Nori. Low-decoherence flux qubit. *Phys. Rev. B*, 75,:140515(2007), 2006.

[17] Zhen-Tao Zhang and Yang Yu. Processing quantum information in hybrid topological qubit and superconducting flux qubit system. December 2012.

[18] Y. Nakamura, Yu. A. Pashkin, and J. S. Tsai. Coherent control of macroscopic quantum states in a single-cooper-pair box. 2009.

[19] Jian-Qi Zhang, Wei Xiong, Shuo Zhang, Yong Li, and Mang Feng. Generating the schrodinger cat state in a nanomechanical resonator coupled to a charge qubit. May 2014.

[20] Tae-Wan Noh, Mun Dae Kim, and H. S. Sim. Superconductor-ferromagnet junction phase qubit. *J. Korean Phys. Soc.*, 60,:72, April 2008.

[21] Zhan Shi, C. B. Simmons, J. R. Prance, John King Gamble, Teck Seng Koh, Yun-Pil Shim, Xuedong Hu, D. E. Savage, M. G. Lagally, M. A. Eriksson, Mark Friesen, and S. N. Coppersmith. A fast "hybrid" silicon double quantum dot qubit. *Phys. Rev. Lett.*, 108,:140503, October 2011.

[22] Peter W. Shor. Polynomial-time algorithms for prime factorization and discrete logarithms on a quantum computer. *SIAM J.Sci.Statist.Comput.*, 26:1484, 1997.

[23] Thorsten Kleinjung, Kazumaro Aoki, Jens Franke, ArjenK. Lenstra, Emmanuel Thomé, JoppeW. Bos, Pierrick Gaudry, Alexander Kruppa, PeterL. Montgomery, DagArne Osvik, Herman te Riele, Andrey Timofeev, and Paul Zimmermann. Factorization of a 768-bit rsa modulus. In Tal Rabin, editor, *Advances in Cryptology – CRYPTO 2010*, volume 6223 of *Lecture Notes in Computer Science*, pages 333–350. Springer Berlin Heidelberg, 2010.

[24] Thomas Monz, Philipp Schindler, Julio T. Barreiro, Michael Chwalla, Daniel Nigg, William A. Coish, Maximilian Harlander, Wolfgang Hänsel, Markus Hennrich, and Rainer Blatt. 14-qubit entanglement: Creation and coherence. *Physical Review Letters*, 106:130506, Mar 2011.

[25] Erik Lucero, Rami Barends, Yu Chen, Julian Kelly, Matteo Mariantoni, Anthony Megrant, Peter O'Malley, Daniel Sank, Amit Vainsencher, James Wenner, Ted White, Yi Yin, Andrew N. Cleland, and John M. Martinis. Computing prime factors with a josephson phase qubit quantum processor. February 2012.

[26] Nikesh S. Dattani and Nathaniel Bryans. Quantum factorization of 56153 with only 4 qubits. November 2014.

[27] M. H. Devoret, A. Wallraff, and J. M. Martinis. Superconducting qubits: A short review. 2007.

[28] Jonathan D. Pritchard. *Cooperative Optical Non-Linearity in a Blockaded Rydberg Ensemble*. Springer Berlin Heidelberg, 2012.

[29] Laboratoire Kastler Brossel, http://www.cqed.org/spip.php?article119&lang=de, visited on 28 Dec 2014.

[30] T. Thiele, S. Filipp, J. A. Agner, H. Schmutz, J. Deiglmayr, M. Stammeier, P. Allmendinger, F. Merkt, and A. Wallraff. Manipulating rydberg atoms close to surfaces at cryogenic temperatures. *Phys. Rev. A*, 90:013414, Jul 2014.

[31] Robert S. Van Dyck, Charles E. Johnson, and Howard A. Shugart. Radiative lifetime of the $2\ ^1s_0$ metastable state of helium. *Phys. Rev. A*, 4:1327–1336, Oct 1971.

[32] S. S. Hodgman, R. G. Dall, L. J. Byron, K. G. H. Baldwin, S. J. Buckman, and A. G. Truscott. Metastable helium: A new determination of the longest atomic excited-state lifetime. *Phys. Rev. Lett.*, 103:053002, Jul 2009.

[33] NIST Data Base
”`http://physics.nist.gov/PhysRefData/ASD/lines_form.html`”.

[34] Tobias Thiele. QSIT Lecture 8 FS 2014
”`http://www.qudev.ethz.ch/node/59934`”.

[35] Constantine E. Theodosiou. Lifetimes of singly excited states in He I. *Phys. Rev. A*, 30:2910–2921, Dec 1984.

[36] J. J. Sakurai. *Modern Quantum Mechanics (Revised Edition)*. Addison Wesley, 1 edition, September 1993.

[37] Myron L. Zimmerman, Michael G. Littman, Michael M. Kash, and Daniel Kleppner. Stark structure of the rydberg states of alkali-metal atoms. *Phys. Rev. A*, 20:2251–2275, Dec 1979.

[38] Thomas Gallagher. *Rydberg Atoms*. Springer New York, 2006.

[39] Lukas Gerster. Metastable Helium source. 2014.

[40] Max Melchner. Collimation of metastable He. 2014.

[41] Dominik Friese. Deflection of metastable Helium via Laser light. 2014.

[42] Toptica TA/FA SHG pro Product page
”`http://www.toptica.com/products/research_grade_diode_lasers/frequency_converted_diode_lasers/ta_shg_pro_frequency_doubled_high_power_tunable_laser.html`”.

[43] Testclue Blog. What is fiber optics?
"http://blogs.testclue.com/fiber-optics/".

[44] Altechna. Dual AR Coated Windows (DAR)
"http://www.altechna.com/product_details.php?id=871".

[45] Altechna. Wavelength Separators
"http://www.altechna.com/product_details.php?id=867".

[46] Pound-Drever-Hall technique
"http://en.wikipedia.org/wiki/Pound-Drever-Hall_technique".

[47] Christopher J. Foot. *Atomic Physics*. Oxford, 1st edition, 2005.

[48] Thorlabs. Si Transimpedance Amplified Photodetectors
"http://www.thorlabs.com/newgrouppage9.cfm?objectgroup_id=3257&pn=PDA8A".

[49] Mario S Könz and Tobias Thiele. Design , Build-up and Control of Electronic Equipment
for the Hybrid Rydberg Experiment. 2014.

[50] Photonis - MCP Reference List: MCP (Chevron) Start-up procedure
"http://www.photonis.com/en/content/133-ism-mcp-reference-list".

Appendix

A Rydberg calculations

Transition wavelengths

n	Wavelength λ [nm]	n	Wavelength λ [nm]	n	Wavelength λ [nm]
30	792.2834054266356	56	786.7358959934126	82	785.5662728904583
31	791.7835000185348	57	786.6593851034783	83	785.5418924908304
32	791.3306945550562	58	786.5868312025931	84	785.5183821091006
33	790.9192380187172	59	786.5179658391415	85	785.4957008205936
34	790.5442331353055	60	786.4525429644195	86	785.4738100798683
35	790.2014883538392	61	786.3903367243528	87	785.4526735565803
36	789.8873989845505	62	786.3311395012387	88	785.43225698441
37	789.5988510984064	63	786.2747601736535	89	785.4125280218788
38	789.3331433308123	64	786.2210225671648	90	785.3934561239981
39	789.08792286986	65	786.1697640722912	91	785.375012423798
40	788.8611327581715	66	786.1208344093767	92	785.3571696228715
41	788.6509682759294	67	786.0740945227875	93	785.3399018901655
42	788.4558406570236	68	786.0294155891747	94	785.3231847683079
43	788.2743467604125	69	785.9866781265449	95	785.3069950868429
44	788.10524360376	70	785.9457711925893	96	785.2913108817935
45	787.9474268872913	71	785.9065916621869	97	785.2761113210319
46	787.799912808114	72	785.8690435752701	98	785.2613766349806
47	787.6618226005014	73	785.833037547321	99	785.2470880522174
48	787.5323693444224	74	785.7984902357165	100	785.2332277395868
49	787.4108466693733	75	785.7653238559485		
50	787.2966190482371	76	785.7334657424677		
51	787.189113430172	77	785.7028479494965		
52	787.0878120052897	78	785.6734068877132		
53	786.9922459293113	79	785.645082993164		
54	786.9019898652141	80	785.6178204251762		
55	786.8166572224234	81	785.5915667904044		

The calculated wavelengths for the transitions $3\,^3\mathrm{P}_2 \to n\,^3\mathrm{S}_1$ used in Section 2.3.

B HV Switch: Circuit Diagrams & PCB Layouts

The circuit diagrams and the PCB prints for the two switches are given and explained here. Furthermore, pictures of the final boards are attached.

Both switches have been designed by Hansjürg Schmutz[1].

Circuit explanation

HV switch

The HV switch mainly consists of two consecutive MOSFETs. At first, the trigger signal of 5 V enters a TC4427 through pin 2 that is fed by $V_{DD} = +15$ V supply voltage. When the trigger is active, a voltage of $V = V_{DD}$ is applied to pin 7. The ceramic capacitances parallel to the supply voltage work as energy storage and can compensate voltage spikes or dips.

The output of the TC4427 is connected to a FQP5N60C. The source of the FQP5N60C is fed with the high output voltage (usually $300 - 500$ V) and the drain is connected to the output. The capacitances parallel to the high voltage input are energy storages.

To avoid damaging the MOSFETs Zener diodes are used after the high voltage input and before the high voltage output.

LV switch

The LV switch to control two different non-zero output voltages is based on a ADG436. The trigger input at pin 1 switches the output at pin 3 between the voltages applied to pin 2 and 4. For the trigger being off, the voltage at pin 4 is applied to the output. For active trigger, the voltage applied to pin 2 is fed to the output. The switch is supplied by $V_{SS} = -15$ V at pin 5 and $V_{DD} = +15$ V at pin 13. Every voltage input has one energy storing capacitance in parallel.

PCB explanation

The PCBs are designed such that amount of dissolved copper is minimized to reduce the deterioration of the acid bath. This method leads to large grounding surfaces as seen in the photographs given subsequent. For bad shielding, the large surfaces lead to capacitative coupling. Furthermore, the conducting paths are lain out such that they have a minimum distance of 3 mm between each other to avoid electric breakdown.
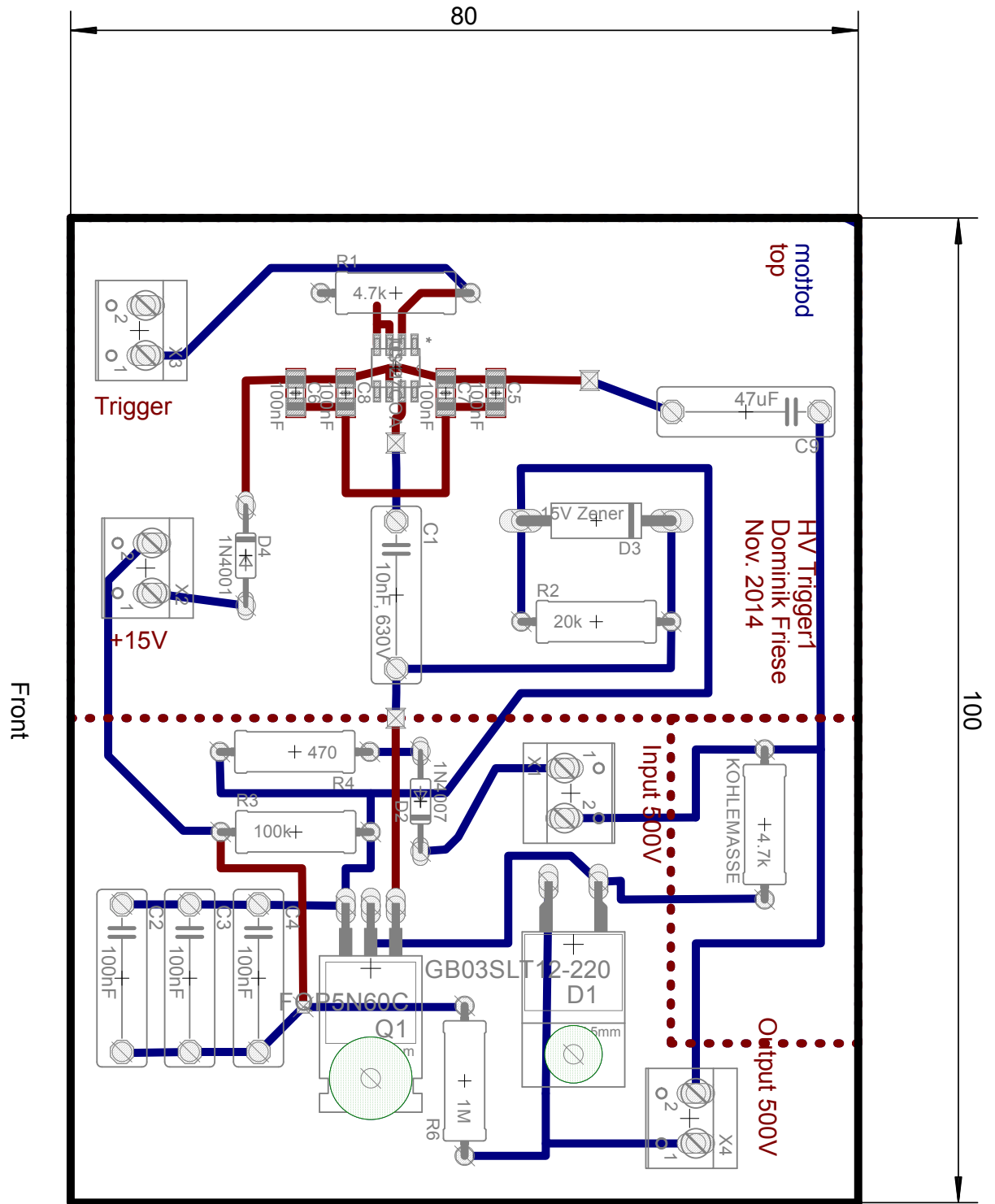
---

[1]Contact: hansjuerg.schmutz@phys.chem.ethz.ch

HV switch

Circuit diagram

PCB

80

100

mottod
top

Front

HV Trigger1
Dominik Friese
Nov. 2014

R1
4.7k

Trigger

X3
2 1

47uF
C9

D4
1N4001

+15V
X2
2 1

C1
10nF, 630V

15V Zener
D3

R2
20k

Input 500V

Output 500V

470
R4

R3
100k

1N4007
D2

X1
1 2
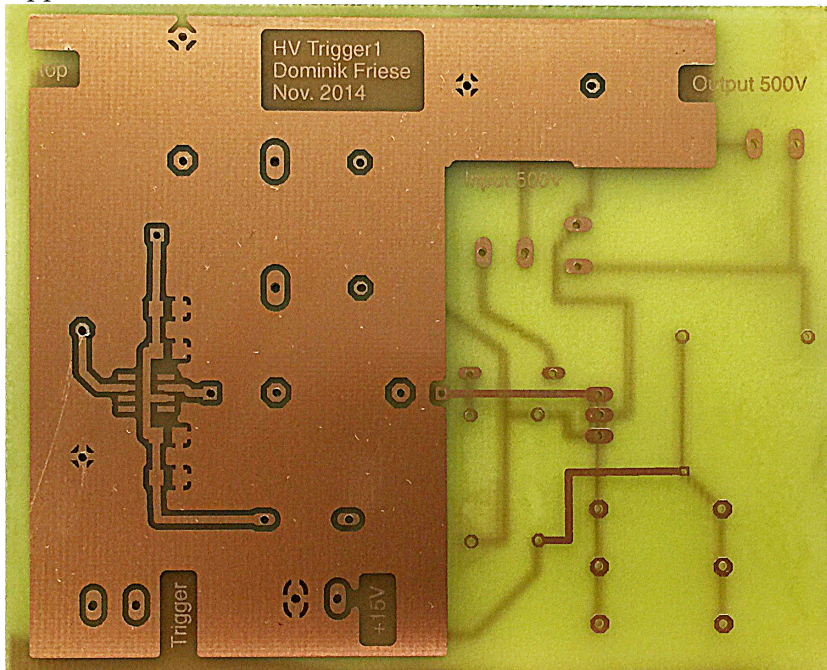
KOHLEMASSE
4.7k

C2
100nF

C3
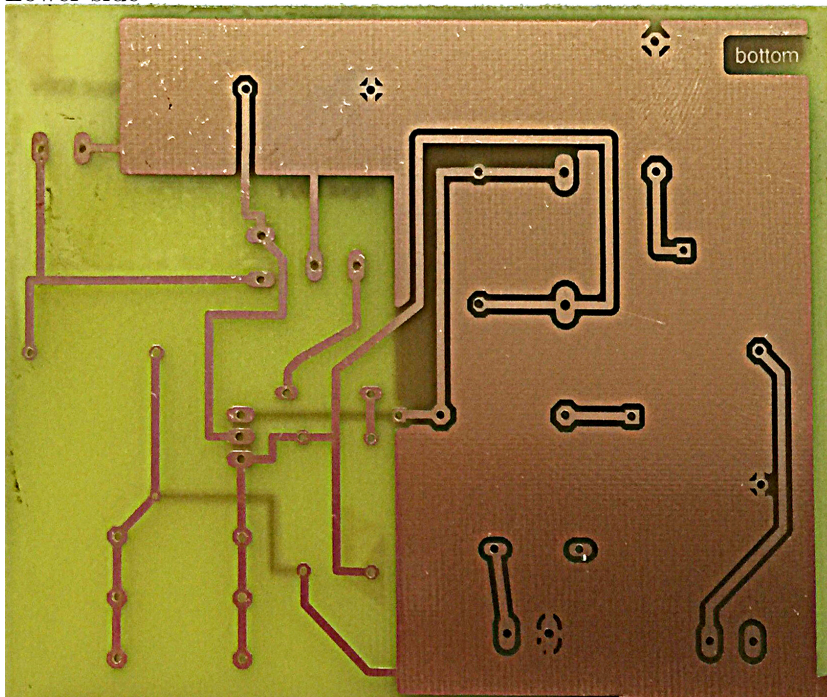100nF

C4
100nF
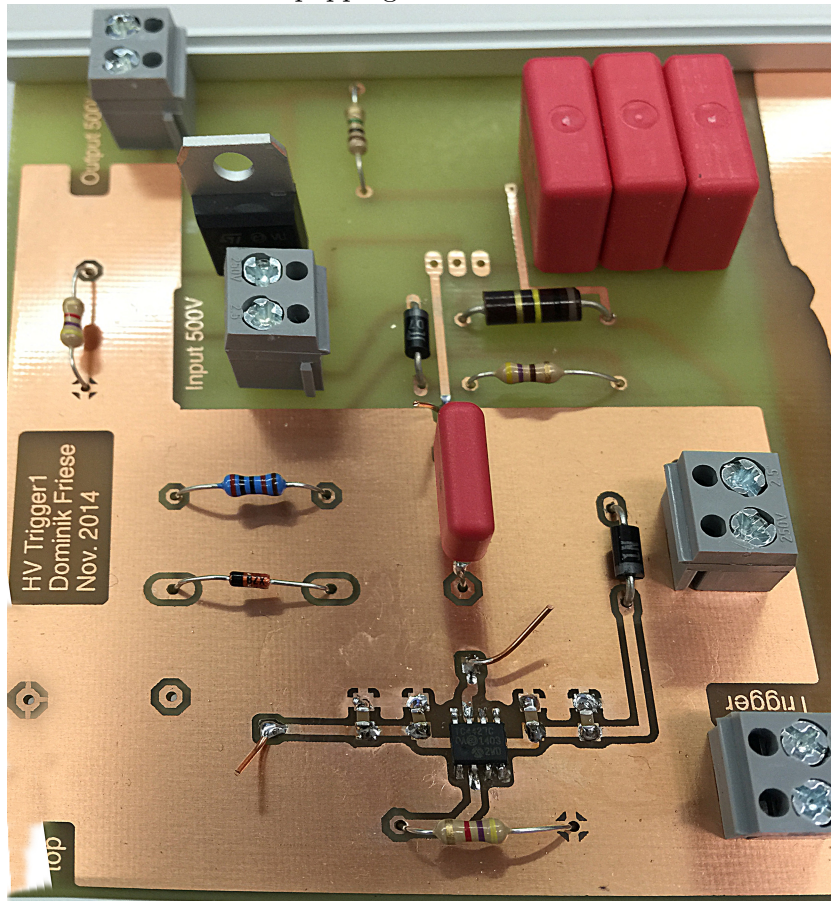
GB03SLT12-220
D1
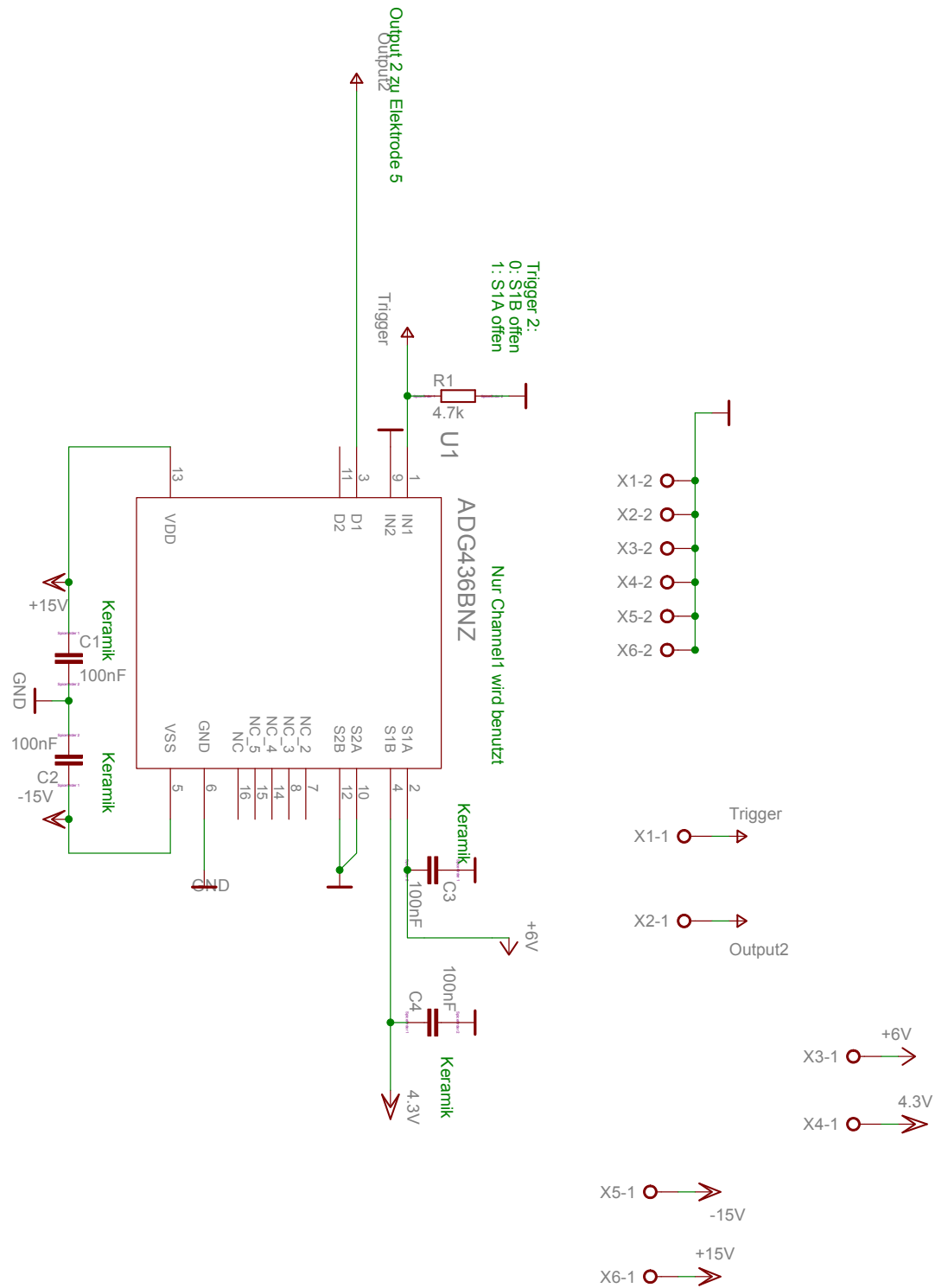
FQP5N60C
Q1

5mm

1M
R6

X4
2 1

67
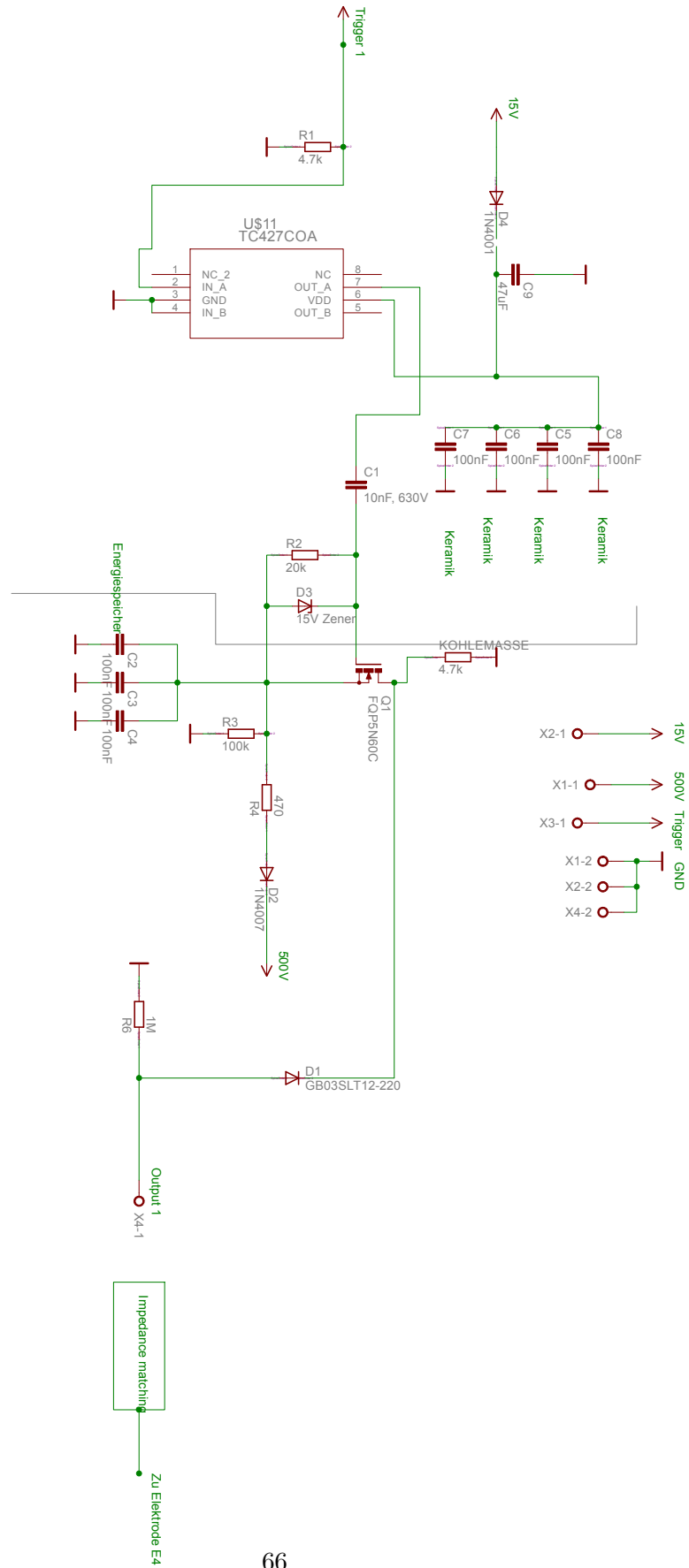
Photos

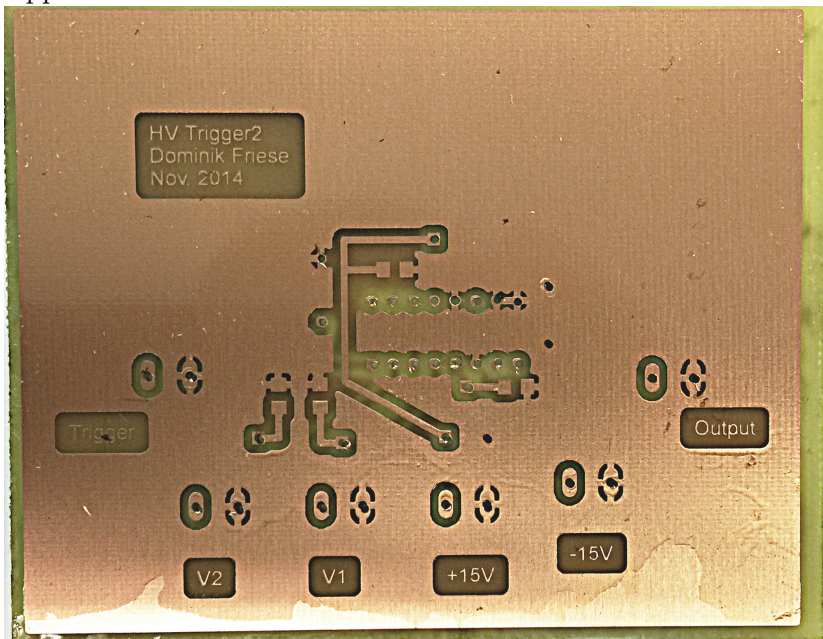Upper side
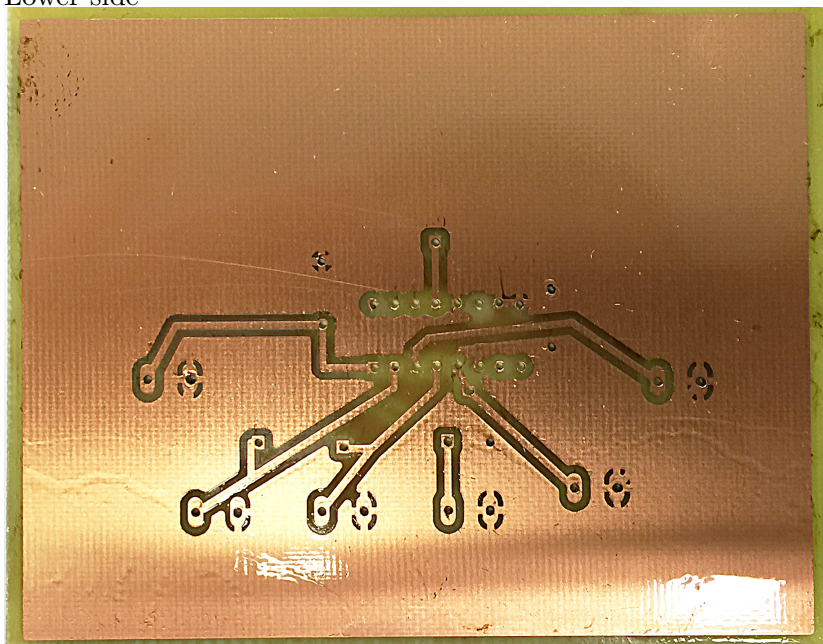

Lower side
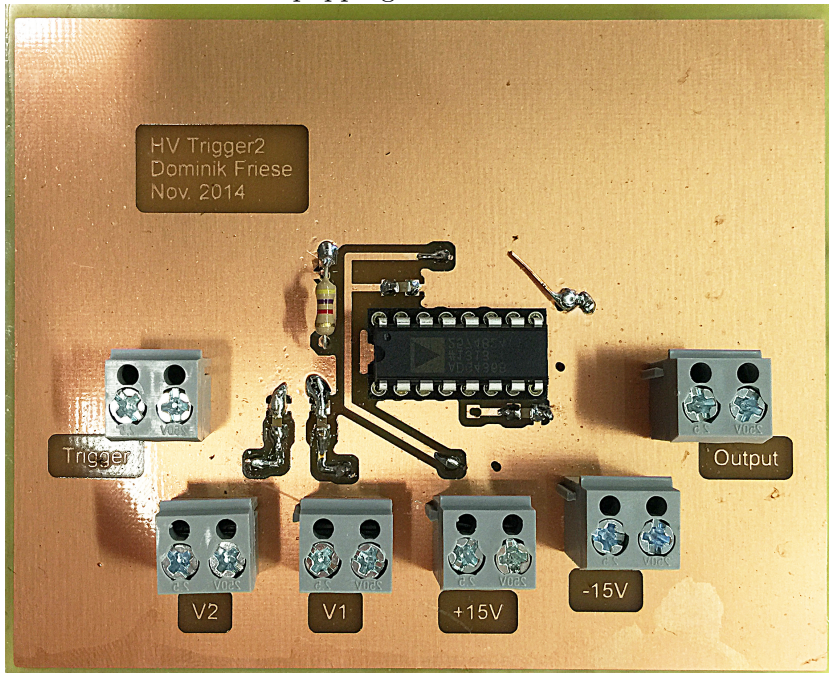
Finished board with equipping

LV switch

Circuit diagram

PCB

80

100

71
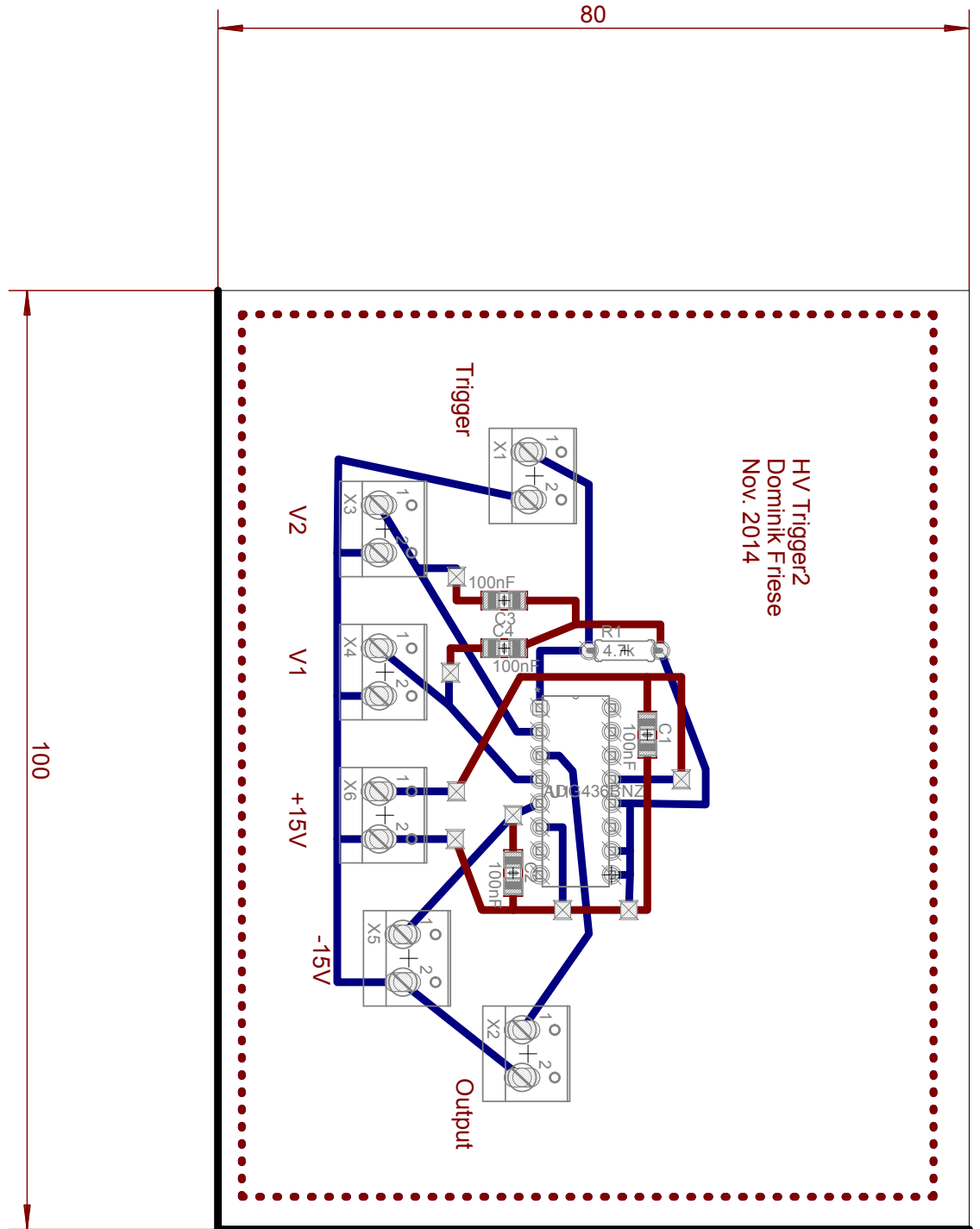
Photos

Upper side

Lower side

Finished board with equipping

C Screenshots

TA PRO Motor and piezo control (LabView)
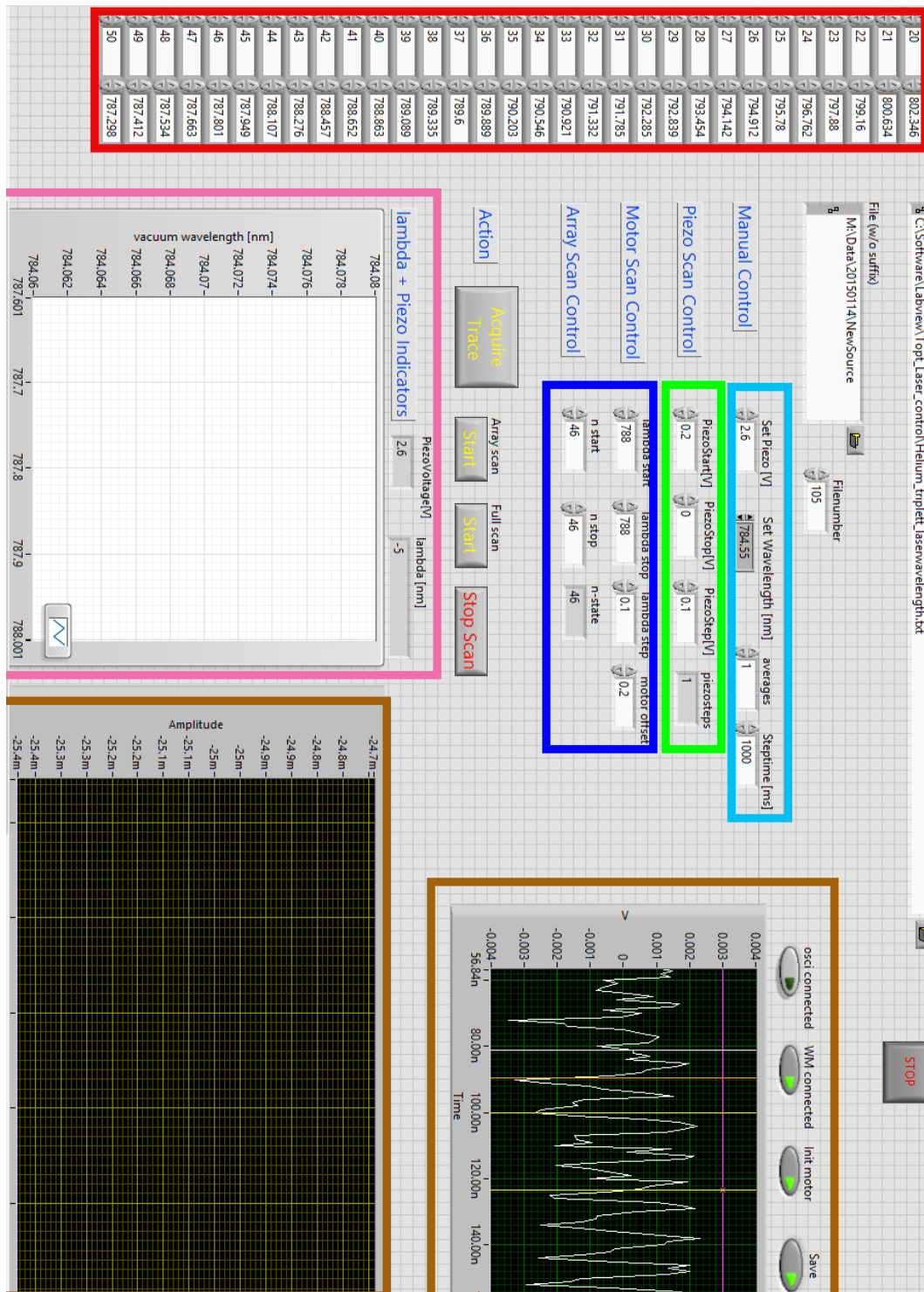
The LabView program we use to control the TA PRO. The red part shows the transition wavelengths for different n. The light blue elements can be used to set a specific motor and piezo position manually whereas green and dark blue can be used to sweep the laser's wavelength automatically. The graph in the pink rectangle displays the measured wavelength with respect to the applied piezo voltage. Brown shows an excerpt of the oscilloscope connected to the MCP.

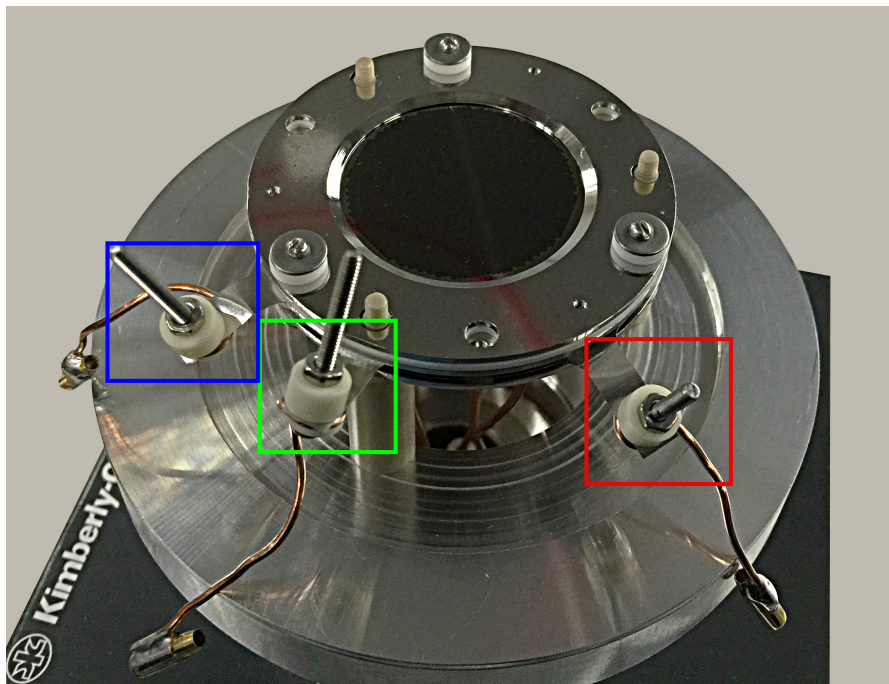# D MCP voltage supply

Circuit diagram
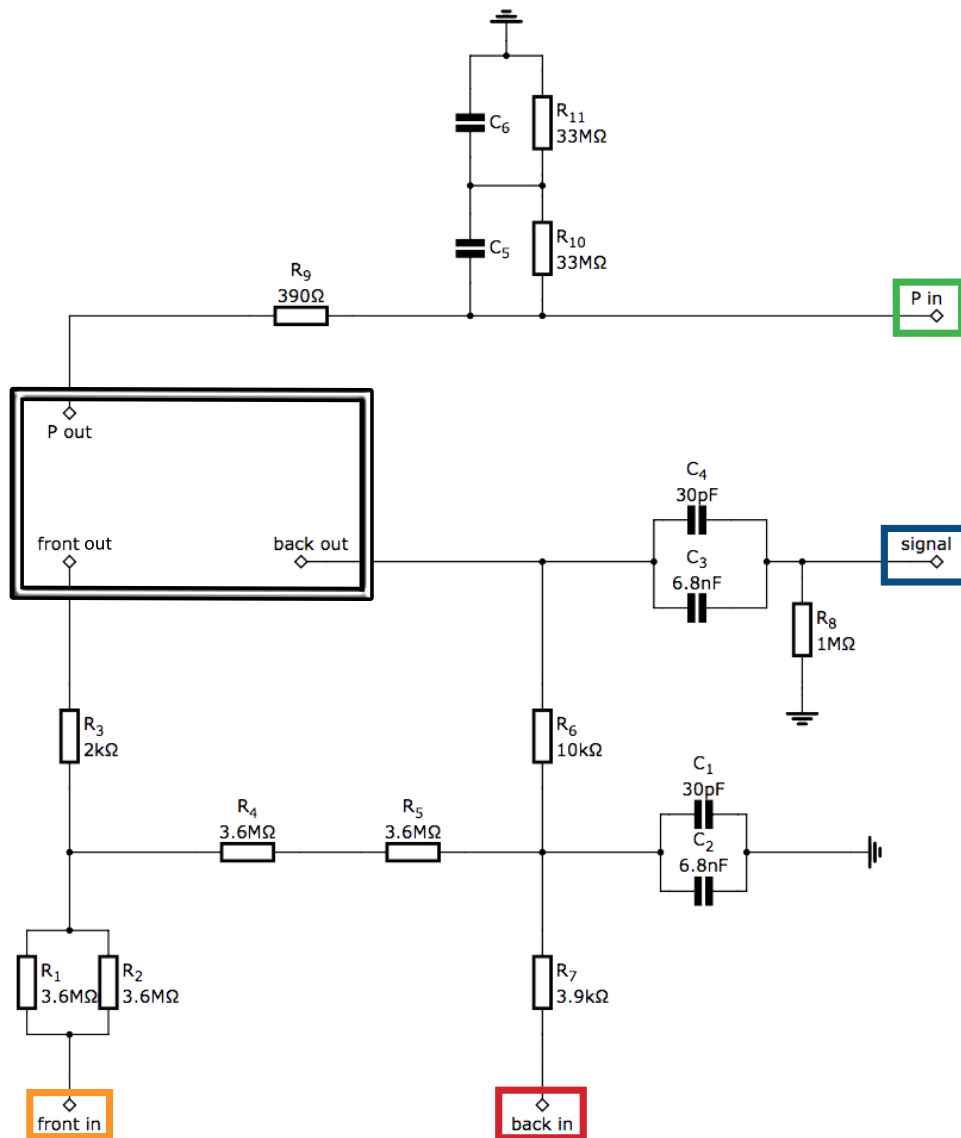
The supply circuit for the MCP. The front and back output are connected by a voltage divider. With 'front in' held at ground, the voltage applied to 'back in' is divided by 1:5 between 'front out' and 'back out'. The 'signal' output is parallel to the 'back' circuit. The phosphor screen circuit is independent from the rest.
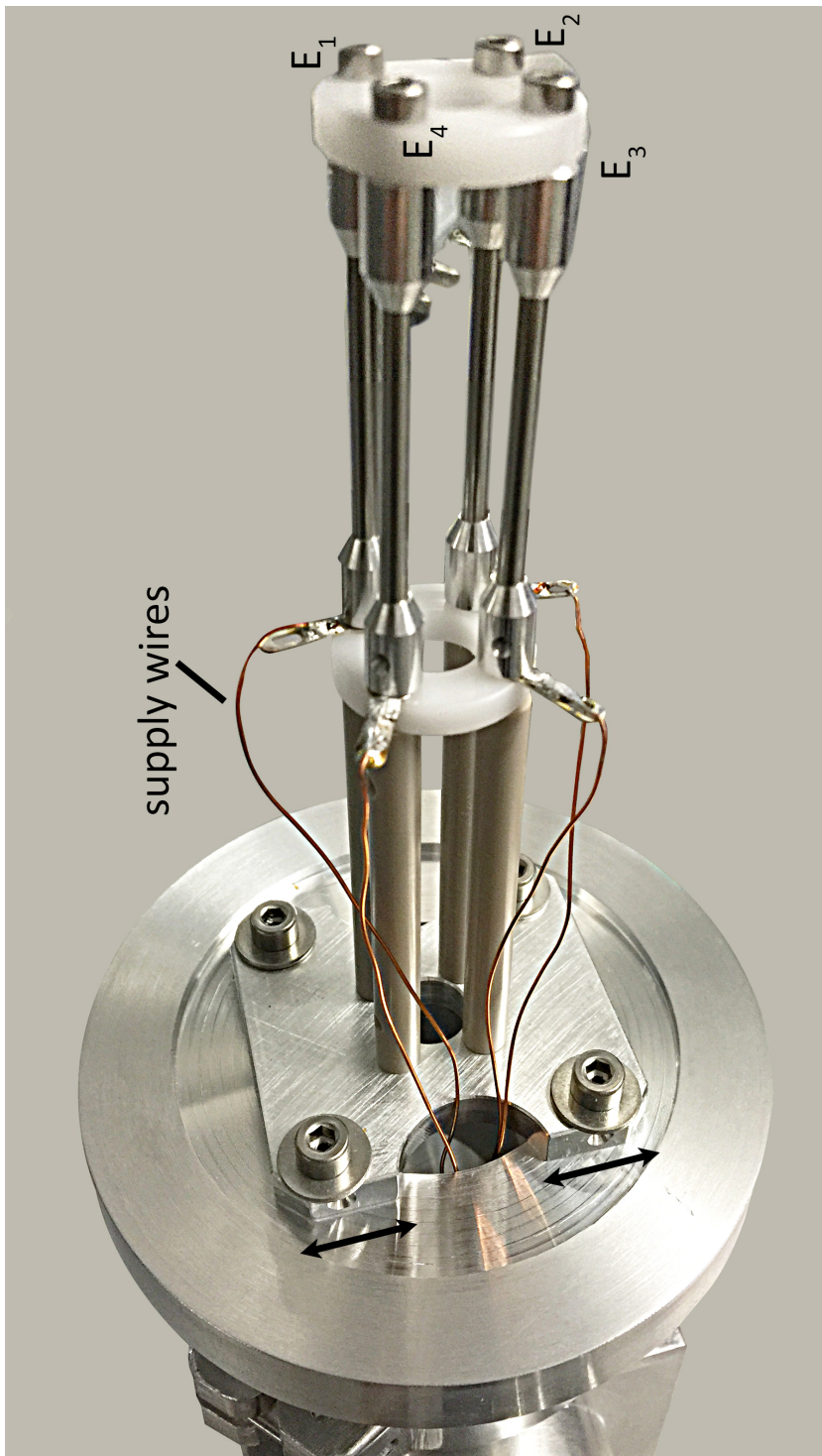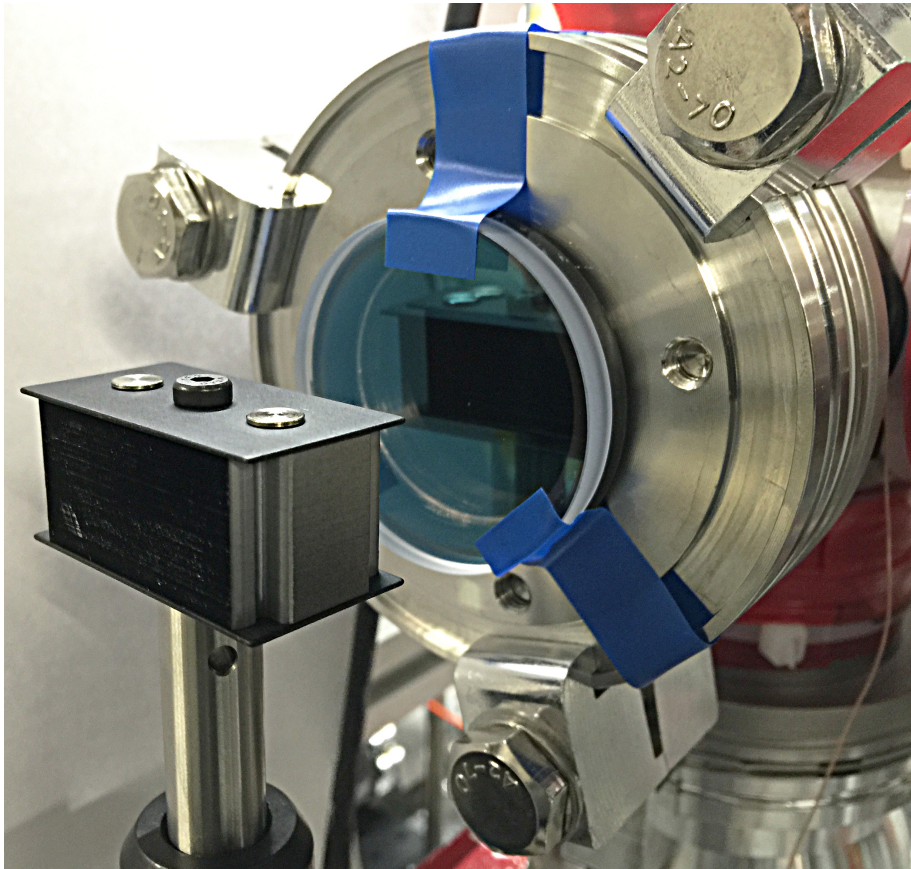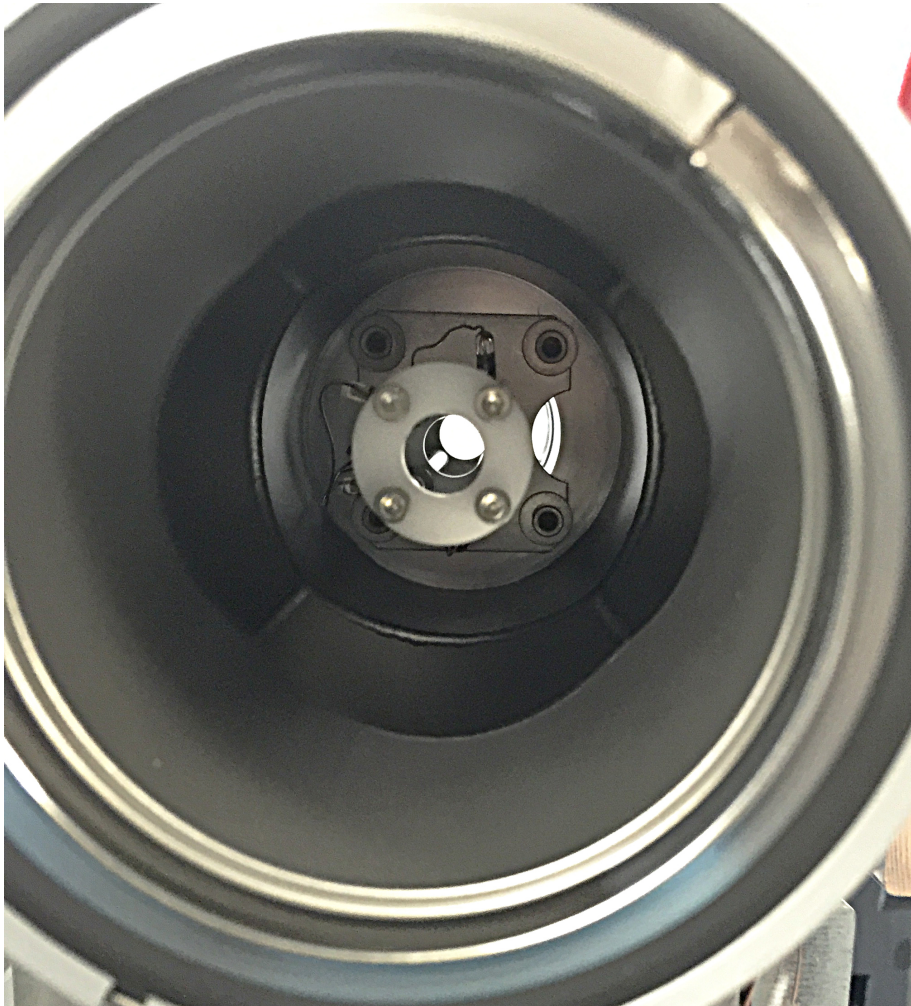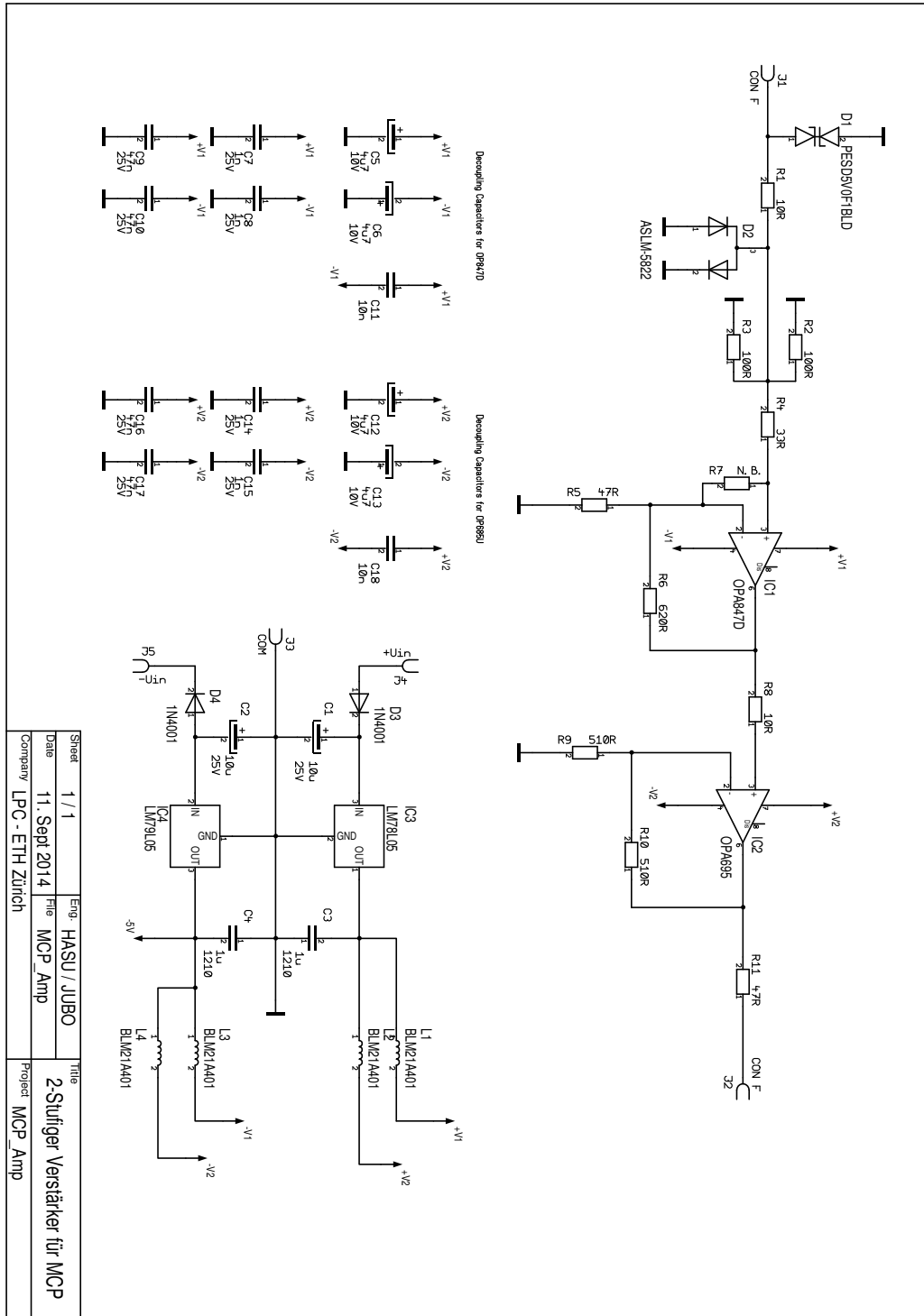
Finished circuit
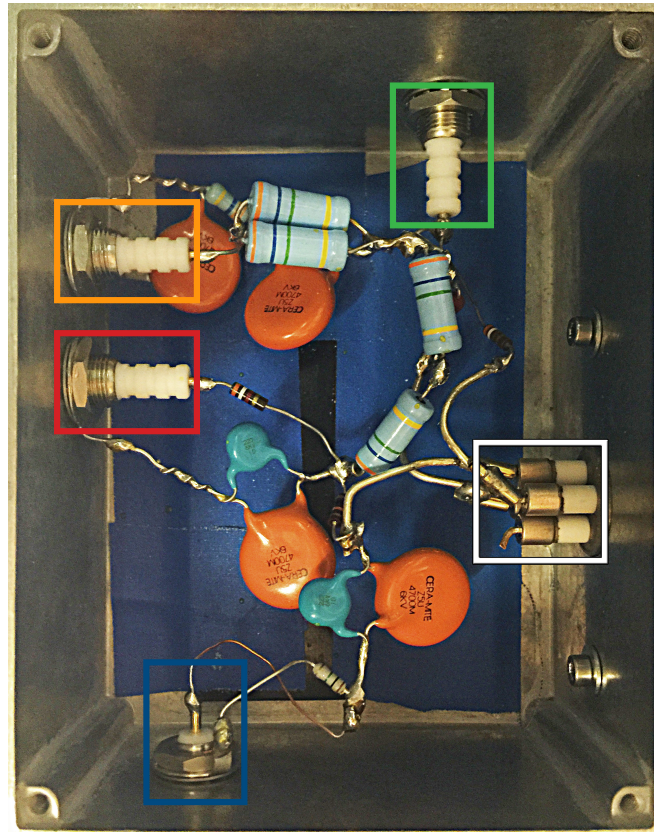
MCP

The three voltage inputs of the MCP are indicated. Blue is connected to the front plate, red to the back plate and green to the phosphor plate respectively metal anode. The inputs are connected to the outputs of the circuit indicated in white.

E Extraction electrodes & AR windows

F Fast MCP amplifier

The fast amplifier for MCP readout is a two level amplifier. In first step, an ultra-low noise OPA847D with a bandwidth of 600 MHz and a gain of about 10 dB is used. The output of the OPA847D is fed into a OPA695 with a bandwidth of 1400 MHz and a gain of about 9 dB.
To reduce noise, the supply voltages are decoupled with capacitances.

ETH

Eidgenössische Technische Hochschule Zürich
Swiss Federal Institute of Technology Zurich

Declaration of originality

The signed declaration of originality is a component of every semester paper, Bachelor's thesis, Master's thesis and any other degree paper undertaken during the course of studies, including the respective electronic versions.

Lecturers may also require a declaration of originality for other written papers compiled for their courses.

___

I hereby confirm that I am the sole author of the written work here enclosed and that I have compiled it in my own words. Parts excepted are corrections of form and content by the supervisor.

Title of work (in block letters):

Towards continuous wave Rydberg excitation for 2 ³S1 Helium

Authored by (in block letters):
For papers written by groups the names of all authors are required.

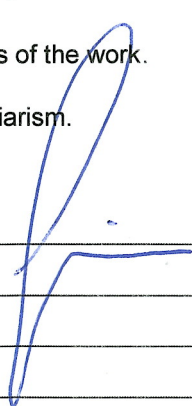| **Name(s):**	**First name(s):**
Friese	Dominik

With my signature I confirm that
- I have committed none of the forms of plagiarism described in the 'Citation etiquette' information sheet.
- I have documented all methods, data and processes truthfully.
- I have not manipulated any data.
- I have mentioned all persons who were significant facilitators of the work.

I am aware that the work may be screened electronically for plagiarism.

Place, date	**Signature(s)**
Zürich, 6.3.2015	

For papers written by groups the names of all authors are required. Their signatures collectively guarantee the entire content of the written paper.